

MASTER OF SCIENCE THESIS

A numerical investigation of using flap control on VAWTs

Shengling Lai

1 JULY 2015

A numerical investigation of using flap control on VAWTs

MASTER OF SCIENCE THESIS

For obtaining the degree of Master of Science in Wind Energy at Technical University of Denmark and Master of Science in Aerospace Engineering at Delft University of Technology.

Shengling Lai

1 July 2015

Department of Wind Energy, Technical University of Denmark
Faculty of Aerospace Engineering, Delft University of Technology



Copyright © Shengling Lai
All rights reserved.

EUROPEAN WIND ENERGY MASTER - EWEM
ROTOR DESIGN TRACK

The undersigned hereby certify that they have read and recommend to the Faculty of Aerospace Engineering for acceptance a thesis entitled “**A numerical investigation of using flap control on VAWTs**” by **Shengling Lai** in partial fulfillment of the requirements for the degree of **Master of Science**.

Dated: 1 July 2015

Head of the Department:

Prof. Dr.G.J.W. van Bussel of TUDelft

Supervisor:

Prof. Dr.Helge Aagard Madsen of DTU

Supervisor:

Dr.Carlos Simao Ferreira of TU Delft

Supervisor:

Dr.Mac Gaunaa of DTU

Supervisor:

Dr.Uwe Schmidt Paulsen of DTU

Abstract

The renewable energy need facilitates the development of offshore wind power. The abundant wind resource has pushed the wind farms into deep water sites. The floating VAWT concept is emerges as the times require. This research is part of Deepwind concept development.

The project focuses on verifying the feasibility of using flap control to increase the power conversion of a VAWT through the numerical investigation. As a preliminary implementation, only a 2-D section is taken out from the Darrieus rotor as the modeled object. The report concentrates on the purely aerodynamic modeling of a VAWT. All the blades are assumed to be fully rigid in order to exempt the structural response.

VAWTs present a distinct aerodynamic pattern from HAWT. To start up, a historical review on the aerodynamic models of VAWTs is performed to recap the critical issues in the aerodynamic modeling. The study mainly emphasizes on the momentum models, covers SST, MST, DMST and Actuator Cylinder (AC) models. AC mainly advantages on including the lateral inductions, and the wake interaction. Its precise prediction was confirmed in the simulation results of the aerodynamic model comparison study [10]. Hence, AC has been chosen as the numerical tool for VAWT modeling, both for the self-developed routine and HAWC2.

A promising solution to determine the load-form for optimal power is constructing a uniform distribution so that the power coefficient could reach Betz limit. The normal load distribution on the blade path is the link between the power conversion and the blade force. At the moment of the determination of the load distribution that leads to the optimal power, the required blade force at the different azimuth positions are also settled. The simulations are performed with $TSR=2, 3, 4,$ and 5 to verify the possibility on achieving the ideal power production in order to draw up an optimized control option.

The result of the study is presented as a form of different flap angles at discretized azimuth positions. Even though the load-form is universal, the resultant flap variation only works for the specific rotor because of the introduction of airfoil data in the computation. An H-rotor VAWT with flaps is set up in HAWC2 to validate the control strategy. As the supplement to AC model, a dynamic stall model called ATEFlap is integrated in HAWC2 to calculate the dynamic stall impact, and the influences from flap deflection for the given airfoil. The model is supposed to return the aerodynamic loading of the blades under the

dynamic stall. Hence, the deviations between the target load distribution obtained from the quasi-steady environment and the semi-dynamic one is observed as expected.

In the end, the flaps running with the given function could almost give the desired loading, but the deviations are observed in downwind part. It is mainly the hysteresis of the lift coefficient causes the difference. It is proven to be partly made up by increasing the flap deflections in the downwind side.

Acknowledgements

As the final outcome of my 18 years as a student, the thesis is presented here. China has an old saying, "Learning as long as you live". The thesis will not only be one of the milestone of my entire life, but also a new start. In such a memorable moment, I would like to outline some names that I am very much like to keep in mind forever.

First of all, my gratitude belongs to both of my supervisors Helge and Carlos. Dr. Carlos Simao Ferreira, thank you for proposing such an exiting topic as my master thesis. Pr. Helge Aagard Madsen, thank you so much for supervising me along with the whole project, lasting for eight months. Your timely and detailed reply, as well as the instructions help me overcome all the barriers one after another. Additionally, thank you so much, Dr. Mac Gaunaa who has patiently explained the theory behind ATEFlap model and the operation procedure of the pre-processor, even though you are not officially my supervisor.

I would like to thank all my friends who has supported me through the project. I cannot hand it in on time without your kindly help. Sercan Ertem, my solid ally and friend, thank you for all the time that we shared for the thesis. Particularly, thank you for providing me the airfoil polar, liberate me from an extra task. Bo Hu, who has unconditionally offered help, no matter professional or general questions. Yifei He, I am very grateful for you advice on clarify the research questions. Also, there are some friends who even though did not help me directly on the thesis, their companions enhance my last semester without any lecture.

Further, I would like to thank my family in China, who has been financially and mentally supporting my total 18-years education so far. Even though we do have not physically meet for almost one year, occasional audio calls make me feel like I am still at home.

Last but not the least, my final gratitude is to myself, to the 2 years as a master student in European Wind Energy Master. It is not only a great platform to get insight to wind industry, but also an opportunity to gain really nice international experience. I have become a better "I" during this two years. Thank you!

Shengling Lai
Lyngby, Denmark

Contents

Abstract	v
Acknowledgements	vii
List of Figures	xiv
List of Tables	xv
Nomenclature	xvii
1 Introduction	1
1.1 The background	1
1.1.1 A brief development history of VAWT	1
1.1.2 Offshore wind power	3
1.1.3 Deepwind concept	4
1.2 Research slope and motivation	6
1.3 Design approach	7
1.4 Thesis outline	8
2 An overview of aerodynamic models for VAWTs	9
2.1 The dynamic models	9
2.1.1 The Single Stream Tube(SST) model	10
2.1.2 The Multiple Stream Tube(MST) model	11
2.1.3 The Double Multiple Stream Tube(DMST) model	12
2.1.4 The Actuator Cylinder model	14
2.2 The kinematic models	16
2.2.1 The fixed vortex model	16
2.2.2 The free vortex model	17
2.3 CFD models	19
2.4 The comparison of the model performances	21

3	The implementation of the linear version AC model	23
3.1	The description of modeled rotor	23
3.2	Modified linear version (MOD-LIN) AC model	24
3.3	Implementing MOD-LIN AC in Matlab	25
3.4	The implementation in HAWC2	27
3.5	The validation	29
3.5.1	The results	29
3.5.2	Comments	29
4	Dynamic stall theory and modeling	33
4.1	A brief introduction to dynamic stall	34
4.2	The airfoil aerodynamics	35
4.2.1	The airfoil selection	35
4.2.2	The static stall	36
4.2.3	The pre-processor of ATEFlap	37
4.3	ATEFlap solution for dynamic stall	39
4.3.1	Potential flow solution	39
4.3.2	Dynamic stall	40
4.4	The function of ATEFlap in HAWC2	41
4.4.1	General function	41
4.4.2	Including the flap deflection	41
5	Load-form study	43
5.1	The power gain optimization: A recap on the previous research	43
5.2	Modeled rotor	44
5.2.1	The factors	44
5.2.2	The set-up	45
5.3	Load-form study process	45
5.3.1	The variables	46
5.3.2	Upwind side shrinking	47
5.3.3	The faults	47
5.3.4	The blade force	49
5.4	General result for load-form study	49
5.5	The flap control strategy	49
6	The strategy validation	55
6.1	An introduction to HAWC2	55
6.1.1	A wind turbine model in HAWC2	55
6.1.2	HAWC2 program structure	56
6.2	HAWC2 model set-up	57
6.2.1	H-rotor	57
6.2.2	Flap variation specification	58

6.3	The simulation process	58
6.3.1	The limitations of the flap modeling in HAWC2 for VAWTs	58
6.3.2	The initial test	58
6.3.3	The effects from the dynamic stall model	59
6.3.4	The modification	59
6.4	The validation result	60
7	Conclusion and recommendation	65
7.1	Conclusions	65
7.2	Recommendations	66
	References	67
A	The numerical model set-up	71
B	MOD-LIN Actuator Cylinder code	73
C	The outcome of the preprocessor	77

List of Figures

1.1	VAWT type, Savonius rotor, Darrieus turbine and H-rotor (from left to right)[9]	2
1.2	Eole, the 3.8MW Darrieus VAWT in Le Nordais	2
1.3	Hywind concept	4
1.4	The configuration of Deepwind concept[45]	4
1.5	VAWT v.s. HAWT in offshore application[36]	5
1.6	The force on the Deepwind shaft[34]	6
1.7	Design approach	7
2.1	SST model[6]	10
2.2	MST model[27]	11
2.3	The induction distribution [27]	12
2.4	DMST model[27]	13
2.5	Shed vorticities and the circulation change rate distribution[40]	13
2.6	Comparison of non-dimensional axial force[40]	14
2.7	The schemetic figure of the Actuator Cylinder model	15
2.8	The schemetic diagram of the fixed wake model[27]	16
2.9	The Kelvin theorum	17
2.10	The lifting line vortex model discretization	18
2.11	The induced velocity profile by a single filament	18
2.12	The vortex panel	19
2.13	The subgrid scheme[30]	20
2.14	The model performances for the test case with $\lambda = 4.5$, $\sigma = 0.1$ and skew infow angle= 3° (Left: Tangential loads; Right: Streamwise load)[10]	22
3.1	The azimuth position defination(Modified from [40])	24

3.2	The aerodynamic coefficients before and after MOD-LIN [21]	24
3.3	The flow chart on AC modeling in Matlab	28
3.4	The coordinate system in HAWC2 [21]	29
3.5	The power and thrust coefficients	30
3.6	The induction on x-direction distribution	30
3.7	The induction on y-direction distribution	31
3.8	F_n for TSR=2& 4	31
3.9	F_t for TSR=2& 4	32
3.10	A comparison performed by Sercan	32
4.1	The process of dynamic stall[18]	34
4.2	The decomposition of NACA0018 data	36
4.3	The airfoil movements[18]	39
4.4	The effect from wake memory term[5]	40
4.5	The effect from the dynamic stall term[5]	41
4.6	The effect from ATEFlap	42
5.1	The loadforms(left) and their induced C_p distribution(right)[1]	44
5.2	The local C_T distribution w.r.t. the blade number[4]	45
5.3	Power performance for Magdalen Island VAWT at 29.4rpm[4]	45
5.4	The process of load-form study	46
5.5	The ideal flow field and load distribution for a VAWT section	47
5.6	The illustration on the curve transforming	48
5.7	The fault of load-form	48
5.8	The optimized load-form	50
5.9	Flap variation for TSR=2	51
5.10	Flap variation for TSR=3	52
5.11	Flap variation for TSR=4	52
5.12	Flap variation for TSR=5	53
6.1	A wind turbine model in HAWC2	56
6.2	HAWC2 program structure[31]	56
6.3	The 3D H-rotor model in HAWC2	57
6.4	F_n v.s. θ with or without dynamic stall model	59
6.5	C_l v.s. AOA with or without dynamic stall model	59
6.6	Final result: Q_n distribution	61
6.7	Final result: Local $C_{p,i}$ distribution	62
6.8	The radial velocity distribution	63
A.1	Numerical model set-up	72

List of Tables

2.1	The model comparison	21
3.1	Modeled rotor	24
3.2	The start term $w_x(j)^*$	26
4.1	Airfoil data	36
5.1	Implementation parameters	46
5.2	The result of Load-form study	49
6.1	Final simulation result	60

Nomenclature

a	axial induction factor
a_{lin}	axial induction factor from linearized flow model
A	the area of the actuator disk in any stream tube
B	number of blades
c	chord length
C_l	Lift coefficient
C_d	Drag coefficient
C_p	Power coefficient
C_T	thrust coefficient
H	Rotor Height
Q_n	load coefficient perpendicular to the actuator cylinder surface
Q_t	load coefficient tangential to the actuator cylinder surface
C_n	normal force coefficient
C_t	tangential force coefficient
R	rotor radius
R_{w_x}	influence coefficient for induction in stream wise direction
R_{w_y}	influence coefficient for induction in lateral direction
v_x	axial velocity component
v_y	lateral velocity component
v_∞	free stream velocity
v_{rel}	relative velocity
w_x	induced velocity component
w_y	induced velocity component
α	angle of attack
θ	azimuth position
σ	rotor solidity

Abbreviations

AC	Actuator Cylinder model
AD	Actuator Disk model
AOA	Angle Of Attack
BEM	Blade Element Moment method
DMST	Double Multiple Stream Tube model
HAWT	Horizontal Axis Wind Turbine
MST	Multiple Stream Tube model
SST	Single Stream Tube model
TSR	Tip Speed Ratio
VAWT	Vertical Axis Wind Turbine

Subscripts

∞	the free stream
1	the first/upstream actuator disk
2	the second/downstream actuator disk
att	attached flow
eff	equally effective
fs	fully separated flow
i	azimuth index, stands for the influences from different points
in	the inner control volume
j	azimuth index, stands for different evaluation points
out	the outer control volume
st	steady
w	wake condition

Chapter 1

Introduction

Nowadays, following the fossil energy crisis, renewable energy is back to public attention and remarkably developed. Wind energy, commonly represented by HAWT has become a popular solution. For example, Denmark just created a record in 2014, namely 39% annual electricity consumption is provided by wind energy. The HAWT is meeting its limitation. Increasing blade imposes a significantly raising centrifugal force and bending moments, let alone the structural challenges. An alternative idea, VAWT is drawing the interest from the industry under the fashion of offshore wind power.

Section 1.1 recaps the major accomplishments on VAWT and offshore wind energy, and then introduces the hybrid concept Deepwind. Based on the previous research and the pre-defined study margin (Section 1.2), a rough experimental set-up is presented in Section 1.3. Finally, a brief structure of the thesis is displayed in Section 1.4.

1.1 The background

1.1.1 A brief development history of VAWT

A Vertical Axis Wind Turbine (VAWT) by definition is the turbine with a rotational shaft standing perpendicular to the wind direction.

One of the main perceived advantages compared with HAWT is that VAWT is not wind-orientate sensitive, and easily to accommodate wind shears. Thus, the yaw is eternally exempted from the concept. Pitch is also unnecessary. All of its heavy equipment, such as a nacelle, is stationary and located in the bottom.

The research on Vertical Axis Wind Turbine was once a R&D highlight around the 1970s and the 1980s, when the most of the listing aerodynamic model in Chapter 2 were developed. From the fundamental concept point of view, VAWT is partly defectives. A start-up device is necessary since sometimes wind cannot afford to produce a sufficient torque. For the same swept area, the VAWT rotor is relatively heavier than HAWT mainly due to a necessary longer blade. The low fatigue life of the bearings.

According to the driven source, VAWT is divided into lift-driven and drag-driven two

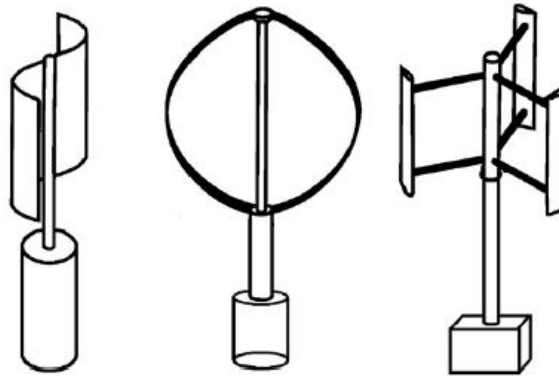


Figure 1.1: VAWT type, Savonius rotor, Darrieus turbine and H-rotor (from left to right)[9]



Figure 1.2: Eole, the 3.8MW Darrieus VAWT in Le Nordais

main types. The Savonius rotor is the only drag-driven concept shown in Figure 1.1. However, the design is not so popular due to its low efficiency compared with the other. The H-rotor mainly advantages on its simplicity. The straight blades are much preferred on both design and manufacture point of view compared with other two concepts are shown in 1.1. At the same time the H-rotor as a lift-driven machine behaviors much better than a drag-driven type. Similar to a HAWT, the rotating structures are supported at the tower top. The swept area of a H-rotor scales with $2R$, while the one for a HAWT scales with r^2 . This implies a heavier and larger rotor is thus needed to reach the same swept area, and therefore, a more server load situation on the tower top.

The final presented concept in Figure 1.1 is a curved rotor geometry named after its inventor G.J.M. Darrieus. It is capable to perform in a high efficiency. The egg-like shape results different TSR and uneven loading across the height. Despite of its difficulty on manufacturing, the blades are connected to the center tower at both ends in the full-Darrieus rotor. Their flapwise (radial) bending stresses during operation are significantly reduced thanks to the centrifugal load, so the blades are loaded mainly in tension. This is a very favorable loading scenario for composite materials, the blades can be made lighter than those cantilevered structures[41]. The set-up of Eole, a 2-sheets Darrieus Rotor with diameter 64m and height 96m, is considered as the milestone of the significant research on VAWT[46]. The turbine was capable to produce 3.8MW rated power, a great achievement in that age.

It is the mechanical problems finally terminated the further development of the concept. The bearing at the same time endured the sever load from the rotating giant rotor. This unfortunately led to an insufficiently short fatigue life. The project only operated from 1988 to 1992[41].

The research for VAWT paused due to the booming of HAWT concept. HAWT becomes a more popular choice thus developed until the largest one with 8MW rated power so far. Recently, VAWT has again drawn attention recently as a potential future concept, especially in offshore applications. One of the most-well known projects is the Deepwind concept lead by DTU-risø, will be discussed in Section 1.1.3.

1.1.2 Offshore wind power

General plot

The EU's Renewable energy Directive sets a binding target of 20% final energy consumption from renewable sources by 2020[44]. With the political support, the awareness that the sea offers a significant wind resource drives the industry to invest on the related projects and research.

Offshore wind power is defined as the construction of wind farms, located in the water, generating electricity from wind[43]. The offshore sites where the wind is constantly stronger than onshore sites are far away from the populations, avoiding the impact on the residence. As of 2014, the installed capacity in Europe was 8045MW. The average size of a grid-connected offshore wind farm in 2014 was 368MW (Data from EWEA), while the number in 2010 was 155.3 MW[19].

However, the offshore turbines is a more complicated design coupling with hydrodynamic problem and submerged design. The expensive transportation, install and maintenance fee becomes a heavy burden of taxpayers. Luckily, there is a decreasing trend of the value that makes the industry optimistic on the offshore wind power. UKERC5 in a 2010 report predicted smaller reductions of around 20% by 2025[19].

Floating wind turbine

The average water depth of offshore wind farms was 22m(EWEA). One of the reasons on the booming of European offshore wind power is that the water depth in Southern North sea where most ongoing projects located are mostly shallow(less than 40m)[7]. The thickness of the foundation is partly associated with the overturning moment by the wind load at the tower top, the deeper, the thicker, so more expensive. Hence, it is very clear that floating platform is more cost-effective in deep water.

One of the most promising concepts is the spar-type supporting structure, based on which Statoil has developed the world's first experimental large floating offshore wind turbine in 2009, namely Hywind[39]. Spar-type has a good performance on heave for its deep draft, but more pitch and roll motions come with it since the water plane area contribution to stability is reduced[35]. Consequently, the power performance is limited due to the instability of pitch motion.

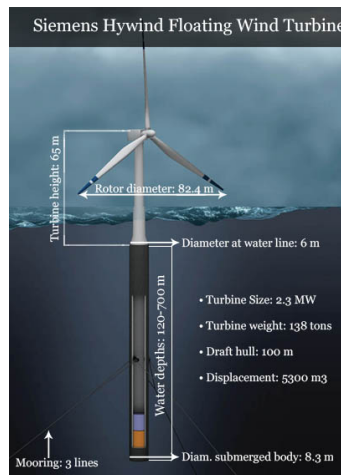


Figure 1.3: Hywind concept

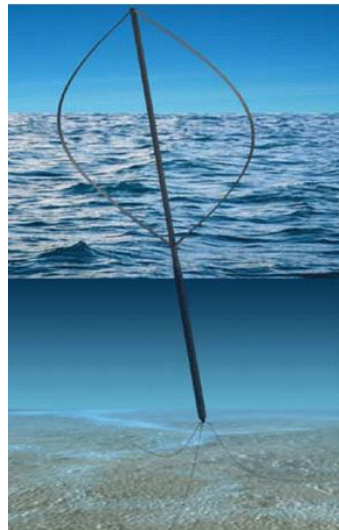


Figure 1.4: The configuration of Deepwind concept[45]

1.1.3 Deepwind concept

In 2010, Risø-DTU established an innovative offshore turbine concept. The new proposed floating offshore VAWT concept has been called DeepWind, because it initiates the feasibility to capture the wind resources at deep water sites. It is the Darrieus type employed as the rotor in the concept (See Figure 1.4) because of its better up-scaling potential[45]. Now, there are 12 international partners involved for different nine working package in the project[33].

Apart from those listed in Section 1.1.1, VAWT holds some particular advantages for the offshore applications, they are outlined below[16],

- More potential to scale up;
- A low center of gravity is helpful for forming the restoring momentum;

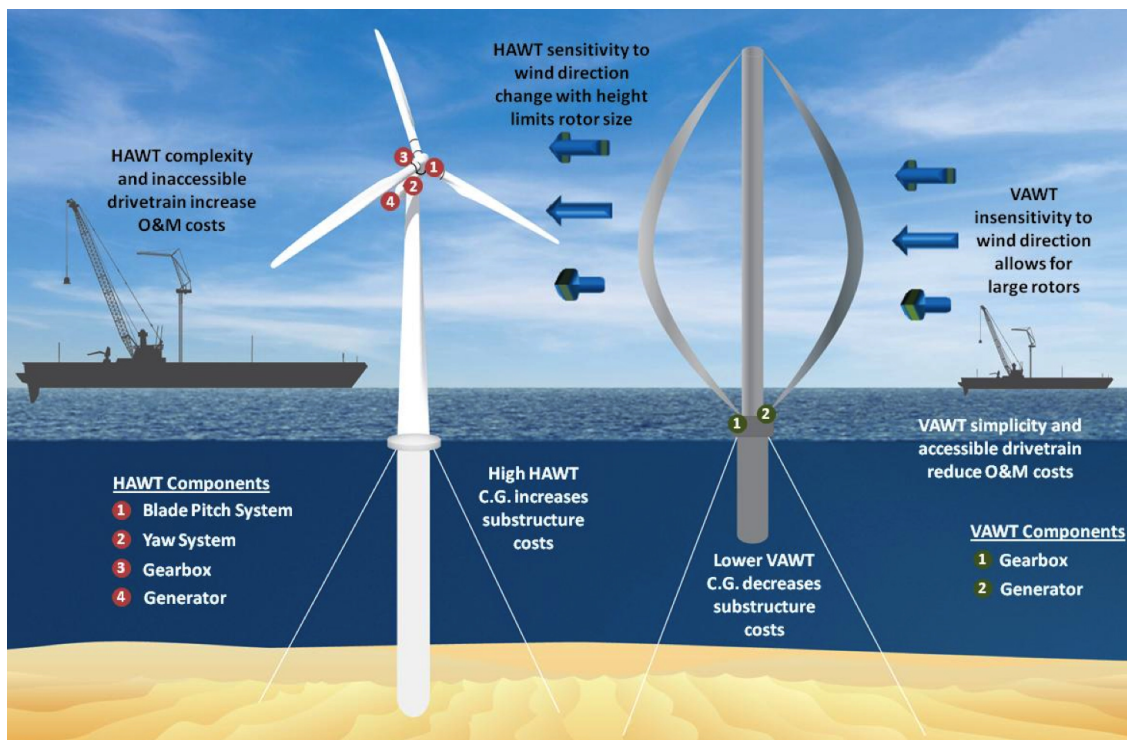


Figure 1.5: VAWT v.s. HAWT in offshore application[36]

- The wind loads finally acts at the nacelle for HAWT, while it acts from top to toe of a VAWT rotor, thus a lower overturning momentum is expected;
- The low position of the drive-train(near the sea surface) is much easier to get accessed, so a significantly lower O&M cost;

The floating platform of DeepWind concept is based on the spar technology. It is worth emphasized that low centre of gravity of the rotor is the most solid advantage to make it easier to "stand" in the water. As seen in Figure 1.5, the rotor is mounted on the base, and the generator is moved down, which leads to a much smaller floating support structure subsequently.

One of the key features is that the water is used as bearing for the rotating floater extending directly from the main shaft[28]. This is a feasible solution to avoid the critical load on rotor bearing.

The force analysis on the shaft is illustrated in Figure 1.6. A long hollow shaft rotates slightly tilted in water, inclining slightly, unlike the foundation of floating HAWT does not regularly rotate[38]. The shaft is mounted with the rotor producing aerodynamic power above sea level, and connecting to a direct drive generator under the water[34]. The buoyancy that acts on the shaft is expected to balance the gravity of the whole structure. Hence, the heavy rotor is supported by the rotor through the shaft.

In addition, water brake is considering as a possible solution for overspending protection.

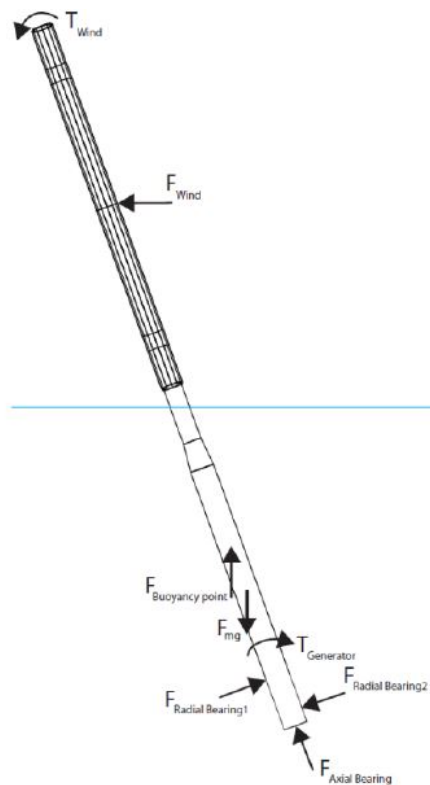


Figure 1.6: The force on the Deepwind shaft[34]

1.2 Research slope and motivation

As part of Deepwind concept development, maximize the aerodynamic power gain is one of the keys to draw the commercial interests. The core innovation of this research is applying the flap control into VAWT. This evidently leads to the central topic of the project: **Is it feasible from aerodynamic point of view that applying flaps into vertical axis wind turbine to increase the power gain?**

The study originates from Madsen et al.[22], where the potentiality of VAWT to increase the power output by squaring the load distribution has been pointed out (see Figure 5.8). For Darrieus Rotor, the flap is the only potential solution to change the load distribution, unlike H-rotor where pitch is also feasible.

Ferreira and Madsen et al.[10] have proved AC as the most accurate one among the tested momentum-balancing-based models. Moreover, a dynamic stall model returns unsteady aerodynamic coefficients for a 2D airfoil with flap has been developed by Bergami and Gaunaa [5]. Those two are the basis of the research.

As a preliminary investigation, only a 2-D horizontal section of the Darrieus rotor is taken out as the investigation object neglecting the 3 dimensional effect e.g. the inflow angle, and the whole rotor is assumed to be fully rigid so as to exempt the structural response. The ultimate outcome of the research will be a reference flap control strategy for the given airfoil or simply a report with "unfeasible" conclusion. If feasible, a reference flap deflection against the azimuth position to reach the maximum power would be provided as well.

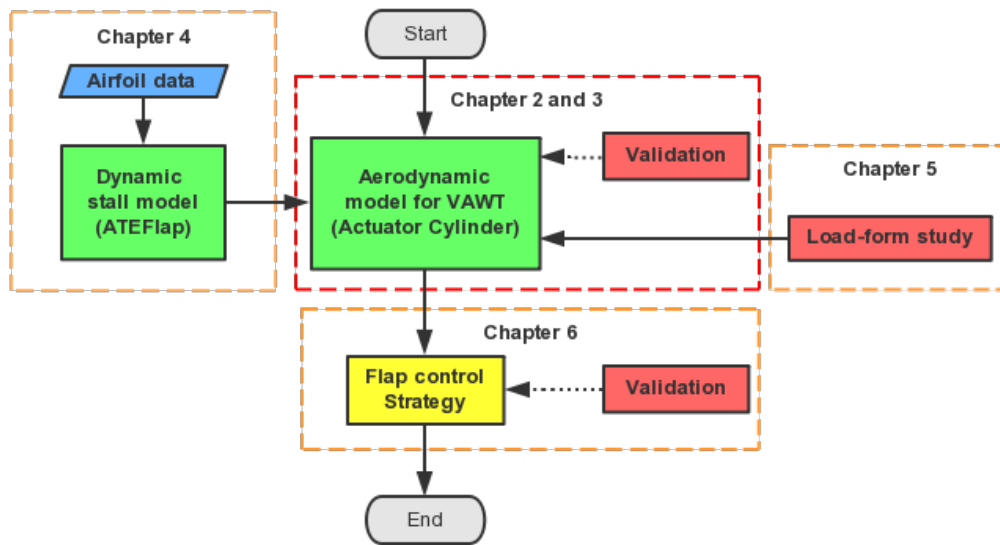


Figure 1.7: Design approach

1.3 Design approach

As an initial investigation, it is considered to be sufficient enough that all the experiments in this project will be fulfilled by numerical simulations. A rough numerical set-up is illustrated in Figure A.1, with the corresponding chapter number is also presented.

A self-developed AC code in Matlab is employed as the core element for the investigation. As a supplementation, ATEFlap model is adopted to introduce the effect from both flap deflection and dynamic stall. The load-form study is carried out to explore the optimized flap deflection at different azimuth position in the statistic state. It leads to the flap control strategy by cooperating with the other elements.

Two validation phases are involved in the numerical process, both are associated with HAWC2, an aeroelasticity code developed by DTU-risø. The one in Chapter 3 is to testify if the self-developed model works correctly by comparing the returned results for a same parameter set. As for the one in Chapter 6, the outcome control strategy is conducted in a dynamic working environment constructed within HAWC2. This is the procedure that directly leads to the conclusion.

Also, a detailed version of numerical model set-up is available in Appendix A. The basic elements are the same as those in Figure A.1, but the specific acting functions and even the relevant parameters are added.

1.4 Thesis outline

- Chapter 1 introduces the research background, especially the Deepwind concept. The research motivation and a rough design approach are also established.
- Chapter 2 contains a historical literature review on the aerodynamic models for VAWT.
- Chapter 3 describes the implementation of Actuator Cylinder model through Matlab and presents the numerical model validation.
- Chapter 4 presents a brief version of both theoretical and practical description of a dynamic stall model including the flap affection, namely ATEFlap.
- Chapter 5 discusses what the load distribution should be to obtain the largest possible power. Subsequently, a flap control strategy is obtained for further verification.
- Chapter 6 presents the results of the strategy validation.
- Chapter 7 recaps all the important results and points out the direction of further researches.

The content of Chapter 2 and 3, as well as the corresponding programming tasks are performed during the 15 ECTs special course phase. The rest of chapters are for 30 ECTs MSC thesis in DTU. Those two parts are integrated and presented as one piece to meet the 45ECTs working load requirement at TU Delft.

An overview of aerodynamic models for VAWTs

The chapter presents a historical recap about the aerodynamic models for VAWTs. The review ranges from the 1970s when the simplest VAWT model Single Stream Tube (SST) model was firstly proposed, up to the establishment of the vortex theories and modern CFD schemes. The basic physical assumptions and a brief implementation procedures are discussed.

All the existing aerodynamic models for VAWT could be sorted into three groups, two of which are classified according to their setting up B.C., the kinematic model (The actuator models) and the dynamic model (The vortex models)[20].

The dynamic models concern the external forces acted by the blades on the fluid volume. In other words, the blades (or the whole rotors) are presumed as the driven source of the forcing. Thus, the models are so-called actuator models, all illustrated in Section 2.1.

The basis of the kinematic models is impermeability condition at the blade surface, meaning that the normal velocity component at the control point is constantly zero. Since the source of the induced velocities appear as "vortex", the blades and the wakes are integrally treated as the vortex panels. They are presented in Section 2.2.

The last one is based on the NS equation solving, known as Computational Fluid Dynamics (CFD) model (Section 2.3).

A comparison among the listed model is carried out in Section 2.4, from the complexity, accuracy and the computational effort aspects. As a supplement, the numerical comparison results of [10] to support the arguments. As a result, Actuator Cylinder model is selected for further implementations.

2.1 The dynamic models

The theoretical foundation of the dynamic models is the actuator disk theory[12]. The modeled one-dimensional wind flow is assumed to be incompressible and homogeneous,

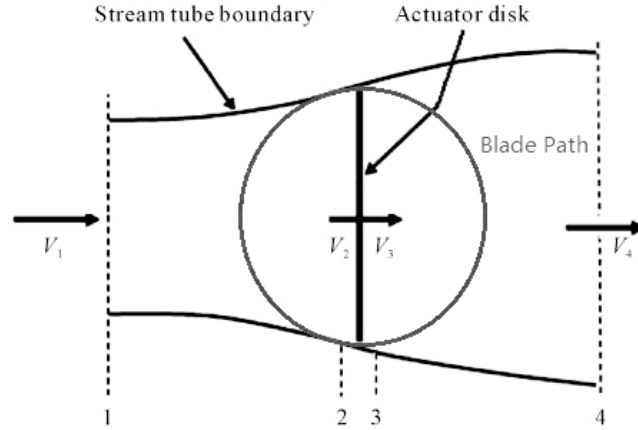


Figure 2.1: SST model[6]

without viscous effects (Thus no dynamic stall). Applied time-averaged, the flow is also considered as stationary. The real turbine rotor is represented by an infinitely thin permeable disk facing the wind, where the velocity distributes equally[23].

As momentum-balance based models, the momentum decrease of the control volume is balanced by the average work by rotor forces applied on the stream tubes. Thus, all the resultant blade forces and the velocities at certain positions are constant during the modeling time. The actuator theory has been a mature industrial choice to design a HAWT as part of BEM.

2.1.1 The Single Stream Tube(SST) model

The successful application of the actuator model in HAWT has inspired researchers to transplant it to VAWT. The first pioneer is Single Stream Tube(SST) model firstly presented by Templin in 1974[42]. Similar to the actuator configuration for HAWT, the rotor is replaced with a disk plane perpendicular to the wind. Both HAWT and VAWT get the most of vortex shed at the disk ends. Hence, the simply direct transplantation was accepted[40].

The induced velocity area is extended as the blade swept area, where the velocity at the disk v_1 is constantly equal to $(1-a)v_\infty$, disregarding the wake effect inside the considered region. Hence the induced velocity and the thrust formulas are exactly the same as the ones for HAWT

$$\begin{aligned} v_1 &= \frac{1}{2}(v_\infty + v_w) \\ T &= 2apv_\infty^2(1-a)A \end{aligned} \quad (2.1)$$

SST is naturally an actuator disk model. The global variables such as a and v_1 is determined through the actuator disk, while the swept area or the azimuth position is taken into account only for computing the local parameters like the blade forces since AOA varies significantly during the spinning. It follows that the power output follows Betz

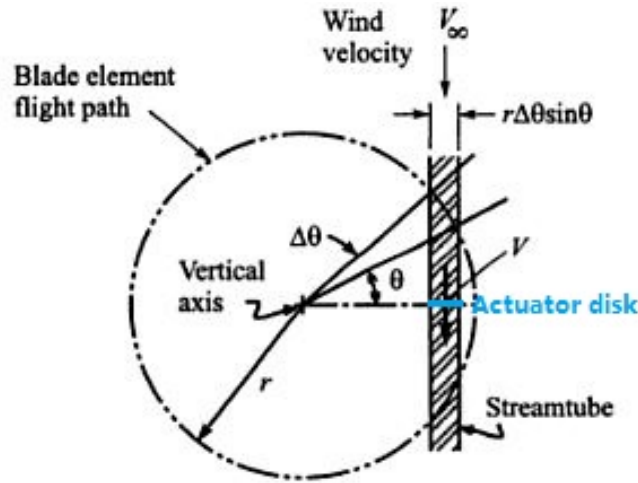


Figure 2.2: MST model[27]

limit $\frac{16}{27}$.

SST is an ideally simple model takes no account of the blade-wake interaction inside the swept region. Moreover, the crude assumption of the constant velocity distribution throughout the swept area is fundamentally incorrect, which leads to an imprecise estimation as a result.

2.1.2 The Multiple Stream Tube(MST) model

A VAWT blade passes by any azimuth position, facing different inflow direction, so the resultant parameters (a and V_{rel}) are obviously different. As a sufficient correction to this issue, the Multiple Stream Tube model(MST) for Darrieus concept has been introduced by Strickland in 1975 [42]. An equally piece-wise stream tube passing through the swept area is presented, where an individual actuator has been placed. The respective blade force and induced wind speed at different sub-tubes are estimated independently.

A relationship between the local stream-wise blade force F_x and the velocity ratio $\frac{v_1}{v_\infty}$ is valid in any sub-tube,

$$\frac{BF_x}{2\pi\rho r\Delta h\sin\theta v_\infty^2} = \frac{v_1}{v_\infty} \left(1 - \frac{v_1}{v_\infty}\right) \quad (2.2)$$

with Δh is the height of the blade element. Figure 2.3 demonstrate the simulation result of Strickland's Darrieus Turbine, showing the induction distribution among the Darrieus rotor. The induction varies significantly at any resolution, especially in a large horizontal section.

However, MST still have difficulty on including the wake interaction, the assumption of the constant velocity still validates for any of the sub-tubes. Hence both SST and MST has a trend of overestimating the power output.

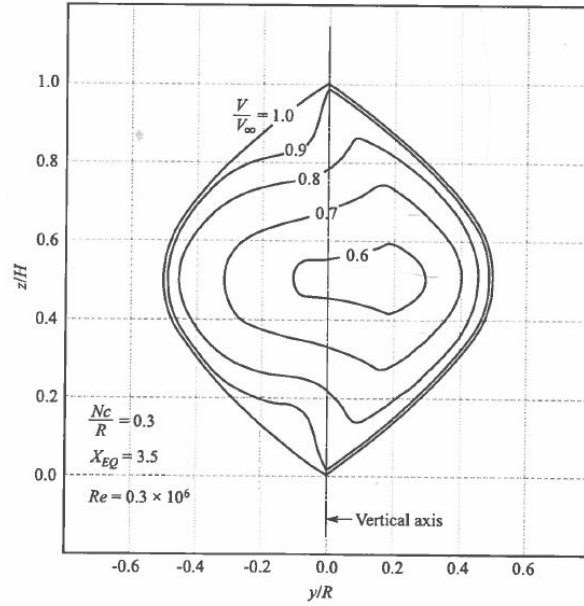


Figure 2.3: The induction distribution [27]

2.1.3 The Double Multiple Stream Tube(DMST) model

As a potential improvement of MST model on the wake affections, Paraschivoiu[27] has brought forward a model divides the swept area into the up- and downwind half represented by two tandem independent actuator disks. That is so-called Double Multiple Stream Tube(DMST) model. Soon, it had became the most common approach for VAWT for its simplicity and slight computational effort.

The schematic diagram of DMST is shown in Figure 2.4. For every sub-tube, the two actuator disks are placed with a distance $2R$ [27], regardless of the actual distance. This actually does not matter for momentum-balanced model, because the induction for the later disk is determined based on the presumed far wake velocity obtained in Bernoulli's equation. The wake deficit as the change of the distance is not considered.

It is important to mention that Betz limit is no longer valid for tandem actuator disk pair, Newman [26] has shown that the new maximum C_p in this case increases to $\frac{16}{25}$.

It is questionable that both MST and DMST do not taken the interference among adjacent sub-tubes into account. For MST, the expanded region is not an issue since they are out of scope, unlike DMST, the phenomenon would affect the downstream disk. According to Figure 2.4, the influence is neglected.

The velocity on the two tandem disk are calculated as,

$$\begin{aligned} v_1 &= (1 - a_1)v_\infty \\ v_2 &= a_2(1 - 2a_1)v_\infty \end{aligned} \quad (2.3)$$

The input velocity on the downstream disk is exactly the wake velocity of the upstream one, but there is no frank information about the relation between the two induction factors but $a_1 \geq a_2$. Even though the wake-inference is involved in DMST, C.S. Ferreira[40] has pointed out that DMST is essentially flawed due to an incorrect division of the wake into

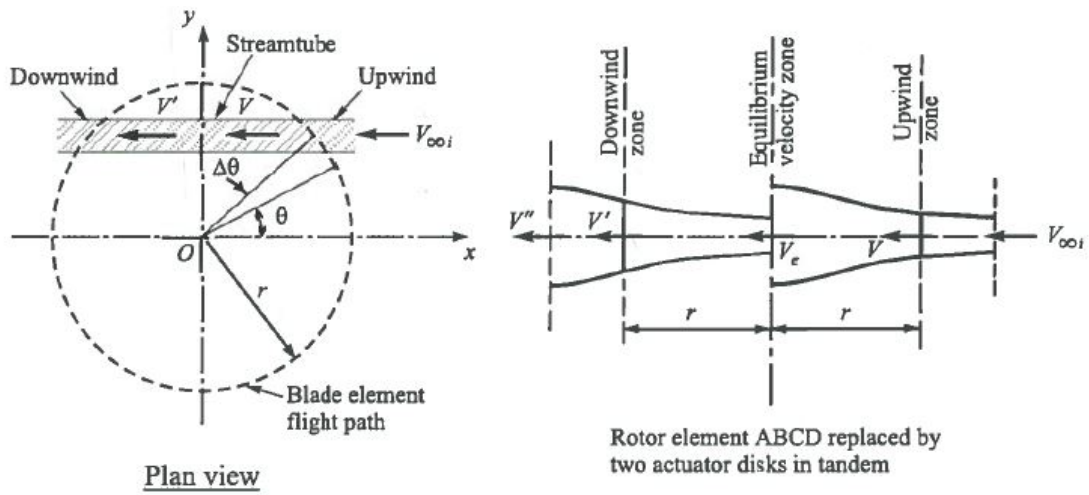


Figure 2.4: DMST model[27]

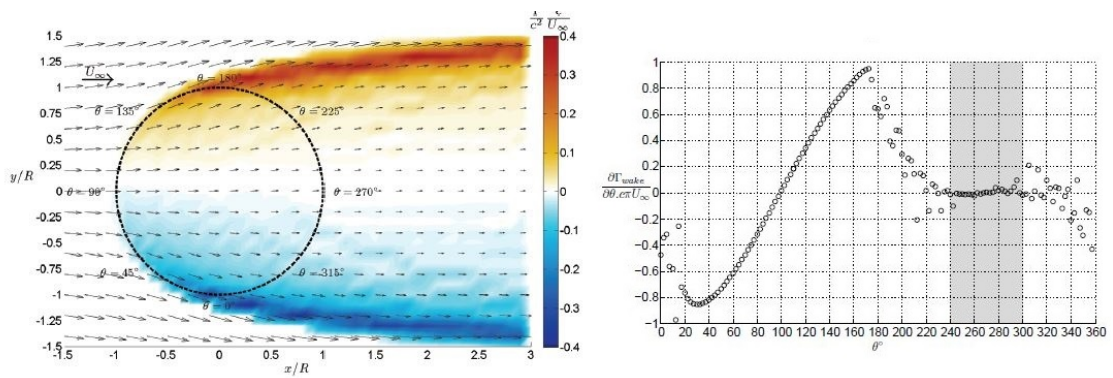


Figure 2.5: Shed vorticities and the circulation change rate distribution[40]

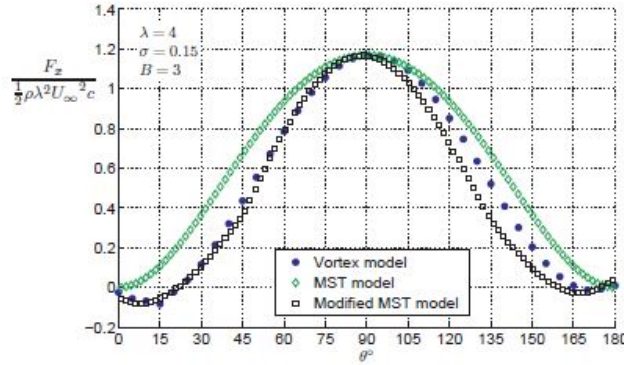


Figure 2.6: Comparison of non-dimensional axial force[40]

two separate elements shed from two actuator strips. As shown in Figure 2.5, shedding vorticities or the change of bound lifting vortex mostly occurs at the windward and the leeward (see Figure 3.1). Around $\theta = 270^\circ$, the bound vortex barely changes. In other words, the induction is mostly contributed by the wake induced in upwind half of the rotation, with little contribution from the downwind half. Thus an inaccurate estimation would occur on the two-equal-disks idea.

Moreover, as seen in Figure 2.6, gaps exist between DMST and vortex model curves, except at $\theta = 90^\circ$, or purely upwind position. Recall the velocity field showed in Figure 2.5, it is observed that the streamtubes expand even before reaching the blade path. The ignorance on the y -direction velocity component is considered as one of the reason leads to the inaccuracy, because it would affect AOA and finally the induction and the blade forces. Supplementary, C.S. Ferreira[40] has proposed a lateral induction factor $a_\perp = \frac{v_y}{v_\infty}$ to improve the DMST, and succeed as seen in Figure 2.6 showing the axial force, but unfortunately, only on the upstream half.

2.1.4 The Actuator Cylinder model

In the previous section, the introducing a_\perp has successfully improved DMST model implies that including the lateral induction is significantly helpful for increasing the accuracy. The idea has already been generated and developed from 1979 to 1982, as the Ph.D. project of Madsen[20]. That is the Actuator Cylinder model.

The conventional actuator models above are originated from the horizontal wind turbine. The rotor of VAWT is assumed as an actuator disk facing the wind. As a 2D model, the flow is considered as purely one dimensional disregarding the lateral velocity fluctuations. However, those models do not fit the curved surface of the blade path. It is on the swept route of the blades that the aerodynamic forces are acting in. Thus they are more concerned instead of the evaluation points (on the disk) of AD model. Furthermore, it is the stream-wise component of the blade force considered more in AD models. This is partly correct since it is the radial components $F_r(\theta)$ has caused a pressure jump surface in fact. Hence, the pressure jump can be expressed as the function of time-averaged $F_r(\theta)$,

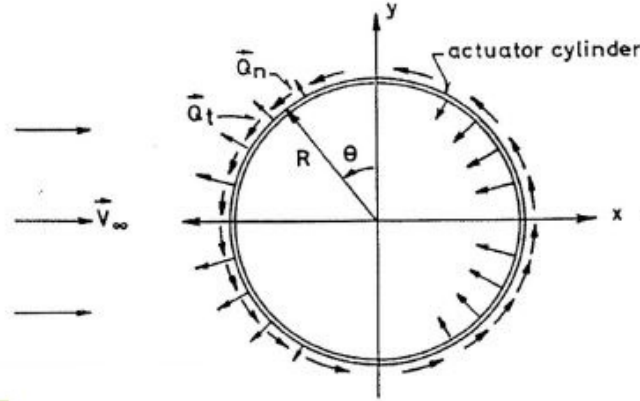


Figure 2.7: The schematic figure of the Actuator Cylinder model

$$\bar{\Delta}p(\theta) = \frac{NF_r(\theta)}{2\pi R} \quad (2.4)$$

Hence, the stream-wise and the lateral components are equally important. As shown in Figure 2.7, the rotor is assumed to be an actuator cylinder wrapping up the swept area instead of a disk, and the normalized one dimensional wind velocity (in-compressible potential flow) comes along the x-axis to the cylinder. the two components of the wind speed is then given as

$$v_x = 1 + w_x, v_y = 0 + w_y \quad (2.5)$$

The Navier-Stock equation connects the velocity components with loads (pressure, volume force components f_x and f_y). The normalized constant can be canceled out, only the perturbation terms are still effective. With the help of continuity equation, we have

$$\begin{aligned} \frac{\partial w_x}{\partial x} &= -\frac{\partial p}{\partial x} + f_x + g_x \\ \frac{\partial w_y}{\partial x} &= -\frac{\partial p}{\partial y} + f_y + g_y \end{aligned} \quad (2.6)$$

where the second order terms(induction-related) are denoted as g_x and g_y . Applying a derivative on their corresponding evaluating direction, a Poisson type equation is obtained,

$$\frac{\partial^2 p}{\partial x^2} + \frac{\partial^2 p}{\partial y^2} = \left(\frac{\partial f_x}{\partial x} + \frac{\partial f_y}{\partial y}\right) + \left(\frac{\partial g_x}{\partial x} + \frac{\partial g_y}{\partial y}\right) \quad (2.7)$$

The Poisson type equation (2.7) is the key to solve the inductions. By neglecting the second order terms, a f_x - and f_y -relative linear solver is obtained. In other words, the relationship between the pressure jump and the first-order body force is yielded. Once the pressure field has been determined, the inductions could be found by integrating Eq (2.6). Eq (2.4) shows that the pressure jump depends on the blade force, which is calculated with the induction. Thus, an iteration is thus mandatory for implementation. This would be further explained in Section 3.3.

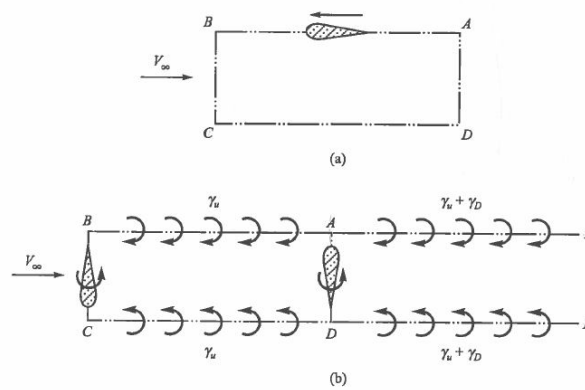


Figure 2.8: The schematic diagram of the fixed wake model[27]

2.2 The kinematic models

All the actuator models except AC are on the basis of one-dimensional momentum balance. This assumption is crippled for highly loaded rotor. Further, v_w is defined as far wake velocity profile in actuator models, no information about the near wake at all.

The above drawback is exactly one of the advantages of the vortex models, which accounts the vortex evolution in both blade and wake in terms of Lagrangian approach. For a VAWT, AOA remarkably changes with the time, resulting in varying bound vortex. Thus, it is essential to enclose the time step for vortex models.

2.2.1 The fixed vortex model

The fixed vortex model was proposed in 1981 by Wilson and Walker in [27], and considered as a combination of SST and vortex theory.

As shown in Figure 2.8, the blade is moving along A-B-C-D path, the vorticity is only shed when the airfoil changes its moving direction, and then the vorticity would be convected downstream. The sign of the shed vorticity at B and C are opposite because the changing direction also opposites mutually. The bound circulation on the blade depends on the vortex sheet strength, downstream velocity and the frequency of changing direction.

The region A-B-C-D is similar to the expanding region (near actuator disk) in SST. The induction here is denoted as a_u while the region A-D-E-F is considered as far wake area, with a new induction a_D . The reason for the dividing is that A-D is on the blade path, a velocity jump exists and new vorticity shed here, thus causes the change vortex sheet strength and the induction in far wake region as seen in Figure 2.8. A relation is valid in this system $a_D - a_u = a$, with a is the induction obtain in SST.

However, since the initial induction factor is worked out from SST, and the fixed wake model is considered as an out-of-date model, no further investigations and improvements have been carried out.

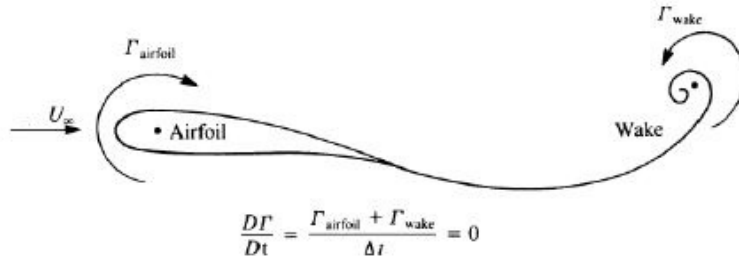


Figure 2.9: The Kelvin theorem

2.2.2 The free vortex model

According to the Kelvin theorem, the change of circulation in time has to be constantly equal to zero [14]. Hence for an ideally stationary velocity field and relatively motionless airfoil, there is only one bound lifting vortex at $\frac{1}{4}c$ and a shed vorticity at $t=0$ when the velocity suddenly appears. However, for a VAWT where AOA constantly changes during the spinning, normally this would lead to a time-dependent lift. This also means a varying circulation of bound vortex since the lift is expressed as below according to Kutta-Joukowski [2].

$$L = -\rho v_0 \Gamma \quad (2.8)$$

Therefore, another vorticity with same strength but opposite sign would be released in the wake at $\frac{1}{4}c$ after the trailing edge and convect with the wake speed as seen in Figure 2.9. This shed vorticity will be convected downwind. Thus, its induction on the blade would decrease with increasing distance as implied in Eq (2.9).

For a wind turbine blade, it could be replaced by one or a series of lifting line following the wake vorticity in a vortex model. It is optional to discretize the blade. For a real wind turbine, whatever HAWT or VAWT, bound lifting vortex usually varies along the blade due to different local relative speed and sometimes sectional chord length as seen in 2.10. However, for our case the simplified straight H-rotor the one is considered as constant.

Kelvins theorem requires to have a closed surface. Therefore, to connect the lifting line and the wake vorticity line, two side filaments are introduced so as to form a closed vortex panel.

For a filament with constant vortex strength/circulation Γ , its induced velocity at arbitrary point \vec{x}_p can be expressed analytically as

$$\vec{u}_\Gamma(\vec{x}_p) = \frac{\Gamma}{4\pi} \frac{(r_1 + r_2)(\vec{r}_1 \times \vec{r}_2)}{r_1 r_2 (r_1 r_2 + \vec{r}_1 \cdot \vec{r}_2)} \quad (2.9)$$

where r_1 and r_2 are the vectors from the vortex line start and end point to \vec{x}_p . The induced velocity field around the filament is illustrated in Figure 2.11. The boundary condition to determine the local velocity and vortex strength is the impermeability condition at the control point ($\frac{3}{4}c$), which means the normal velocity component at this point is zero. Forming the filament together as several vortex panels in a discretized blade then it becomes what is showing in Figure 2.12. Thus the vortex strength of each panels are

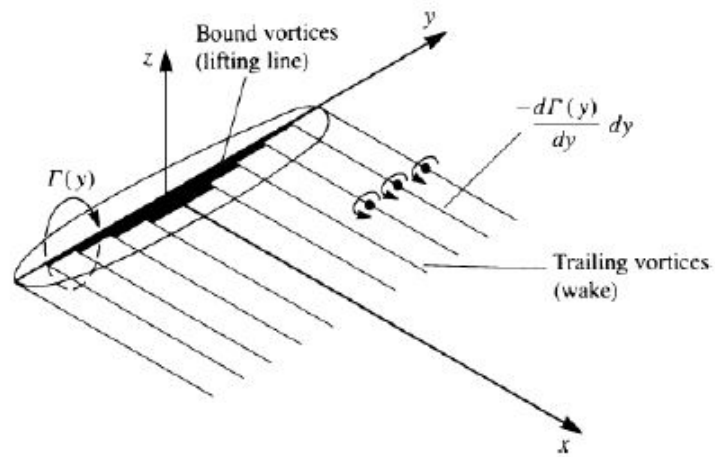


Figure 2.10: The lifting line vortex model discretization

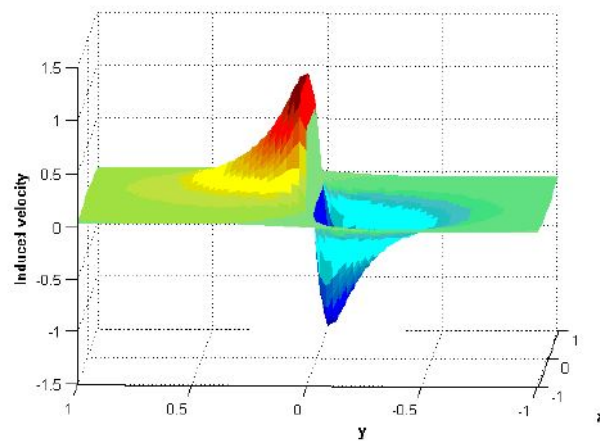


Figure 2.11: The induced velocity profile by a single filament

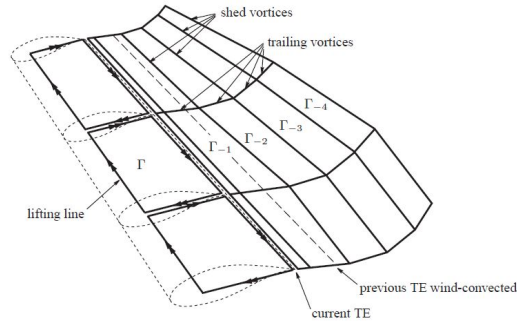


Figure 2.12: The vortex panel

individual. At each time steps, a new vorticity shed (or another row of panels are produced), joining the wake vorticity and together affect the velocity field. In other words, the implementation is sensitive to the time steps.

For a VAWT, the issues are not only the evolving AOA, but also that the blade (or bound lifting line) would pass its own wake during the rotation. C.S. Ferreira[40] has stated that for an airfoil section, the total circulation is the summation of the circulation due to the several perturbations as expressed in Eq (2.10),

$$\Gamma_{airfoil} = \Gamma_{induced,other,aerofoils} + \Gamma_{relativewind} + \Gamma_{induced,wakes} + \Gamma_{displacement} \quad (2.10)$$

Among them, airfoil displacement circulation is the only constant term since the turbine rotates at a constant rotational speed.

2.3 CFD models

With the booming of the computational ability of the computer, CFD solvers have become a high-end tool to investigate the VAWT aerodynamics because it is capable to demonstrate the whole picture of the flow field.

The first step of CFD scheme is the mesh setting-up/discretization in the evaluation domain, those meshes are physically treated as control volumes. In this phase, Finite Volume Method is commonly employed.

As for the boundary condition on the domain, it is optional to start with the values at the wall of the domain(Dirichlet boundary condition) or its flux(Newman boundary condition). For example, for the impermeability condition at airfoil surface.

CFD models are sometimes also called NS models since the most commonly applied physical models in the control volumes are Navier-Stokes equation, which is usually employed along with the continuity equation. For in-compressible flow, they are expressed as

$$\rho\left(\frac{\partial \vec{v}}{\partial t} + \vec{v} \cdot \nabla \vec{v}\right) = -\nabla p + \nabla \cdot \vec{\tau} + \vec{f} \nabla \vec{v} = 0 \quad (2.11)$$

After defining the physical modeling (theoretical equations), the solving process could be launched. Usually, it starts from the wall to the center, from known to unknown. A conservation is valid both on the micro- and macroscopic, any of the flux flows out

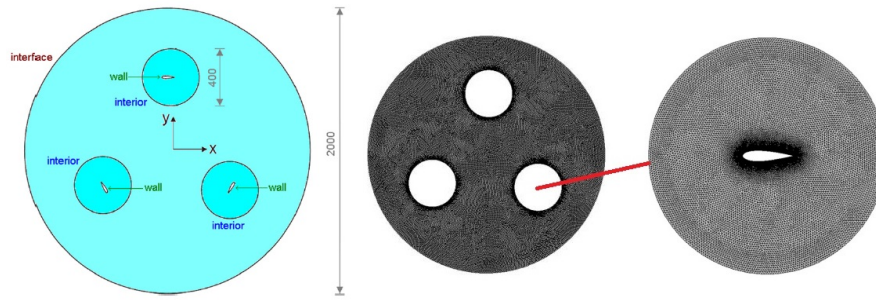


Figure 2.13: The subgrid scheme[30]

of the upstream volume equals to that flows into the downstream one, and similar for a tandem volume array(so-called global conservation). The process is so-called Direct Numerical Solution(DNS) since all the meshes are included. For VAWT flow field such a large project, it is rarely applied to solving all the fluid motions is a very computationally expensive. Two alternatives are available for reducing the computational efforts, they are Reynolds Averaged Navier Stokes solver(RANS) and Large Eddy Simulation(LES) respectively. RANS decompose the whole equation into the time-averaged part and the fluctuation part for better converge. However, it is only capable of solving the stationary flow otherwise the modeling is physically meaningless. LES simplified the problem using neglecting the effects of small eddies.

The irreplaceable advantages of CFD models are not only its high accuracy but also the ability on including dynamic stall and the possibility to exempt the airfoil characteristic data.

The impact of viscous effects of vorticity, has caused dynamic stall. The most visible phenomenon about that is the lower produced lift by the same AOA. Paraschivoiu has shown a remarkable trend of overestimating the power production by the negligence of the dynamic stall[27]. CFD models are also capable to include precisely the dynamic stall. Both momentum models and the vortex models are unavoidable from using the experimental airfoil characteristic. However, the error would occur because of the mismatch between the experimental Re number and the real one according to Paraschivoiu[27]. Madsen[20] also stated that it is questionable to use the steady experimental data in the unsteady environment. The issues are able to be overcome thanks to the inherent ability of the CFD code in determining the aerodynamic components of actions through the NS equations of the blade profile[30].

There is no need to investigate the whole field with equal precision. Thus, an unstructured mesh scheme is usually employed by means of the size function of the grid in order to reduce the computational time. The closer to the blade (the wall), the finer the meshes are, as shown in Figure 2.13. The mesh has to move with the spinning rotor. The moving mesh, in other words, means the mesh have to be re-new at every time step, as well as the following procedures. This remarkably increases computational cost. Sometimes too accurate modeling is not essential. Correctly modeling the structure of shed vorticity is unnecessary since only their influences on the turbine are interesting for us.

2.4 The comparison of the model performances

To sum up, the critical issues for modeling a VAWT are,

- Induction variation;
- Wake interaction;
- Lateral inductions;
- Dynamic stall.

A more detailed comparison concerning the cost performances is presented in Table 2.1. The complexity has been clarified in the model descriptions. The momentum models has the least computational cost because they concerned the time-averaged state, but AC model needs an iteration to determine the induction. Vortex models are time-dependent, and the shed vorticity is time-step-sensitive. Finally, CFD is a luxury option with the longest set-up and computational time.

Table 2.1: The model comparison

	SST	MST	DMST	AC	Free-wake Vortex	CFD
Complexity	Low	Low	Low+	Moderate-	Moderate+	Very high
Accuracy	Very Low	Low	Low	High	High	Very high
Computational effort	Low	Low	Low	Low	High	Very high

C.S. Ferreira and H.A.Madsen et al. have processed a comparison among the selected VAWT aerodynamic codes on single VAWT modeling in 2014, two typical test results on blade force are shown in Figure 2.14. U2DiVA, ARDEMA2D and CACTUS code are all free wake vortex model codes[10]. As seen in Figure 2.14, the curves of every model mutually agrees, except MST and DMST. Similar as the other tested results presented in [10]. Obviously, MST and DMST are neither considered as capable for single VAWT aerodynamic modeling due to the absence of lateral induction.

As a conclusion, AC model returns a very precise estimation with only a little computational effort. The success is mainly contributed by the identity between the its actuator geometry and real blade path. Therefore, AC model is selected for the following steps.

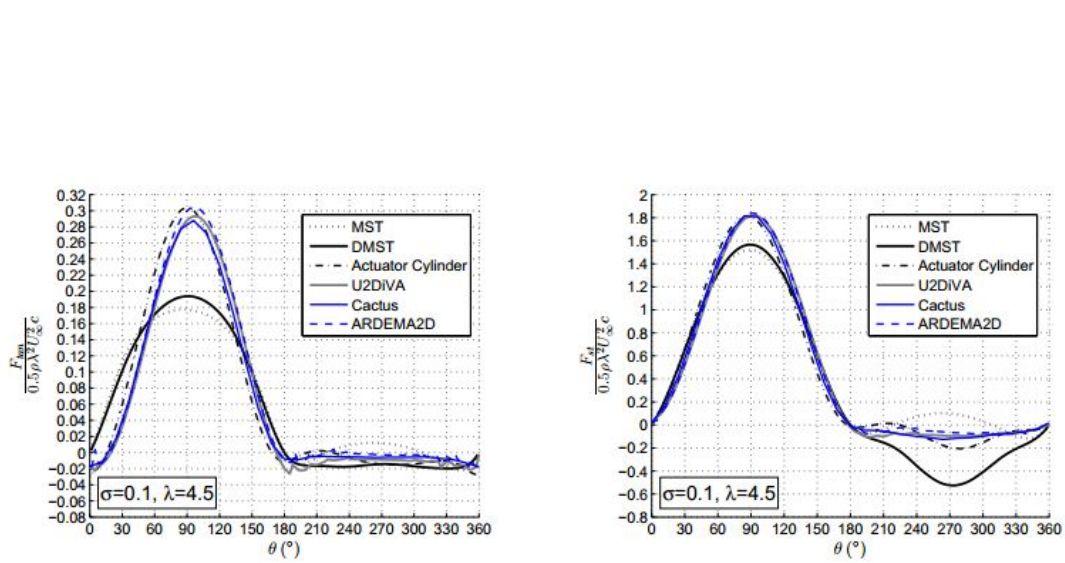


Figure 2.14: The model performances for the test case with $\lambda = 4.5$, $\sigma = 0.1$ and skew infow angle= 3° (Left: Tangential loads; Right: Streamwise load)[10]

The implementation of the linear version AC model

Actuator Cylinder model has been chosen to be integrated in HAWC2, a wind turbine aeroelastic code developed by DTU-Risø.

From this Chapter, AC is employed as the numerical tool to model a VAWT. Although HAWC2 is has been proven to work correctly, it is considered as too complicated to handle within the limited working time. In particular, a portable and easily assessed code is more suitable for such an innovative reserch where intensive “try-out” and bringing new variables are required. Given all that, Matlab, the handy and familiar tool is a better option.

The main purpose of the following text is to introduce the process on how the linear version AC model with MOD-LIN correction is constructed in Matlab, which is presented in Section 3.3. To validate the routine, the simulations for a common case (Section 3.1) are carried out by both HAWC2 and Matlab, and the results are mutually compared (Section 3.5).

Although HAWC2 model set-up will not be discussed until Section 6.1, some issues for HAWC2 model especially the coordinating system is presented in Section 3.4. In addition, Section 3.2 explains the idea behind MOD-LIN as a supplemente.

3.1 The description of modeled rotor

The given parameters are summarized in Table 3.1. The exactly same rotor is going to be modeled in both Matlab and HAWC2 in order to be comparable. Prevailing wind v_∞ is from the left, the definition of the azimuth angle θ is illustrated in Figure 3.1 with some rough region distinction.

Table 3.1: Modeled rotor

Rotor geometry					Airfoil		External condition		Variable
B	R	σ	H	type	C_l	C_d	ρ	v_∞	TSR
3	1m	0.1	2m	H-rotor	$2\pi \sin(\alpha)$	0.023	1.225 kg/m^3	9m/s	

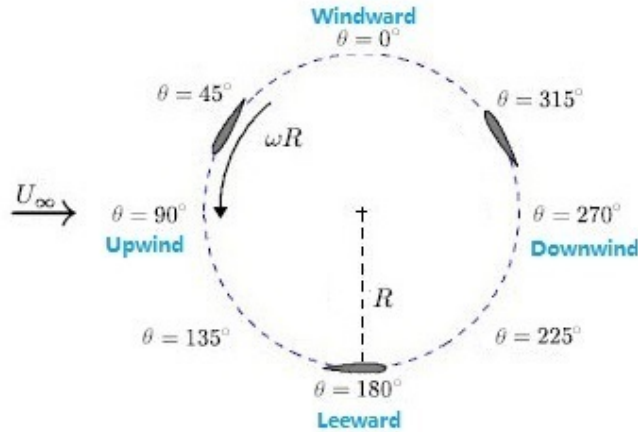


Figure 3.1: The azimuth position definition (Modified from [40])

3.2 Modified linear version (MOD-LIN) AC model

Madsen[21] brought up an empirical modification for correcting the problem of linear AC on overestimation on high load case. It is worth notable that C_T even exceeds 1 for high loading, which is physically impossible.

Therefore, the modification is based on the thrust coefficient. The correction factor in (3.9) is obtained based on the two different relations between C_T and induction a obtained from a uniform loading solution, and BEM, respectively.

$$\begin{aligned} C_T &= 4a_{lin} \\ C_T &= 4a - 4a^2 \end{aligned} \quad (3.1)$$

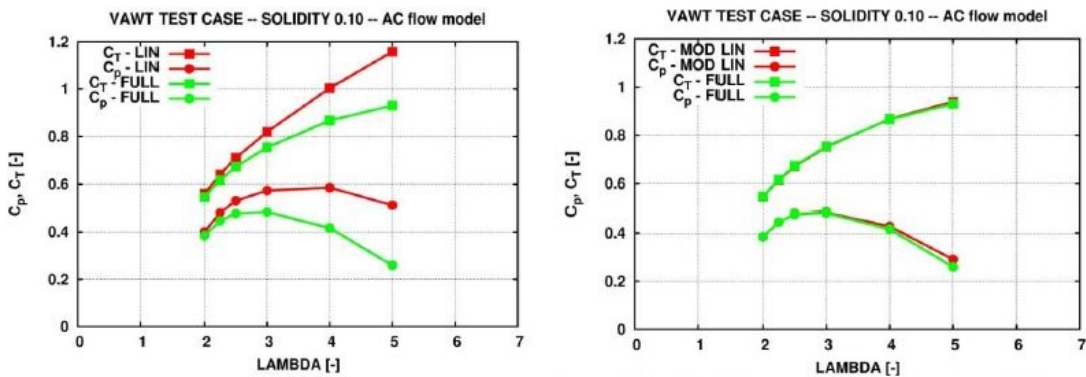


Figure 3.2: The aerodynamic coefficients before and after MOD-LIN [21]

The Actuator Cylinder model shows increasing C_p with increasing C_T , while the other models show a decreasing C_p with increasing C_T after the maximum C_p [10]. The reason for this behavior is probably that MOD-LIN is not as effective as in low loading cases at the very high loading(see Figure 3.2).

3.3 Implementing MOD-LIN AC in Matlab

A linear version AC model is implemented for its simplicity by avoiding to solve the Poisson equation in the non-linear solution. Recall the Poisson type equation (2.7), which connects the volume force and the first-order induction terms, it is very clear that we have to calculate the loading on the control volume in order to obtain the velocity. Here are the key steps on the implementation.

It is mandatory that the discretization should start with a non-zero point, skip 180° and be symmetric about the diameter line $0 - 180^\circ$. Otherwise, there is no grantee that the summarized scheme in Table 3.2 works correctly.

In the simulations, typically a 36-element mesh is applied one the cylinder with the starting point at $\theta = 5^\circ$. So do the evaluation points, because we usually evaluate also at a circle where the specific points share the same azimuth position as the cylinder in order to simplify the problem. The coordinates of the evaluation points (x,y) are obtained from

$$\begin{aligned} x(j) &= -R_{eva}\sin(\theta(j)) \\ y(j) &= R_{eva}\cos(\theta(j)) \end{aligned} \quad (3.2)$$

with $j=1,2,3,\dots,36$.

The influence coefficients stand for the different influences from and at different points. As there are 36 points in our case, R_{w_x} and R_{w_y} are both 36×36 matrices, and only location-sensitive.

$$\begin{aligned} R_{w_x}(i,j) &= - \int_{\theta-\frac{1}{2}\Delta\theta}^{\theta+\frac{1}{2}\Delta\theta} \frac{-(x(j) + R\sin(\theta))R\sin(\theta) + (y(j) - R\cos(\theta))R\cos(\theta)}{(x(j) + R\sin(\theta))^2 + (y(j) - R\cos(\theta))^2} d\theta \\ R_{w_y}(i,j) &= - \int_{\theta-\frac{1}{2}\Delta\theta}^{\theta+\frac{1}{2}\Delta\theta} \frac{-(x(j) + R\sin(\theta))R\cos(\theta) - (y(j) - R\cos(\theta))R\sin(\theta)}{(x(j) + R\sin(\theta))^2 + (y(j) - R\cos(\theta))^2} d\theta \end{aligned} \quad (3.3)$$

The aerodynamic loads and resultant velocity are all AOA-dependent. One of the most remarkable differences of VAWT from HAWT is the varying AOA during the rotation. Thus AOA in certain position can only be obtained based on computed local relative velocity. Since the actual velocity field is an unknown, or specifically, the inductions in both direction(w_x and w_y) are unknown, an iteration procedure is necessary.

$$\begin{aligned} v_{rel,x} &= v_\infty + \omega R\cos(\theta) + v_\infty w_x \\ v_{rel,y} &= \omega R\sin(\theta) + v_\infty w_y \\ v_t &= v_{rel,y}\sin(\theta) + v_{rel,x}\cos(\theta) \\ v_r &= -(v_{rel,y}\cos(\theta) - v_{rel,x}\sin(\theta)) \\ \alpha &= \tan^{-1}\left(\frac{v_r}{v_t}\right) \end{aligned} \quad (3.4)$$

According the AOA computed in Eq (3.4), the blade forces are obtained as

$$\begin{aligned} F_n(\theta) &= \frac{1}{2}\rho v_{rel}^2 c C_n(\alpha) \\ F_t(\theta) &= \frac{1}{2}\rho v_{rel}^2 c C_t(\alpha) \end{aligned} \quad (3.5)$$

with the normal and tangential load coefficients are originated from the airfoil characteristic,

$$\begin{aligned} C_n &= C_L \cos(AOA) + C_D \sin(AOA) \\ C_t &= C_L \sin(AOA) - C_D \cos(AOA) \end{aligned} \quad (3.6)$$

The load coefficients are physically the pressure jump on the surface expressed in Eq (2.4). This is the result of the impact from the blade forces. The idea behind the formula (3.7) is that the pressure is the fraction between force and the acting area. Noting that the term ρv_∞^2 in denominator non-dimensionalized the formula, thus Q_n and Q_t are both dimensionless.

$$\begin{aligned} Q_n(\theta) &= \frac{BF_n(\theta)}{2\pi R \rho v_\infty^2} \\ Q_t(\theta) &= -\frac{BF_t(\theta)}{2\pi R \rho v_\infty^2} \end{aligned} \quad (3.7)$$

So far, the needed loads are known, we could start estimating the velocity. Neglecting the second-order terms g_x and g_y from the Poisson type equation (2.7), the inductions are analytically expressed as

$$w_x(j) = \frac{1}{2\pi} \sum_{i=1}^{i=N} Q_{n,i} R_{w_x}(i, j) + w_x(j)^* w_y(j) = \frac{1}{2\pi} \sum_{i=1}^{i=N} Q_{n,i} R_{w_y}(i, j) \quad (3.8)$$

The star term $w_x(j)^*$ is the extra terms adding in $w_x(j)$, represents adding the pressure jump effects in the axial induced velocity. Not only the influences come from the cylinder, but also the direct effects in the pathway should be included. The star term $w_x(j)^*$ varies with the evaluation position summarized in Table 3.2. This is the way how AC includes the wake interaction. Let us take a 36-points scheme which is conducted in HAWC2 as

Table 3.2: The start term $w_x(j)^*$

Inside the cylinder	$j=1-N/2$	0
	$j=N/2+1-N$	$Q_{.n}(j)-Q_{.n}(N+1-j)$
Outside the cylinder	$j=1-N/2$	$-Q_{.n}(j)$
	$j=N/2+1-N$	$-Q_{.n}(N+1-j)$

an example. For a streamline go through the evaluation point $j=35$ outside the cylinder, downstream, it has to firstly passes by the cylinder surface twice at the elements $j=2$ and $j=35$.

One should be pointed out is $j=1-18$ and $j=19-36$ actually stand for the upstream and **wake region**, accordingly. In our case, only the loads near the cylinder is attentive, thus defining $j=19-36$ elements as wake region is correct here. The cylinder surface is

a critical region since it is hard to judge whether the load coefficient terms should be deducted or not. Thus, setting the evaluation radius as 1.01R or 0.99R is recommended if one wishes to approach the loads on the blade path. That is exactly what we did in the implementation.

To better demonstrate the train of thought behind the modeling, a brief flow chart is presented in Figure 3.3.

Now, it is the time to introduce MOD-LIN correction. An empirical modification factor k_a has been introduced to multiple the induction w_x and w_y during the iteration so as to improve the linear solution without increasing computational efforts

$$k_a = \frac{1}{1 - a} \quad (3.9)$$

Finally, the most concerned parameter C_T and C_p are calculated as [1]

$$\begin{aligned} C_T &= \int_0^{2\pi} Q_n \sin(\theta) + Q_t \cos(\theta) d\theta \\ C_{p,ideal} &= \int_0^{2\pi} Q_n v_n d\theta \\ C_{p,real} &= \frac{\frac{1}{2\pi} \int_0^{2\pi} B(F_t \omega R) d\theta}{\frac{1}{2} \rho v_0^3 2R} \end{aligned} \quad (3.10)$$

The ideal power coefficient is based on the inductions on the cylinder surface, while the real one is calculated according to the torque. Theoretically, $C_{p,real}$ is supposed to be less than $C_{p,ideal}$, because not all the pressure on the cylinder surface has been converted to the power.

3.4 The implementation in HAWC2

The given H-rotor model is also implemented in HAWC2 where a MOD-LIN AC is integrated in order to validate the accuracy of Matlab code. To be more comparable, dynamic stall, tip loss and tower shadow etc. are excluded, the structure stiffness of each body is intentionally set at an unusually high value.

The global coordinate system with the local coordinate constrained in blade in HAWC2 illustrated in Figure 3.4 differs from Matlab model. Z direction is defined as the gravity direction, and x-direction is pointing against the free stream. For the blade coordinates, x-axis parallel with the chord-wise/tangential direction.

Moreover, the initial position of blade 1 is on the exact left(downwind) and it spines along clock-wise. Both are totally different from the ones in Matlab model(see Figure 3.1), hence a phase lag between HAWC2 and Matlab curve exists for every diagram.

Also, each structure body is modeled as arbitrary numbers of un-deformable Timoshenko beams with given structural characteristic in HAWC2. The macroscopic deformation is modeled by the bending of the Timoshenko beams. For pure aerodynamic problem, the stiffness is set at high value as mentioned in order to provide a full-rigid turbine.

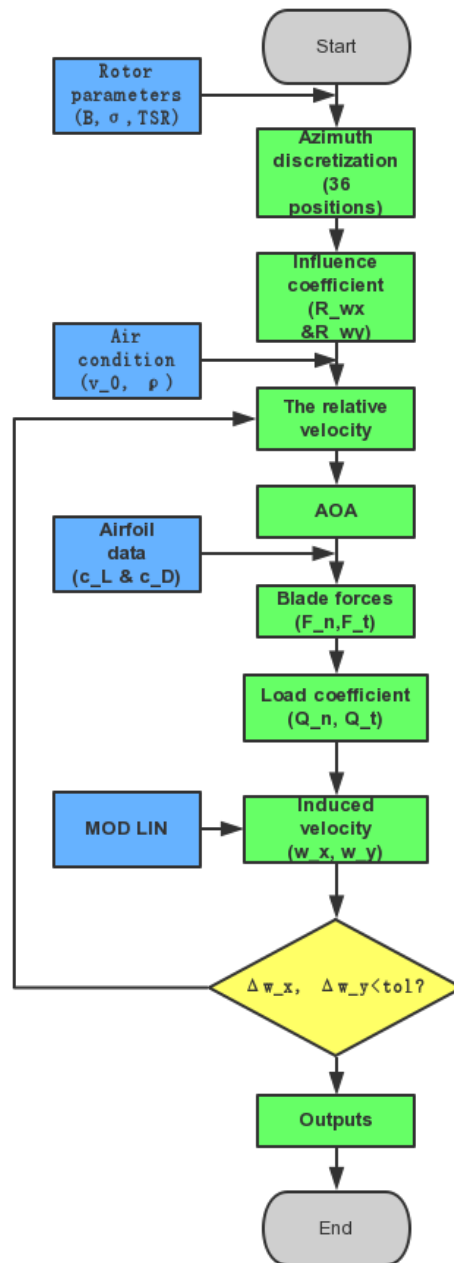


Figure 3.3: The flow chart on AC modeling in Matlab

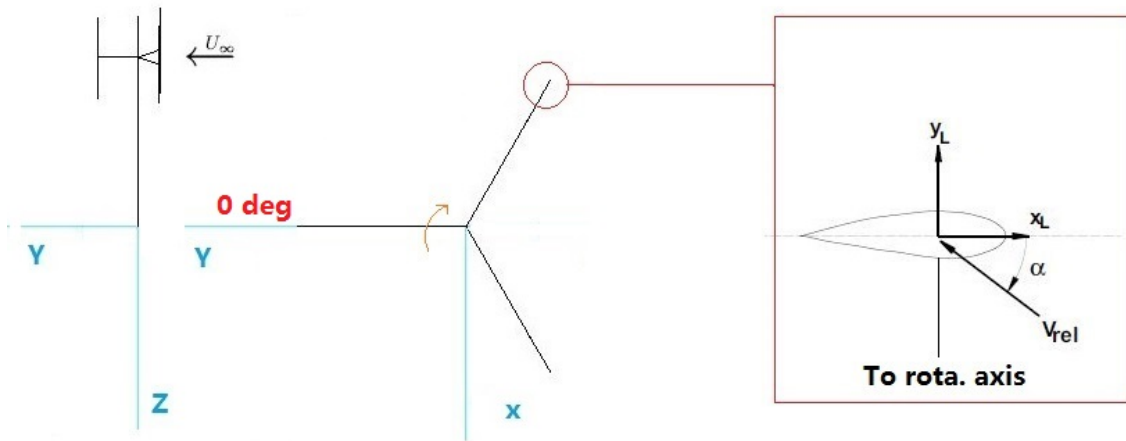


Figure 3.4: The coordinate system in HAWC2 [21]

3.5 The validation

3.5.1 The results

Both the thrust and power coefficients (see Figure 3.5) from Matlab model agree with those from HAWC2. As shown in Figure 3.6 and 3.7 demonstrate the comparison of the streamwise and lateral inductions, respectively. The one obtained from HAWC2 is actually the instantaneous value at $t=18s$, when the flow field is stationary. Thus there is no misalignment but a slight shift among the curves. This is partly because of the different evaluation position in HAWC2 for the global parameters such as the inductions and the load coefficients.

Generally, the blade force curves mutually agrees to each others as shown in Figure 3.8 and 3.9. However, some disturbances are observed the downwind side, which is not solved in the end.

3.5.2 Comments

In conclusion, based on the results shown from Figure 3.5 to 3.7, the linear version Matlab model is working in a correct way. It shows a general identity with HAWC2 results, even though some small deviations are also observed.

In addition, my colleague Sercan Ertem also conducted MOD-LIN AC in Matlab. His results agree with mine but differs from HAWC2 results as seen in Figure 3.10. Hence it is more likely the other sub-routine of HAWC2 has caused the slight disagreement.

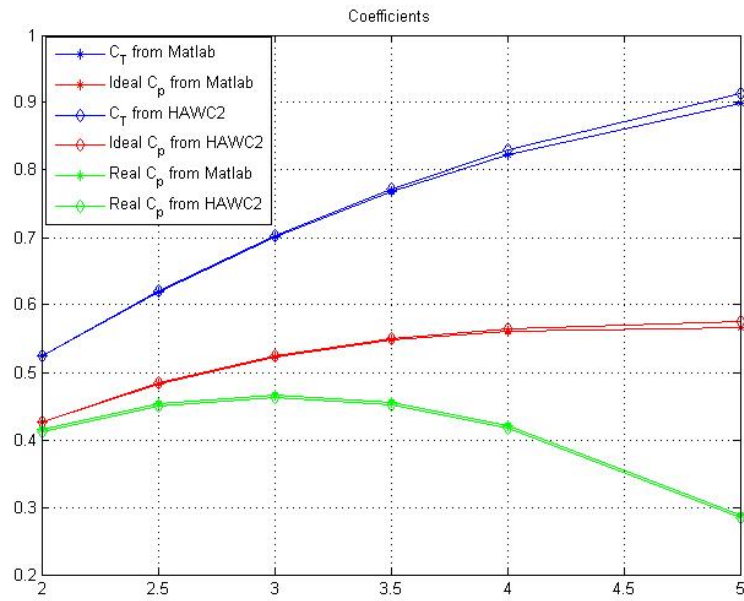


Figure 3.5: The power and thrust coefficients

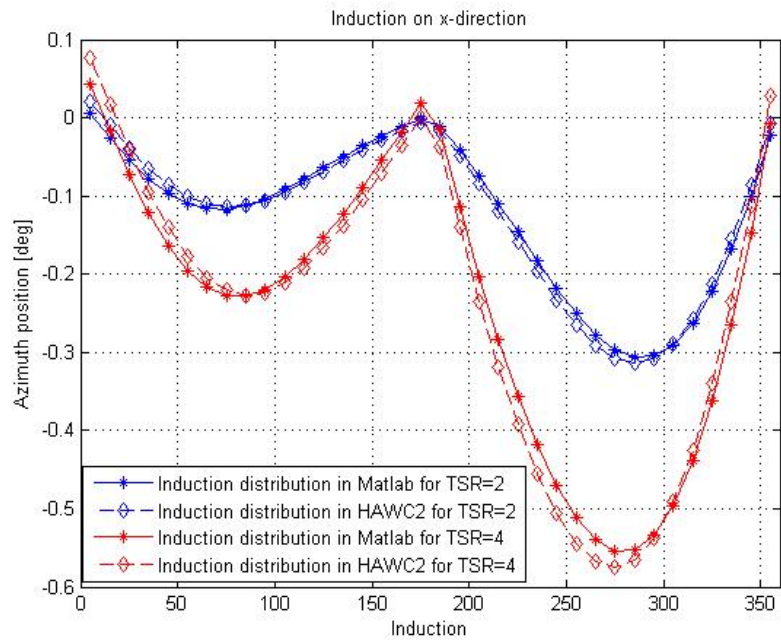


Figure 3.6: The induction on x-direction distribution

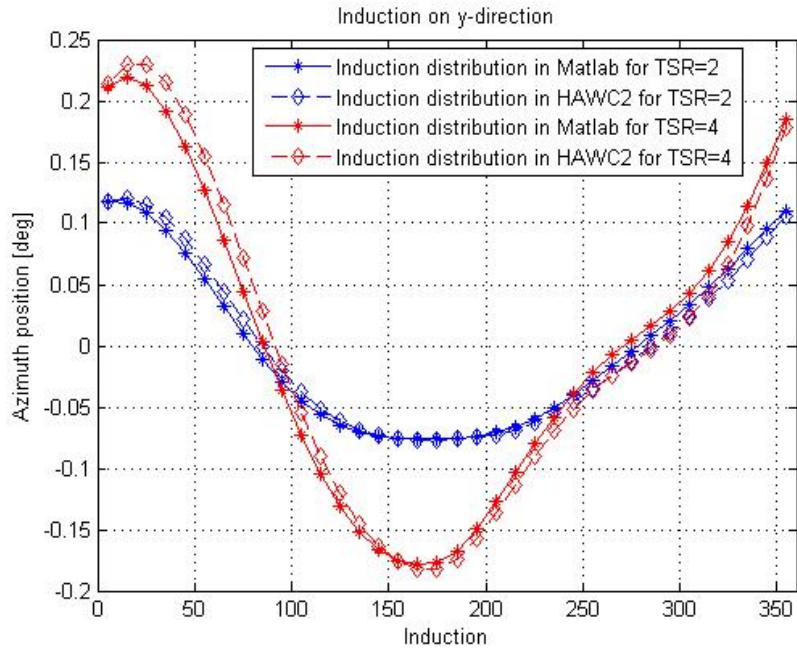


Figure 3.7: The induction on y-direction distribution

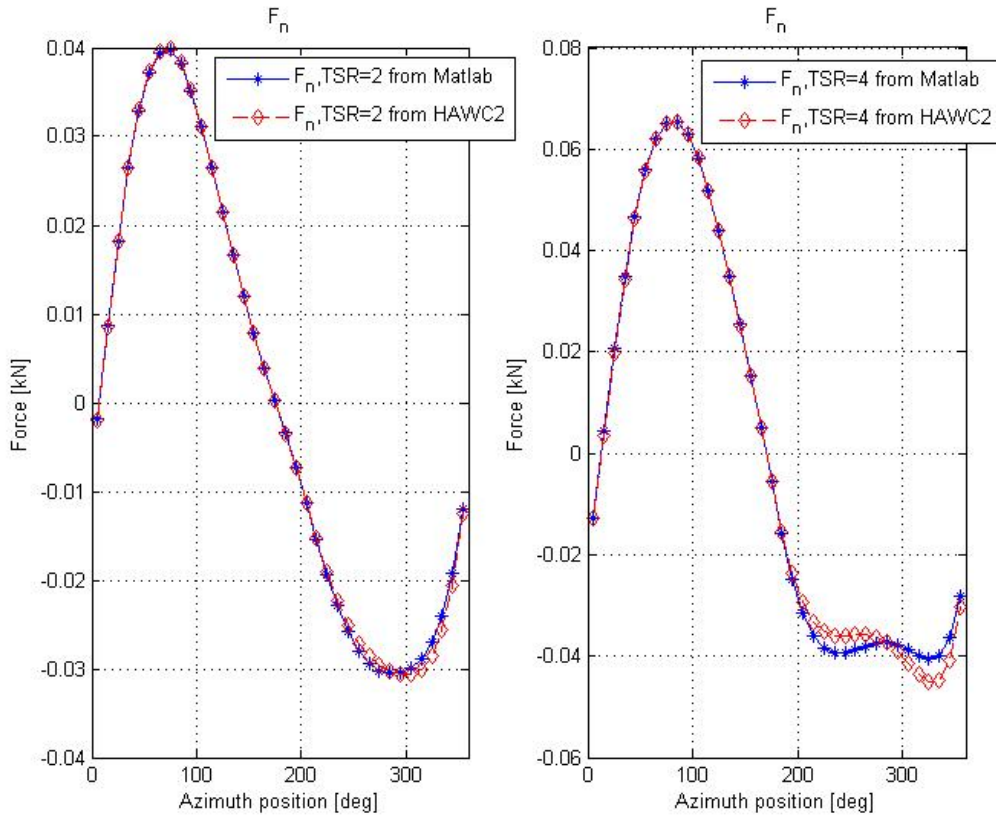


Figure 3.8: F_n for TSR=2& 4

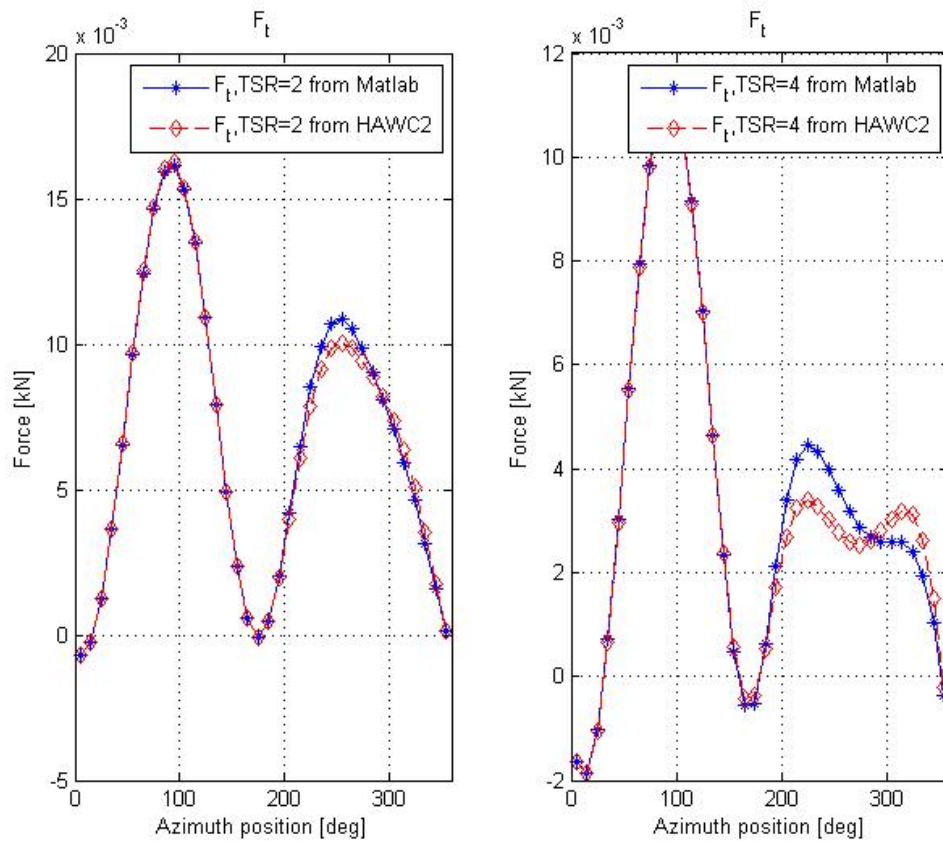


Figure 3.9: F_t for TSR=2& 4

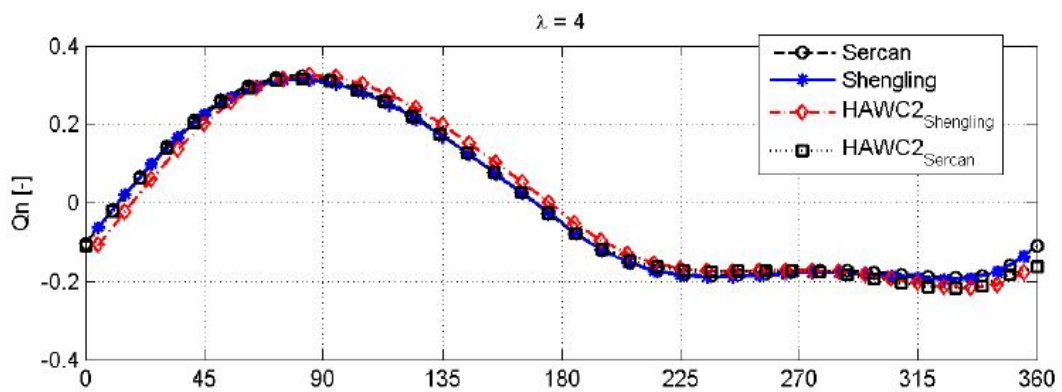


Figure 3.10: A comparison performed by Sercan

Dynamic stall theory and modeling

Dynamic stall by definition is a stall phenomenon that the aerodynamic coefficients become time-dependent. It will occur on any lifting surface when it is subjected to any unsteady motion such as pitch and heave[25]. The first analytical dynamic stall models were introduced in late 70s[13]. Originally, the dynamic stall was studied within helicopter-related fields. However, it can be also observed in wind turbines, particularly VAWT.

During any of the revolutions, VAWT blades experience a remarkable variation on AOA, thus dynamic stall is expected to occur frequently. Zanon et al. [47] has proved that dynamic stall impacts the design and operation of VAWTs, particularly power and load control at low TSRs. For wind farm design, it was shown that dynamic stall can affect wake recovery and thus wind farm power control. Therefore, a dynamic stall model is mandatory if one wishes to estimate a VAWT more accurately, not to mention that flap impacts are taken into account in this case.

ATEFlap is developed by Bergami and Gaunaa and has been integrated into HAWC2[5]. It is an engineering model coupling a potential flow solution with a Beddoes-Leishmann dynamic stall model for a deformable trailing edge or flapping airfoil. This is one of the prerequisites for performing this research. In the following subsections, the discussion is mostly on ATEFlap related theory background.

The model requires the airfoil aerodynamic coefficients at various angles of attack, as well as the coefficient variations caused by steady flap deflections as input. Section 4.2 shows how the clean airfoil data is expanded by adding the flap impacts. As two integrated theory content of the model, the potential flow solution, and the dynamic stall estimation procedure are also presented in Section 4.3 and 4.2, respectively.

All the theory and operation stated below refers to ATEFlap version 2.05

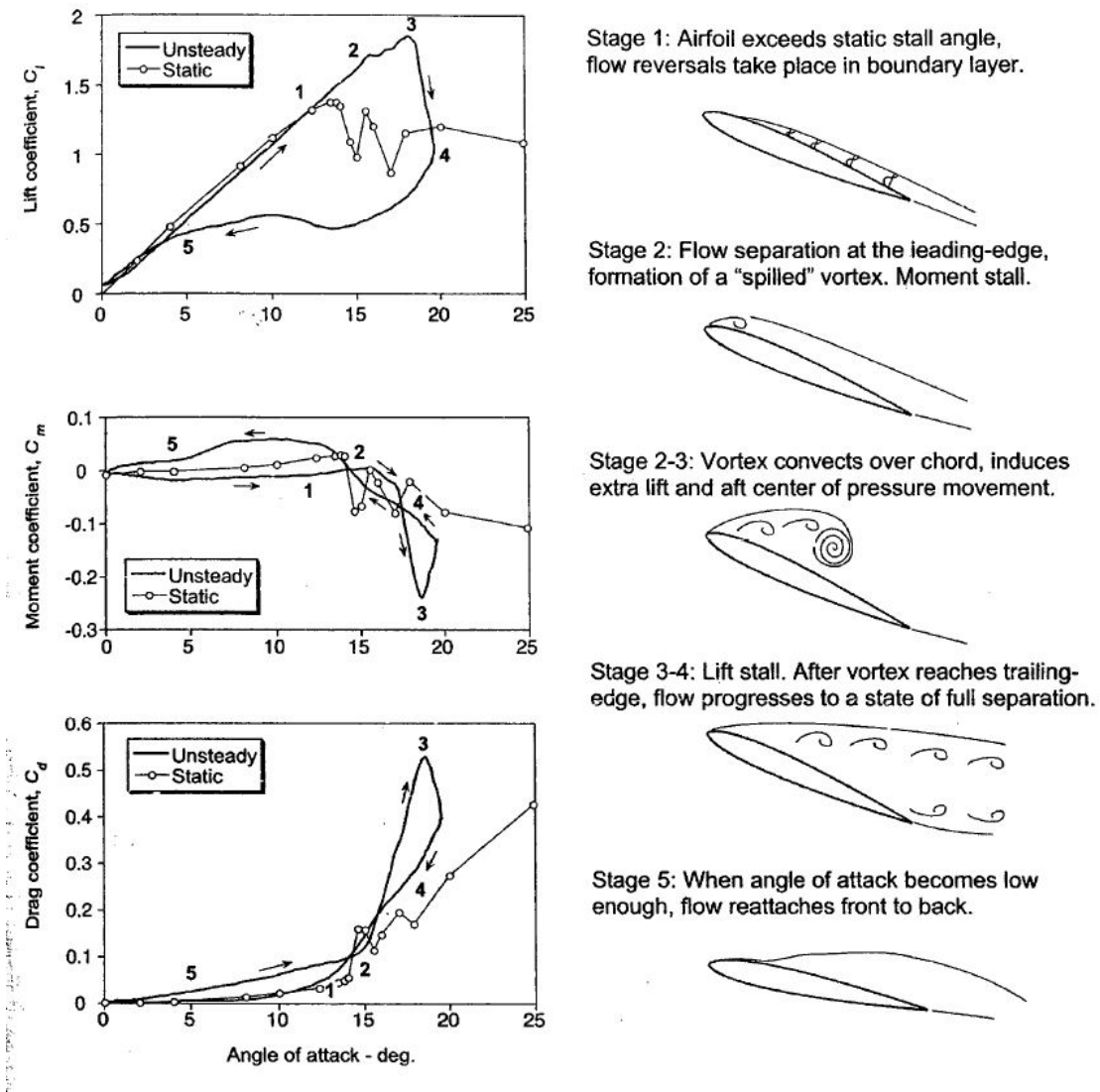


Figure 4.1: The process of dynamic stall[18]

4.1 A brief introduction to dynamic stall

The straightforward reflection on $C_L - AOA$ curve is that there are more than one corresponding C_L for a fixed AOA, higher or lower than the original when AOA varies in a certain high frequency (see Figure 4.1). The reflection is similar to Theodorsen effect. The dynamic stall is characterized by the shedding and convection of a vortex-like disturbance over the suction side[27], while Theodorsen effect happens in the purely attached flow where the lift response lags the rapid change of AOA[15].

According to Leishman[18], the process of the dynamic stall is depicted in Figure 4.1, with its impacts on all the coefficients. During a fast upstroke motion (nose up) that is beyond the static range, the flow stays attached even though the reversals already occur inside the boundary layer (Stage 1). Before long, a vortex develops at the leading edge at the beginning of Stage 2, and convects along the blade surface (Stage 2-3). This induces

both additional lift and drag that even exceed their static values but a break of C_m . After the moment that the vortex finally arrives at the trailing edge (Stage 3), a full separation occurs. The vortex is then shed into the turbulent wake (Stage 3-4) and results in a sudden drop of C_l and C_d . The aerodynamic circumstances is now approximately the same as the stall in quasi-steady conditions. Paraschivoiu[27] indicates there might be some weaker secondary vorticities that result in disturbances of those coefficients. However, the airfoil will not obtain a C_l as high as the corresponding steady value until the airfoil is reset to an AOA that is below its normal stationary upper-limit (Stage 5). That is exactly why all the aerodynamic coefficients cannot be back to the steady value before reaching the certain AOA.

Dynamic stall is still not fully understood although it has been intensively studied. Luckily, engineers do not wait until all the physics are clarified before putting their hands on modeling dynamic stall[24][18].

As discussed in Chapter 2, despite CFD models that provides a good insight of the physics exist, a Semi-Empirical model is actually a preferred option. One of the most popular is Beddoes-Leishmann model because of its completeness. It has adapted in ATEFlap.

All in all, the whole process of dynamic stall consists of the flow separation, vortices shedding and the delayed reattachment, hence it seriously influences the loading and power output of a VAWT. As the AOA experienced by the blades increases with the decreasing TSR, dynamic stall becomes increasingly important at lower TSRs (will be presented in Chapter 5).

In addition, Scheurich[37] claims that dynamic stall can also occur at high TSRs when the AOA is locally increased by interactions between the blades of the rotor and the vortices within the wake generated by the turbine.

4.2 The airfoil aerodynamics

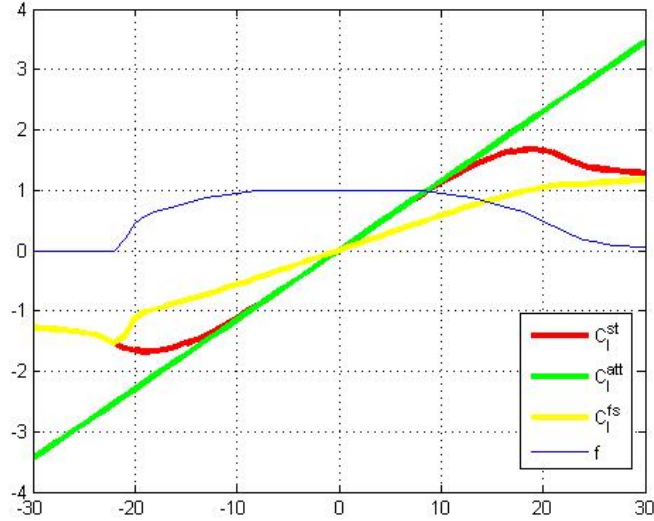
4.2.1 The airfoil selection

The load-form study presented in Chapter 5 is rotor-dependent. Hence, it is crucial to select a representative rotor geometry. Considering the circular routine of a blade, it is a wise choice to select a symmetrical airfoil to guarantee a homogeneous behavior in up- and downwind side, the same as those Darrieus rotor in 80s. Furthermore, Beddoes-Leishman model is classical thin airfoil theory based, a practically thin airfoil is more preferred for a better estimation.

Even though a long flap is capable to cause a significant impact on the coefficients, a 10% length is chosen so as to be more realistic. Subsequently, the final selections are presented in Table 4.1. The desired airfoil data is obtained from Xfoil with Reynold's number $Re = 5 \times 10^6$.

Table 4.1: Airfoil data

Airfoil	NACA 0018
Flap length	10%
AOA range	$[-180^\circ \ 180^\circ]$
Flap range	$[-14^\circ \ 14^\circ]$

**Figure 4.2:** The decomposition of NACA0018 data

4.2.2 The static stall

The decomposition on C_l

The presenting model only counts trailing edge stall that is much more commonly seen in wind turbines.

Given a regular clean airfoil polar (steady values), the steady lift coefficient C_l^{st} is decomposed as the weighted sum of the ones of fully attach flow (C_l^{att}) and fully separated flow (C_l^{fs}),

$$C_l^{st} = C_l^{att} f^{st} + C_l^{fs} (1 - f^{st}) \quad (4.1)$$

where the weight parameter or separation function f^{st} indicates the degree of attached for the flow field. Physically, it stands for the fraction of chord-wise length where the flow is attached.

The linear range

Figure 4.2 illustrates all the components of Eq (4.1). It reveals that C_l can be described in a linear formula within the fully attached region ($f^{st} = 1$), as a function of both AOA

and β , expressed as,

$$C_l^{lin} = \frac{\partial C_l}{\partial \alpha}(\alpha - \alpha_0) + \frac{\partial C_l}{\partial \beta}(\beta) \quad (4.2)$$

where α_0 is defined as the AOA that returns null lift. For a symmetric airfoil, α_0 is expected to be about zero.

The separation function

One of the basic assumptions of B-L model is the separation function is evaluated based on the fraction between the steady and the linear lift coefficient,

$$f^{st} = (2\sqrt{\frac{C_l^{st}}{C_l^{lin}}} - 1)^2 \quad (4.3)$$

which is valid for the lift on a flat plate in a potential Kirchhoff flow[13]. Eq (4.3) implies an interesting fact, C_l^{st} is only a quarter of C_l^{lin} when it just arrives at fully separation ($f^{st}=0$). This is mutually confirmed with Figure 4.2.

The following equations illustrate how the lift coefficients are decomposed according to the known C_l^{st} and C_l^{lin} .

$$f^{st} = 1 \rightarrow \begin{cases} C_l^{att} = C_l^{st} \\ C_l^{fs} = C_l^{st}/2 \end{cases} \quad (4.4)$$

$$f^{st} = 0 \rightarrow \begin{cases} C_l^{att} = C_l^{st} \\ C_l^{fs} = C_l^{lin} \end{cases} \quad (4.5)$$

$$0 < f^{st} < 1 \rightarrow \begin{cases} C_l^{att} = C_l^{lin} \\ C_l^{fs} = \frac{C_l^{st} - C_l^{lin} f^{st}}{1 - f^{st}} \end{cases} \quad (4.6)$$

4.2.3 The pre-processor of ATEFlap

The general process

As a supplementary to the main routine, an external pre-processor is created to add the flap impact into the given airfoil polar. All the process presented in Section 4.2.2 is fulfilled by the program.

The pre-processor of ATEFlap counts the influence from both AOA and flap on the aerodynamic coefficients. In fact, it is the $\frac{\partial C_l}{\partial \alpha}$ and $\frac{\partial C_l}{\partial \beta}$ two slopes in Eq4.3 that the numerical tool estimates, so as to obtain C_l^{lin} for later steps.

The inputs and outputs are outlined here:

- Inputs 1: Clean airfoil data, the aerodynamic coefficients(C_l^{st} and C_d) as functions of AOA.

- Inputs 2: Flap steady variation (ΔC_l^{st} and ΔC_d) as functions of both AOA and β , bench-marked to those under $\beta = 0$.
- Intermediate parameter: C_l^{lin} (Eq (4.2)).
- Outputs: C_l^{att} , C_l^{fs} and f^{st} as functions of both AOA and β .

The outcome is presented in a form of a look-up table, a part of which of the given airfoil is enclosed in Appendix C.

Solving discontinuity

An iteration algorithm is carried out to look for $\frac{\partial C_l}{\partial \alpha}$ and α_0 at the same time. $\frac{\partial C_l}{\partial \alpha}$ is originally also flap-dependent, because the gradient is expected to change with different β . However, the contribution from β makes C_l^{lin} become non-linear even in the "linear" range, obeying the linear assumption. Hence an universal assumption $\frac{\partial C_l}{\partial \alpha}|_{\beta=0}$ is applied so as to eliminate the variable β in the end. Similar to the gradient $\frac{\partial C_l}{\partial \beta}$, it is computed at α_0 in order to eliminate the effect from AOA.

During the computation, the following factors might lead to the discontinuity. Thus, some adjustments are anticipated.

Eq 4.6 yielded through combining (4.1) and (4.3) gives rise to singularity points. Eq (4.6) occasionally defected due to the "cross-border" of f^{st} (out of [0 1]). This is caused by negative or excessive (≥ 1) fraction $\frac{C_l^{st}}{C_l^{lin}}$. In that case, f^{st} will be forced back in the the range accordingly.

C_l^{fs} is forced to be 0.5 C_l^{st} as prescribed by classical B-L model to smooth the curve. The input C_l^{st} sometimes does not entirely follow the linear trend even in fully attached flow, the instinct discontinuities might be amplified in the process. Hence, the suspicious points are usually found in $f^{st} = 1$. Some manual adjustments are required in this case.

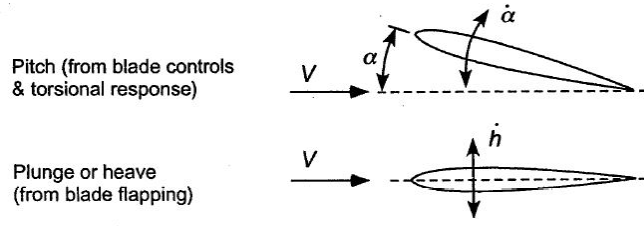


Figure 4.3: The airfoil movements[18]

4.3 ATEFlap solution for dynamic stall

Only two degrees of freedom the airfoil are considered, heave and pitch, as shown in Figure In one word, all the variation on these two motions are converted into the impacts on both α and β in ATEFlap to count the trailing edge flap. Hence the effective equivalent terms α_{qs} and β_{qs} are denoted in the following sections to include both the actual and induced variation.

Only the lift is detailed discussed in depth since the computational ideas for drag and moment are similar. The dynamic effects reproduced by the model is split into three categories:

- Non-circulatory terms(C_l^{nc}) is also known as added mass term, indicates the mass that accelerated by the airfoil movements.
- Circulatory terms($C_l^{Circ.Pot.}$ or $C_l^{Circ.Dyn.}$)
- Dynamic stall effect(Integrated in $C_l^{Circ.Pot.}$)

In the following context, only the basic ideas are emphasized. A few equations are displayed to support the arguments but without explanations. For more details, please refer to [5].

4.3.1 Potential flow solution

The potential flow part of the model is based on Gaunaa's solution for a thin airfoil undergoing arbitrary motion and camber-line deformation[11]. The model uses common potential flow assumptions, incompressible, irrotational and inviscid.

The potential flow solution consists of non-circulatory and circulatory components,

$$C_l^{Pot.} = C_l^{Circ.Pot.} + C_l^{nc} = C_l^{att}[\alpha_{eff}; \beta_{eff}] + C_l^{nc} \quad (4.7)$$

where the effective equivalent terms α_{eff} and β_{eff} is denoted as those transformed from α_{qs} and β_{qs} by including the wake memory effects.

α_{qs} and β_{qs} are defined as the terms including both the actual and induced variation,

$$\begin{aligned} \alpha_{qs} = \alpha_{3/4} = \alpha_{st} - \frac{1}{v_\infty} \dot{y} + \frac{(0.5 - \epsilon_{ea})b_{hc}}{v_\infty} \dot{\alpha} \\ \beta_{qs} = \beta - \frac{1}{v_\infty} \frac{H_y}{\frac{\partial C_l}{\partial \beta}} \dot{\beta} \end{aligned} \quad (4.8)$$

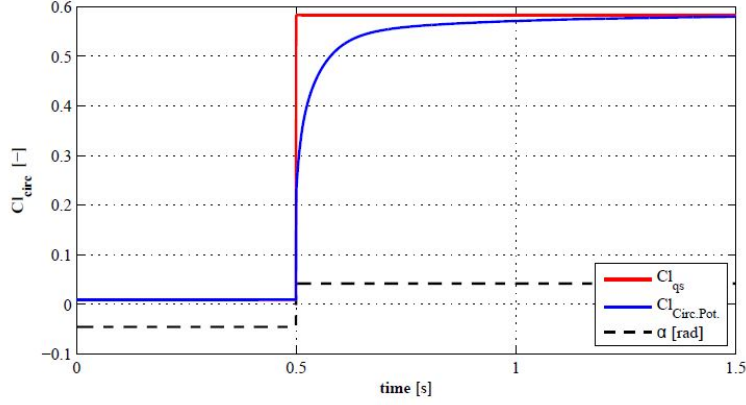


Figure 4.4: The effect from wake memory term[5]

For a one-vortex represented airfoil, the flow-tangency condition is satisfied only at the three quarter chord point[2]. Hence, it is usually taken as the evaluation point for AOA. According to Kelvin theory, a vorticity with the same strength as the change of bound vortex but opposite sign would be released into wake. The released vorticity would cause an equivalent effective downwash speed on the airfoil. It will not vanish until being convected into a far enough position with the wake flow. This behaves like a time-lag effect as shown in Figure 4.4.

4.3.2 Dynamic stall

Dynamic stall represents a shift variation of the coefficients. As indicated in Section 4.1, the induced vortex in dynamic stall start affecting the loading even before jumping into the wake. Furthermore, its impact presents a bounce-like pattern with a smaller time scale than wake memory term.

As mentioned, dynamic stall research firstly started from the helicopter aerodynamics. In that sense, they also include the effects of Mach numbers at which these helicopters operates, as well as a rather complex structure of the equations representing the time delays[8][15]. In ATEFlap, the adopted dynamic stall solution is from a reduced version of the B-L model at Risø National Laboratories(2004)[13], omitting the effects of compressible flow and leading edge separation.

The components of $C_l^{Circ.Dyn}$ are the same as Eq (4.7), but a weighted sum similar to the one in Eq (4.1) is introduced into the circulatory term,

$$C_l^{Dyn.} = C_l^{Circ.Dyn} + C_l^{nc} = C_{l,}^{att} f^{dyn} + C_l^{fs}[\alpha_{eff}, \beta_{eff}](1 - f^{dyn}) + C_l^{nc} \quad (4.9)$$

where the weight parameter f^{dyn} accounts for trailing edge separation dynamics. f^{dyn} is very similar to f^{st} , but standing for a separation in the dynamic operation.

The idea of modeling dynamic stall is lagging the coefficients from the quasi-steady. The typical lag in the airfoil stall is a direct consequence of the flow separation delay. As shown in Figure 4.5, a sudden increased AOA corresponding to a decrease in lift in steady condition, it initially raises the lift before the stall in fact. In this phase, pressure lag time constant T_p and boundary time constant T_f are introduced. They physically describe the

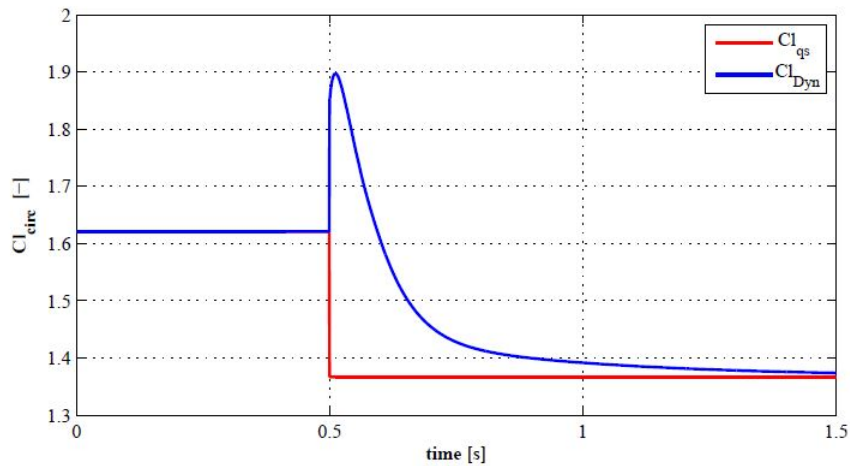


Figure 4.5: The effect from the dynamic stall term[5]

time for pressure field to react for the movement and the boundary layer rebuilt time, respectively.

As a result, the time-dependent factor f^{dyn} counts the stall delay phenomenon is computed. Compared with the wake memory in potential flow, the dynamic stall variation is more swift but long-lasting.

4.4 The function of ATEFlap in HAWC2

4.4.1 General function

The main algorithm of ATEFlap is integrated in HAWC2 as one of the options to estimate the dynamic stall. The model is automatically carried out once it has been declared in "htc" file.

As discussed in Section 4.2.3, the external pre-processor is able to provide a look-up table for a given (α, β) pair. However, the basis are α_{eff} and β_{eff} instead of the real ones. Even for a certain $(\alpha_{eff}, \beta_{eff})$ pair, the corresponding C_l^{st} is not fixed, because of the varying f^{dyn} . In a word, ATEFlap returns a C_l after combining all the issues listed above.

4.4.2 Including the flap deflection

A test case is carried out to show how the flap affects C_l . A predefined flap variation is written in the control file. As shown in Figure 4.6, fluctuations are observed at time points 10s and 11s due to the sudden change of flap angle, respectively. This is exactly what it has been specified. The positive flap is defined as pointing towards the pressure side, thus returning a general increasing trend.

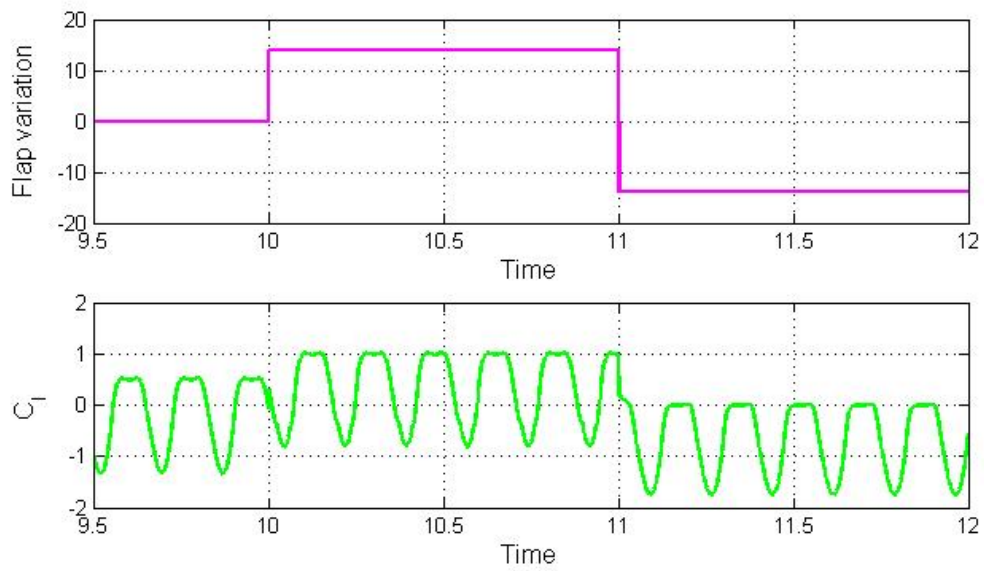


Figure 4.6: The effect from ATEFlap

Load-form study

A flap generates substantial change in the lift coefficient by altering the pressure distribution along the chord[3]. So does the pressure along the blade path. Again, the local ideal power coefficient is defined here for further explanation,

$$C_{p,ideal} = v_{r,i}Q_{n,i} \quad (5.1)$$

where the local normal pressure jump $Q_{n,i}$ has to be normalized. Obviously, the load or $Q_{n,i}$ distribution is directly associated with final power output. At the same time, the pressure field is caused by the blade forces. Hence, $Q_{n,i}$ is the bridge connecting the blade force and the power output. It is then considered as the key factor to playing with if one wish to increase the power by flap.

It is easier to conduct the flap angle optimization after a specific goal in a form of the load distribution that leads to the optimal power has been determined. The prerequisite research has provided an inspiration on adjusting the load for an uncertain 2D VAWT cross section (Section 5.1), which is so-called load-form study.

Load-form study is rotor-dependent. Given a rotor geometry (Section 5.2), Section 5.3 illustrates the basic process of a new load-form study, mainly focuses on determining the variables that actually affect the curve.

Subsequently, the results are shown in Section 5.4. Combining the outcomes of Chapter 4, the control strategies as a form of $\beta(\theta)$ for different TSRs are presented in Section 5.5.

5.1 The power gain optimization: A recap on the previous research

As mentioned in Chapter 2, the induction distributes unequally along a VAWT section, thus there is no way to represent it by an actuator in a single stream tube. However, the reason that an actuator disc is capable to represent a HAWT is that ideally the loads are adjusted to be even on the wholly swept area through the designed twist angle, which makes the actual angle of attack be consistent along the blade.

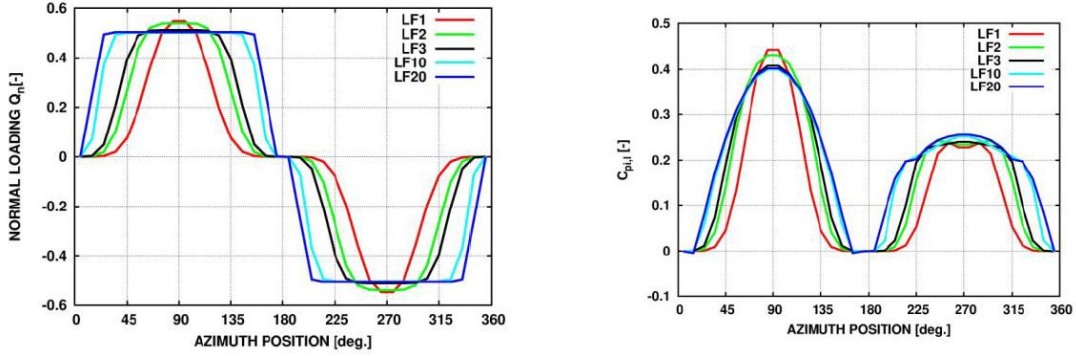


Figure 5.1: The loadforms(left) and their induced C_p distribution(right)[1]

It is already known that under the condition of uniform inflow, the Betz limit ($C_{p,max} = 0.593$) indicates the maximum power capture. Unfortunately, the solution for irregular inflow is still unclear. Evidently, **converting an inexperienced case into another where the way to optimize is already known** is evidently a wise choice. This is the core idea behind the whole study.

Assuming that $Q_t = 0$ is constantly valid, an expression of Q_n is then introduced in [1] to adjust the local Q_n to be more uniform,

$$Q_n(\theta) = Q_{n,max} \frac{\sin(\theta)}{|\sin(\theta)|} \left(1 - |\cos(\theta)|^m + \frac{1}{2\pi} \sin(2\pi |\cos(\theta)|^m) \right) \quad (5.2)$$

where m is an integer parameter, defining the degree of the squaring of the curve.

As presented in Figure 5.1, five cases with $m=1,2,3,10$ and 20 are selected for creating the Q_n curve [1]. Under the AC process, knowing the load distribution is enough to obtain C_p for a given rotor, the local power is yielded without any iteration.

As shown in Figure 5.1, a squared load-form actually leads to an unequal C_p distribution. One may increase the power by equalizing the local power coefficients on up- and downwind sides. Such an asymmetrical load-form was performed by Madsen et al.[1]. The load-form curve was therefore vertically offset with a constant. It turned out that although local value changes, the integral C_p remains the same. As a result, offsetting the curve is out of our consideration for the further steps.

5.2 Modeled rotor

5.2.1 The factors

It is notable that the optimized load-form is universal, independent from the rotor geometry and operational conditions. Their affects will not appear before the blade forcing and induction calculation.

[4] indicates that a blade number of two or three is equally a good choice with respect to the rotor loads. According to Figure 5.2, more blades of the same σ will lead to a smoother thrust distribution, and finally increase the overall C_T .

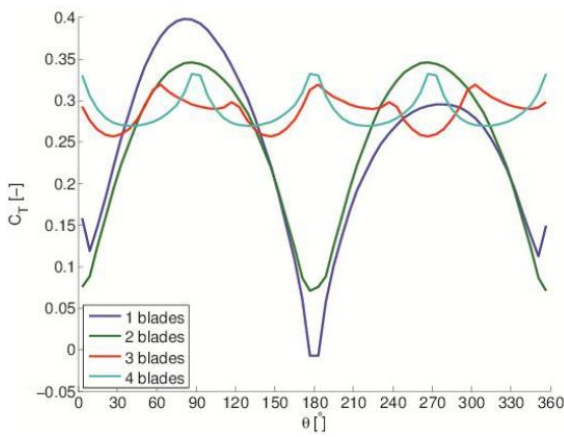


Figure 5.2: The local C_T distribution w.r.t. the blade number[4]

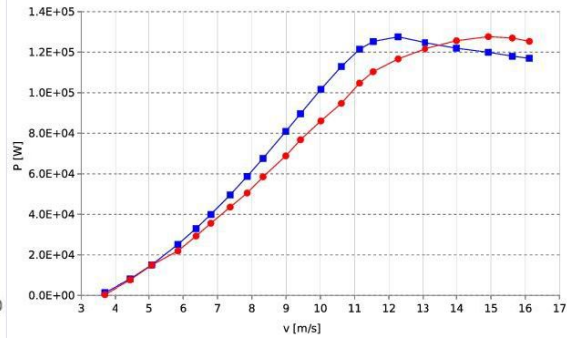


Figure 5.3: Power performance for Magdalen Island VAWT at 29.4rpm[4]

Furthermore, the wind speed and radius will not affect the inductions because all the parameters are normalized before being introduced as mentioned in Chapter 3. Hence any of a wind speed corresponding to the optimal working condition is fine (See Figure 5.3).

As mentioned, dynamic stall is dominant in low TSRs, but AC as a time-averaged model does not count dynamic stall. Hence the variation discussed here is only partly true. Recall Figure 3.5, the induction raises with TSR, as well as the blade loads. We thus anticipate flap impacts would be more notable with higher TSRs.

Bedon et al.[4] set up a Darrieus rotor with solidity $\sigma = 0.165$ for experiments. Recall the blade force formula,

$$L(\theta) = \frac{1}{2} \rho v_{\infty}^2 c C_l(\alpha) \quad (5.3)$$

The formula above implies that the shorter the chord length is, the less impact from the blade to the flow field. Hence, a reasonable σ is a good choice on the guiding significance.

5.2.2 The set-up

Table 5.1 illustrates the model constructed for modeling. The applied airfoil parameters has been presented in Table 4.1 along with ATEFlap implementation.

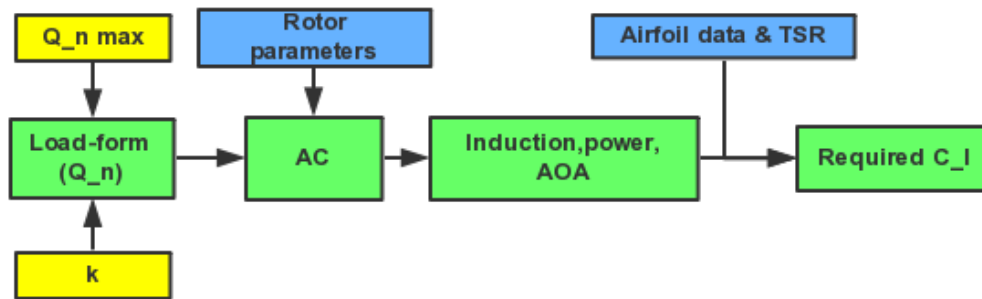
5.3 Load-form study process

A brief load-form study process is presented in Figure 5.8. As an improvements, MOD-LIN AC model is adopted for the following instead of the old linear model applied in [1] when MOD-LIN was not proposed at that time.

Similar as the previous, the load-form is constructed firstly. A straightforward “try-out” procedure is carried out to look for the combination of Q_n and k that leads to the optimal

Table 5.1: Implementation parameters

External condition	Wind speed v_∞	9m/s
	Density ρ	1.225 kg/m^3
Rotor Geometry	Blade chord c	0.1
	Number of blades B	2
	solidity σ	$\frac{Bc}{R} = 0.2$
	Rotor height H	2m
	Rotor Radium R	1
	Rotor type	Straight H
TSR		2,3,4,5

**Figure 5.4:** The process of load-form study

power. Recall the flow-chart of the AC code presented in Figure 3.3. In this study, the variables are introduced in the half-way of AC routine and thus no iteration is needed now.

It should also be emphasized that the study is only for a specific rotor with a certain set of operation conditions, even though the rotor diameter is normalized into 1. Not only the variable TSR, but also the solidity and probably other factors affect the final flap variation. For more information, please refer to Section 5.2.1.

The aim of load-form study is looking for the required $\beta(\theta)$, which can be calculated easily after the required blade force at the evaluation points for a certain rotor is known.

5.3.1 The variables

There are two parameters involved in the process, namely the normal load amplitude $Q_{n,max}$ and the shrink angle k .

Q_n is the key factor associated with the power gain, this argument can be supported by Eq (3.8) and (3.10). However, AC is a two stage power conversion actuator, as the flow passes through the volume surface twice, creating a twin-peak power production curve as seen in Figure 5.1. A too large induction in upwind side will lead to a weak production in downstream part. This is a trad-off decision.

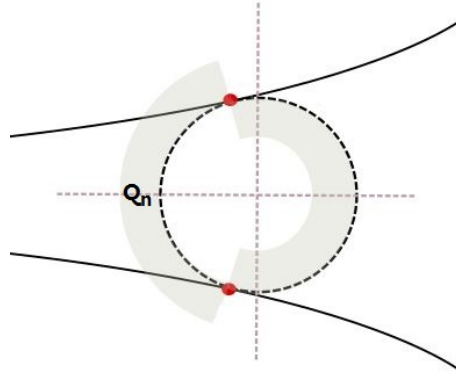


Figure 5.5: The ideal flow field and load distribution for a VAWT section

As illustrated in Figure 5.5, the stream tube expands even before arriving at the actuator, so the tangent points are at neither 0° nor 180° . If one performs the previous version of load-form study, a region with negative $Q_{n,i}$ would appear on both sides because of the sign of $v_{r,i}$. The negative regions deduct the final value of integrated C_p . This is why the shrink angle is taken into account.

5.3.2 Upwind side shrinking

The ideal of transforming the load-form curve for a certain shrink angle k is presented in Figure 5.6. One should notice that it is the Q_n curved "moved" horizontally along the x-axis, rather than playing with azimuth angle directly.

The curve is divided into four parts based on the azimuth positions (0° 90° , 90° 180° , 180° 270° , 270° 360° , illustrated Figure 3.1). Those two in upwind half tend to merge towards the 90° position while the other two move apart from 270° . An assumption that the resolution of k is the same as the one of azimuth angle is applied here so that the moving (counted as the number of elements in Q_n array) then becomes exactly equal to the shrink angle (Degree form). However, as a result of the movements, part of the original curve vanishes and a gap around 270° appears. Based on the ideal of the study, which is to optimize the gap is filled in with the negative amplitudes.

5.3.3 The faults

Unfortunately, the study on the case $m=1,2$ and 3 all tend to be defected due to the excessive shrink. In the considering interval, after k is beyond a certain number, an obtrusive "peak" would appear at 90° with a value lower than $Q_{n,max}$. At the same time, the end of down-wind side, a "flap groove with $-Q_{n,max}$ is being created (See Figure 5.7). So this kind of curve implies abandoning to harvest power on upwind side but capture more on the down stream. It is not too physical an ideal to be considered.

Therefore, a proper shrink angle upper limits for those cases. It should be noted that

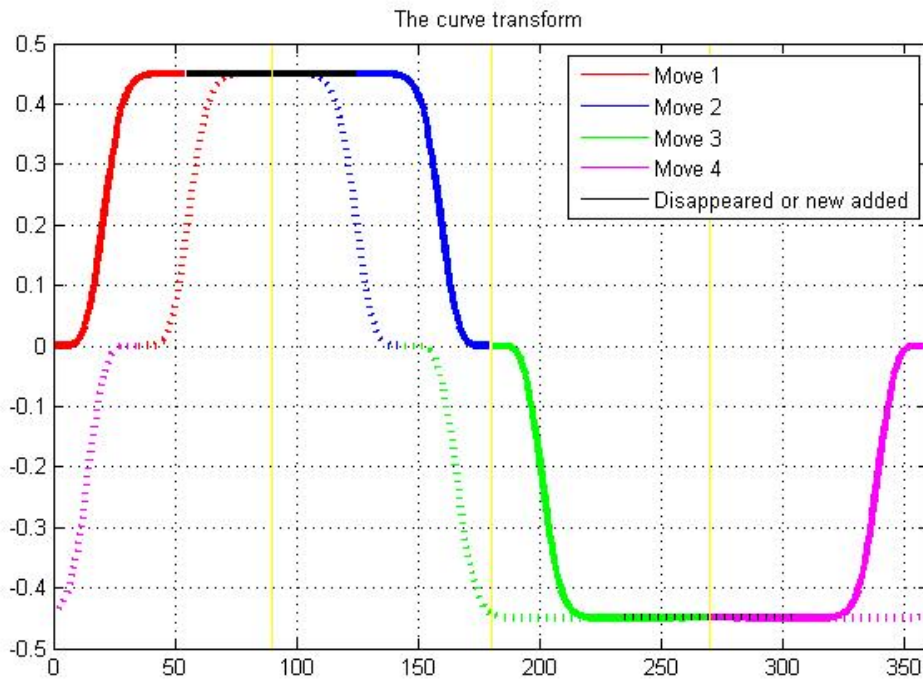


Figure 5.6: The illustration on the curve transforming

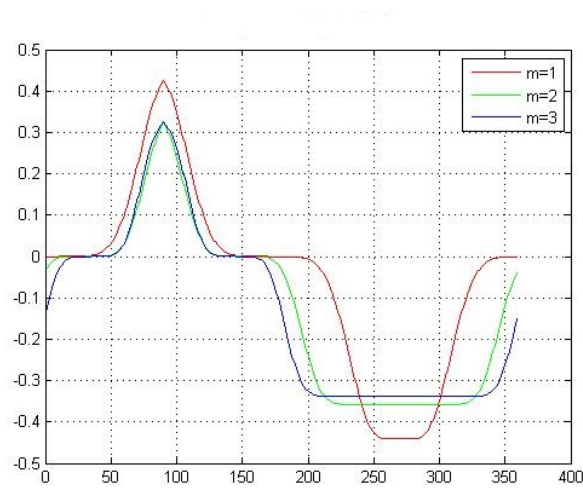


Figure 5.7: The fault of load-form

our interests in this phase are mostly on the two most flat ones ($m=10$ and 20) which obviously yield more power. The previous three are simply the back-up plans in case of the superior is proved to be unrealistic.

5.3.4 The blade force

The procedure to calculate the blade force is actually similar to Chapter 3 but in an inverse order (recalling Eq (3.7), (3.6) and (3.7)). It is worth mentioning that as the final step, the required lift coefficient is calculated as,

$$C_{l,need} = \frac{(C_{n,need} - C_d \sin(\alpha))}{\cos(\alpha)} \quad (5.4)$$

where C_d is from airfoil data. This is the step where the airfoil data is taken into account. An assumption of the independence of drag from flap angle is applied here to simplify the problem.

5.4 General result for load-form study

The results are summarized in Figure 5.8 and Table 5.2.

Generally, the more uniform the curve is, the higher $C_{p,ideal}$ is achieved.

Table 5.2: The result of Load-form study

m	1	2	3	10	20
k	5*	8*	16*	12	8
Q_{max}	0.381	0.302	0.286	0.242	0.232
$C_{p,ideal}$	0.4573	0.5234	0.5543	0.5796	0.5859
* All reach the maximum limits.					

However, the study for $m=1,2$ and 3 are all defected as predicted, unlike the latter two cases returning a more realistic and better power-effective results. It is worth noting that the steps are observed in both of the remaining curves, so the sudden change of flap is unavoidable one way or another. Given all that, the load-form with $m=20$ is processed for further steps from this section.

5.5 The flap control strategy

Since AOA and the required C_L are known, β is then evidently obtained from the 3-D surface. However, some compromises are necessary because required C_L sometimes are not possible.

Figure 5.9 to 5.12 demonstrate the resultant AOA, C_l and final flap angle distribution

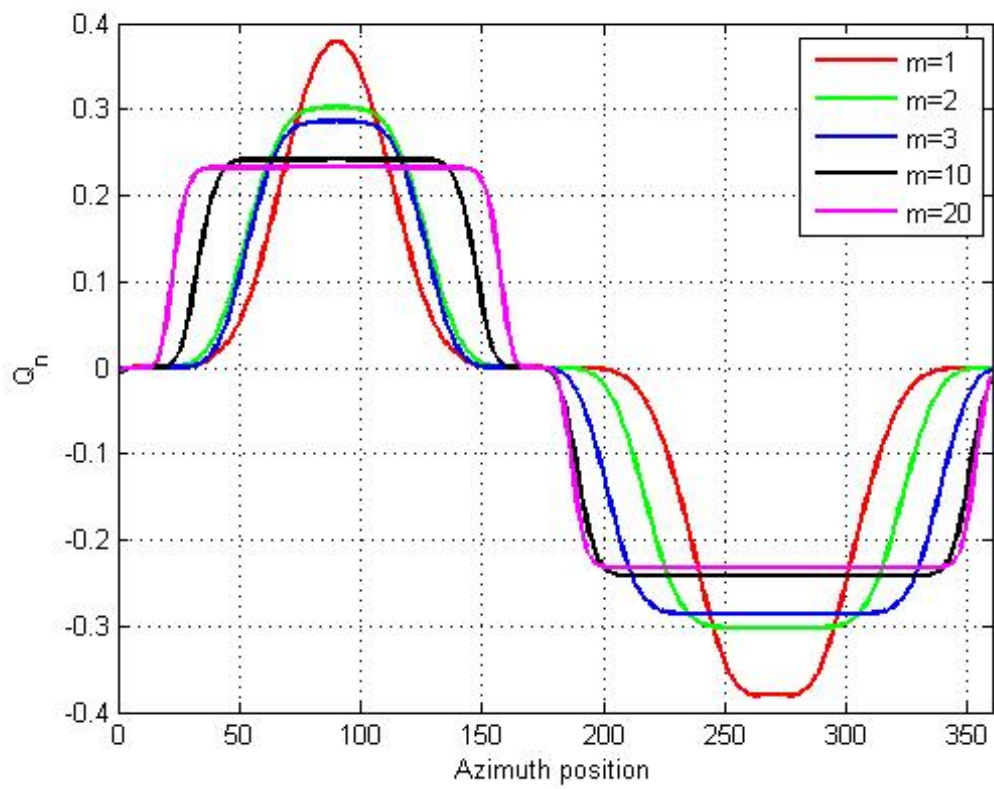


Figure 5.8: The optimized load-form

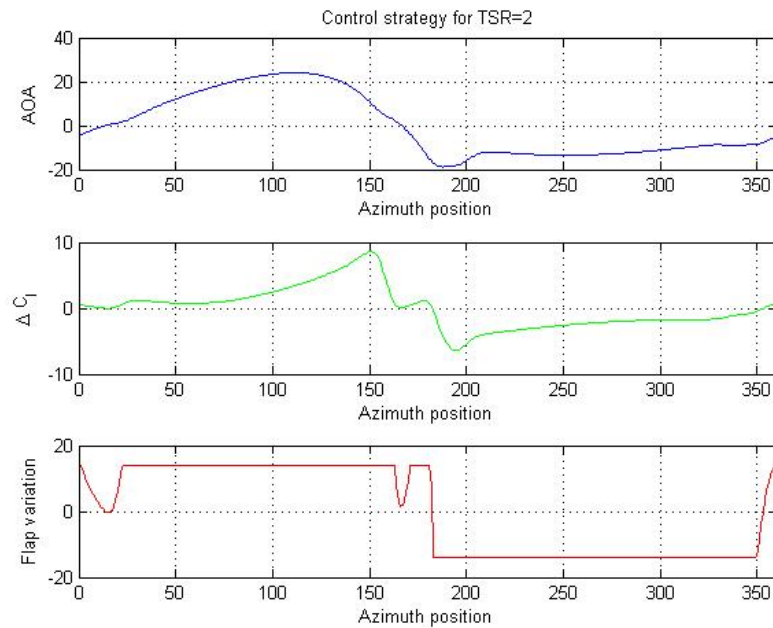


Figure 5.9: Flap variation for TSR=2

for different TSRs. AOA generally decreases with an increasing TSR and the induced induction, hence the flap variation are totally different. Some flat region is observed in the flap variation curves, because of the limitation on the flap motion. However, flap solution seems to be not as efficient as expected in low TSRs, the curve mostly remains along on the limits. This implies that the flaps are better installed at wide sections of Darrieus rotor for more remarkable impacts.

It is worth emphasizing that no compromise about the swift variation were made. The swing interval $[-14^\circ \ 14^\circ]$ is considered to be narrow enough.

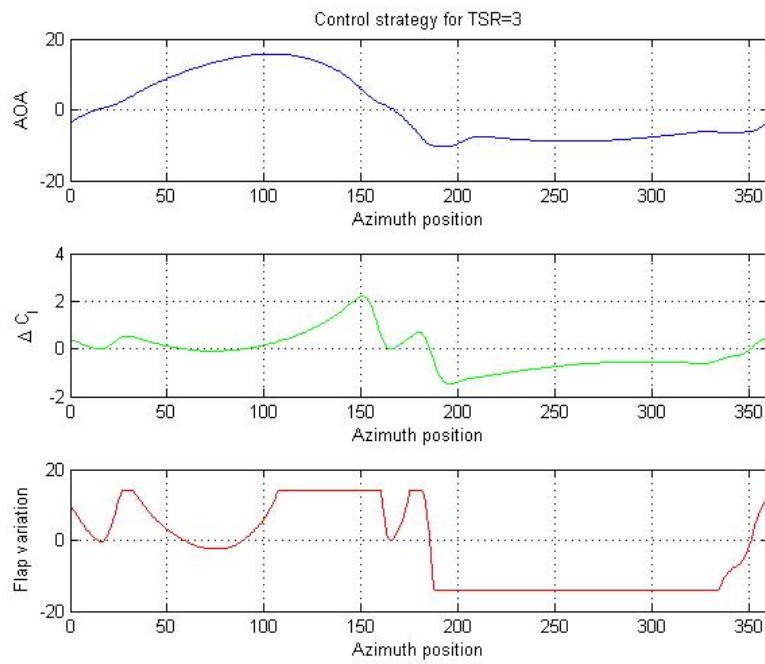


Figure 5.10: Flap variation for TSR=3

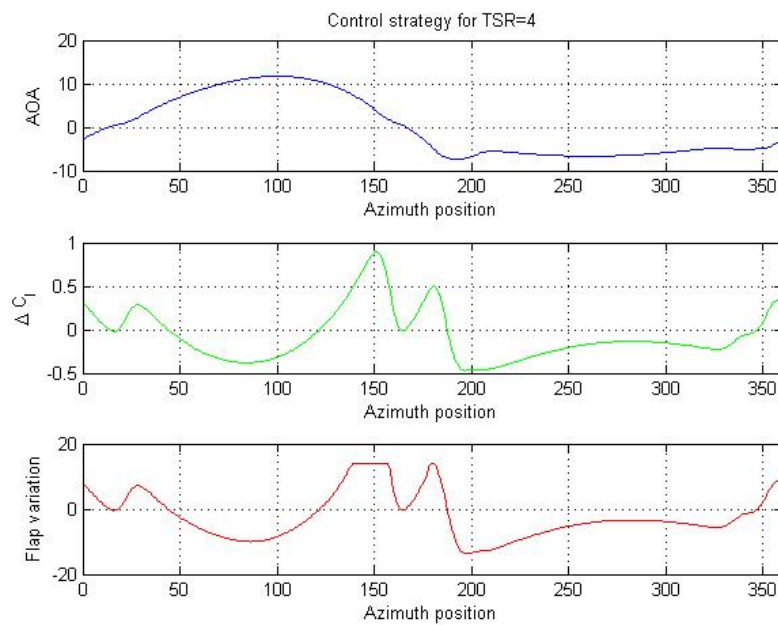


Figure 5.11: Flap variation for TSR=4

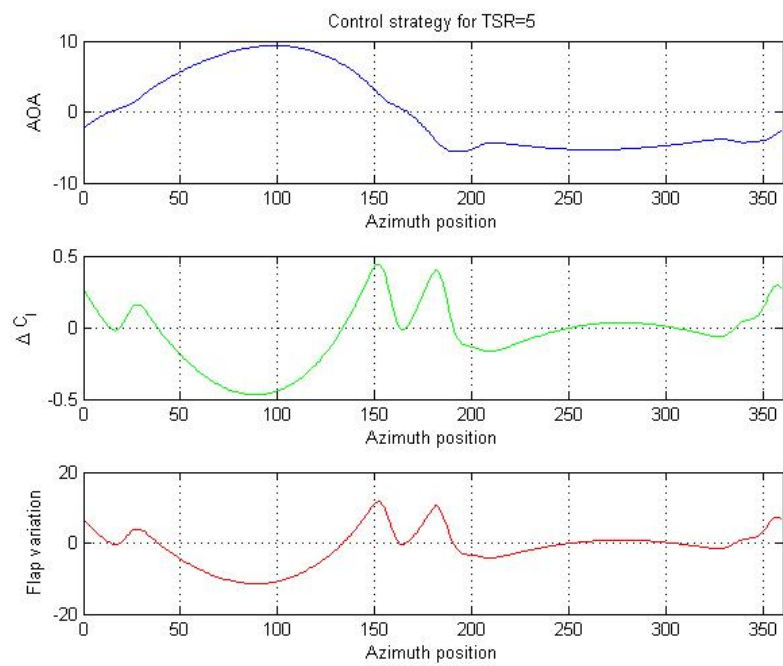


Figure 5.12: Flap variation for TSR=5

The strategy validation

After the flap strategy is drafted in a quasi-steady case, it is time to validate them in a dynamic simulation. However, constructing a dynamic working environment and operation condition is overwhelmed for the self-developed Matlab routine. The existing numerical tool, HAWC2 is then employed for the task. The HAWC2 program structure and modeling ideas are illustrated in Section 6.1, while Section 6.2 focuses on the specific model we have adapted. In the end, Section 6.3 presents the simulation process along with the final results in Section 6.4 answering to our ultimate research question raised in Chapter 1.

6.1 An introduction to HAWC2

HAWC2(Horizontal Axis Wind turbine simulation Code 2nd generation) is an aero-elasticity code developed by DTU-Risoe and intended for computing the turbine response in time domain[32]. Recently, because of the R&D needs, VAWT model and eigen-frequency analysis have been introduced into the code.

6.1.1 A wind turbine model in HAWC2

As shown in Figure 6.3, the structure in HAWC2 is based on a multi-body formulation. A simplified "point-line" model is defined to represent the turbine in HAWC2, where those flexible "line bodies" are formed with several un-deformable Timoshenko beams with pre-defined mechanical characteristic (e.g. mass stiffness and inertia distribution). The connections among the "lines" are actually the constraints with specified degree of freedom. The components of a typical wind turbine model is illustrated in Figure 6.3. After the structure geometry has been set up, the parameters that determines its responses for different external conditions (wind and wave) are defined in the data file. All these aspects, and the mutual influence between aerodynamic force and structure deformation

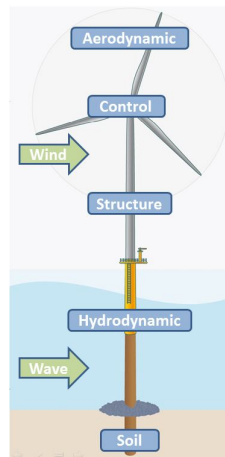


Figure 6.1: A wind turbine model in HAWC2

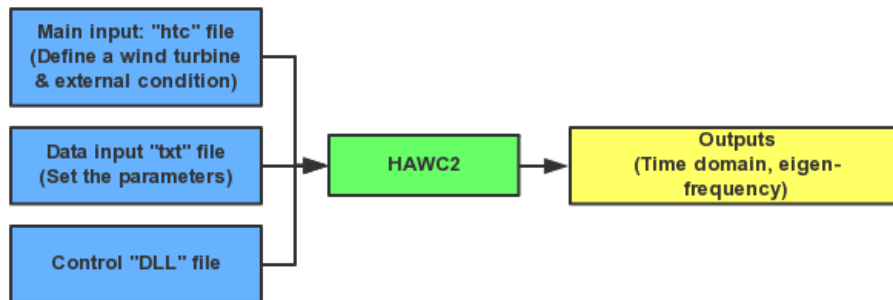


Figure 6.2: HAWC2 program structure[31]

lead to a complex iteration process. Thus the outcomes present a dynamic behavior.

6.1.2 HAWC2 program structure

Linking to the turbine model presented in Figure 6.3, an overview of HAWC2 program is shown in Figure 6.2.

A main input "htc" file sets up the components (bodies) of a wind turbine. Starting from the ground (global coordinates), the bodies are defined along with its orientation and the outer dimensions. By transforming the local coordinate systems and setting up the constraints, a whole turbine is clearly presented. At the same time, the external conditions are also specified here.

In order to define the mechanical characteristics of the structure, the required parameters are written in the "txt" assigned files. Declared in the "htc" file, the input files are linked with the corresponding structure. In our case, moreover, a special folder containing the outputs from ATEFlap pre-processor is needed as a supplement.

HAWC2 core does not contain the information about the specific parameters but the

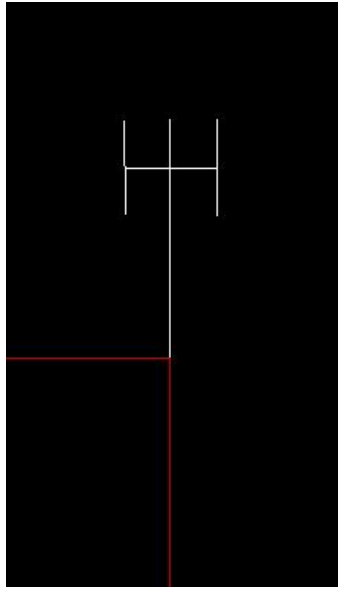


Figure 6.3: The 3D H-rotor model in HAWC2

algorithm dealing with the inputs. The controller "DLL" files determine how the wind turbine would response for multiple particular circumstances. It is mainly adopted to control the operational parameters such as the turbine speed, pitch, and particularly, the flap deflection[17].

DLL itself is naturally a subroutine that allocates the inputs into HAWC2 core based on agreed index. Here, the DLL acts as a bridge function between HAWC2 main routine and an input file containing the control strategy.

6.2 HAWC2 model set-up

6.2.1 H-rotor

For a Darrieus rotor like Deepwind concept, the whole rotor would experience different TSRs for a certain rotational speed due to the radius difference, which is a rather complex situation. That is why only a 2D section has been studied from the first place. Unfortunately, the modeling concept of HAWC2 dictates its inability to model a 2D section. As a compromise, an H-rotor is set up instead of a 3-D Darrieus. The geometry has been presented in Table 6.1 and 4.1.

The aerodynamic effects from the support beams connected to the blades are neglected, and thanks to the homogeneous behavior along the H rotor (without the tip loss), the 3D model is thus considered to be capable to represent a 2D section.

6.2.2 Flap variation specification

In the given program, the index is appointed to time, while the results of load-form study is azimuth-dependent. Since the initial position of each blade, the rotational speed and the simulating time are all known, it is possible to convert $\beta(\theta)$ into $\beta(t)$, then import it to the data file. That is how the flap variation is specified for the simulations.

An external "dat" file containing the expected flap angles at different time points is adopted as the input for the flap control.

In addition, it is actually possible to assign the azimuth position as the common index using the original "DLL". In that case, only the azimuth of one blade can be employed, the flap angle of the other blade needs to be adapted.

6.3 The simulation process

6.3.1 The limitations of the flap modeling in HAWC2 for VAWTs

As discussed, the dynamic stall model ATEFlap applies its impacts through correcting the lift coefficient C_l . However, it was clarified by correspondence with the HAWC2 developers that the load changes from flap actuation is not taken into account in the induction modeling. The reason for this limitation is that HAWC2 is initially designed for a HAWT, where flap variation and dynamic stall does not cause a significant difference on overall situation. Thus their effects were not accounted. This seriously drags the whole process. An alternative way, namely the really conducted process was slightly different. The returning $F_n(\theta)$ from a HAWC2 simulation based on the flap variation presented in Section 5.5 is once again applied as input into the self-developed AC routine for further steps.

6.3.2 The initial test

Among all the four cases presented from Figure 5.9 to 5.12, the case with TSR=4 in Figure 5.11 is considered to be the most well researched one, because the flap is able to adjust the load to meet the targets while it sometimes meets the limits but not saturate in a too large region.

Therefore, only that case is taken for further considerations.

As mentioned, a gap between the quasi-steady and the semi-dynamic was expected. As an initial test, the flap variation demonstrated in Figure 5.11 is directly introduced into HAWC2 model to see how dynamic stall model affects the rotor behavior.

As can be seen in Figure 6.6, a deviation of the loading appears mainly on downwind side where AOA is negative. Dynamic stall lowers both the power output and thrust from a macro perspective. Its impacts are mainly dominant on the downwind side. All in all, the quasi-steady flap guidance defects in dynamic stall model joined environment, particularly on the downwind side.

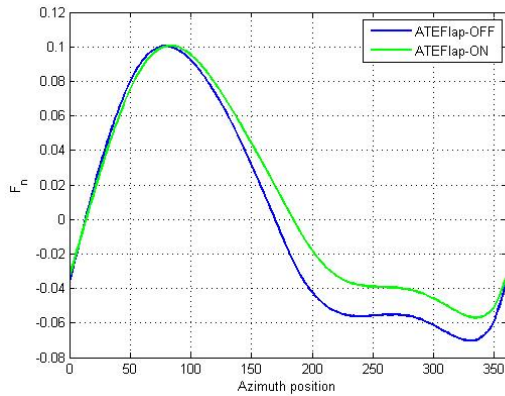


Figure 6.4: F_n v.s. θ with or without dynamic stall model on

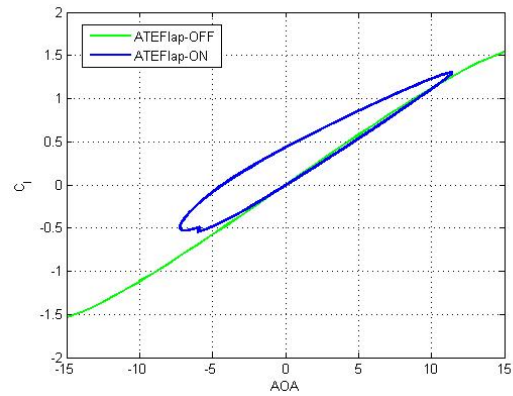


Figure 6.5: C_l v.s. AOA with or without dynamic stall model on

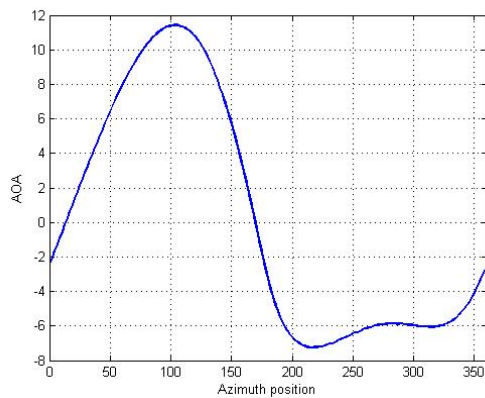


Figure 6.6: AOA distribution with dynamic stall model on

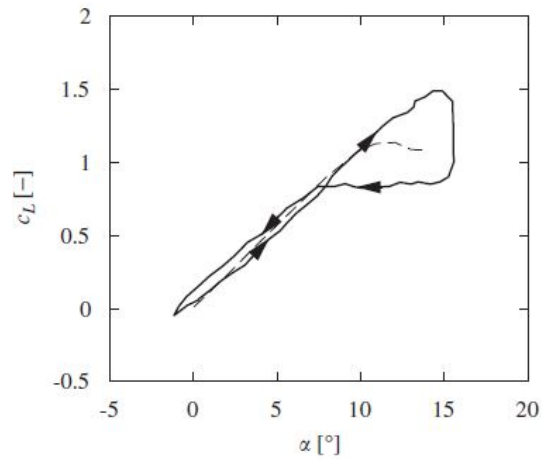


Figure 6.7: C_l v.s. AOA under static (Dashed) and dynamic (Solid) stall situation[15]

6.3.3 The effects from the dynamic stall model

The dynamic stall is not expected to be dominant for TSR=4 case. It is more likely to have some other factors that limited the performance.

In order to figure out the reason of the deviation found in the initial test, two special investigation on blade forces are carried out and finally displayed in Figure 6.4 and 6.4. To eliminate the flap variation impacts, the flap is set to be silent for both cases.

The slight inflation is found before the blades jump into wake interaction area. However, the model does nothing but reduce the blade forces in the downwind side. The displayed circular pattern in Figure 6.4 is very similar to the dynamic stall. However, it is more likely the hysteresis phenomenon occurs. It has been included in ATEflap.

Recall Figure 2.5 in Chapter 2, which Carlos[40] shows that there is a rapid change of bound vortex roughly at both the windward and leeward. In particular, the later one

is more rapid. Thus, a larger amount of shed vorticity is expected. This is also a rapid changing region of the AOA, as confirmed by Figure ???. Under non-stationary conditions, it takes some time for the flow to approach the stationary flow pattern[15]. The stall occurs at around 90° position, where AOA exceeds 10° (See Figure 4.2). Larsen et.al.[15] indicates that once the flow is separated during the motion, the degree of attachment will also exhibit delay with respect to its stationary value. This will not be recovered even in the linear range, as shown in Figure ??. This confirms the behavior of the blade force in Figure 6.4, where a lag behind static value is observed after turning on the ATEFlap in HAWC2.

6.3.4 The modification

Even though the quasi-steady load-form has been proven to be insufficient, it is rather complex to include dynamic stall in the self-developed code. Based on the situation described in Figure 6.4, an alternative improvement of imposing an empirical modification on the region with negative AOA is a proposed.

Recall Figure 5.11, increasing the flap variation is actually possible since the space for improvements exists.

A factor of 1.5 is simply introduced to be multiplied with the flap angles in downwind part to increase the blade loads. This is denoted as Case 3 in Table 6.1. It is hard to figure out an reasonable modification factor since the deviation changes with azimuth position, and no pattern is found.

6.4 The validation result

Table 6.1: Final simulation result

Case No.	1	2	3	Target
Flap	OFF	ON	ON,modified	-
C_T	0.7384	0.7921	0.8318	0.9097
$C_{p,ideal}$	0.5464	0.5707	0.5793	0.5859

The final outcomes from the simulations are summarized in Table 6.1, Figure 6.6 to 6.8. The slight deviations of Q_n observed in upwind side are mainly caused by the hysteresis, the two occurred positions match those observed in Figure 6.4.

Recall the flap variation displayed in Figure 5.11, the flap meets its limitation at around 150° and 170° . In other words, the target cannot be achieved. However, Q_n at those two points exceed the targets. This is also caused by the hysteresis.

The hysteresis phenomenon evidently reduces the overall blade loading, shrinks the power output. Its impacts are mainly dominant on the downwind side. Applying the gain factor did successfully increases the rotor performance as desired. Even though the thrust raises more at the same time, the target is still not achieved.

An exception is found by comparing case 1 and 2. Roughly 0.025 increasing of C_p is

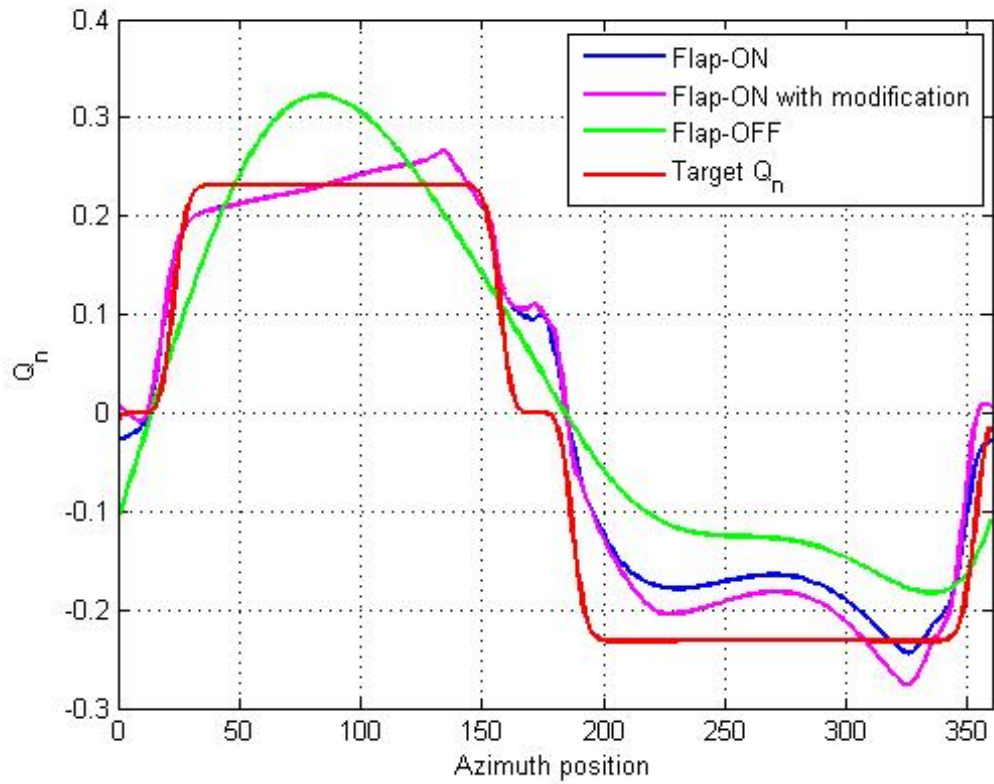


Figure 6.8: Final result: Q_n distribution

exchanged with only doubled increasing of C_T . This is caused by the shrinking capture in the upwind side, where flap sometimes reduces the inductions on purpose so as to leave the energy to downwind part.

It is notable that a slightly decreasing induction in upwind side is observed in Figure 6.8. This reveals the modification is an issue that gave rise to the whole revolutions.

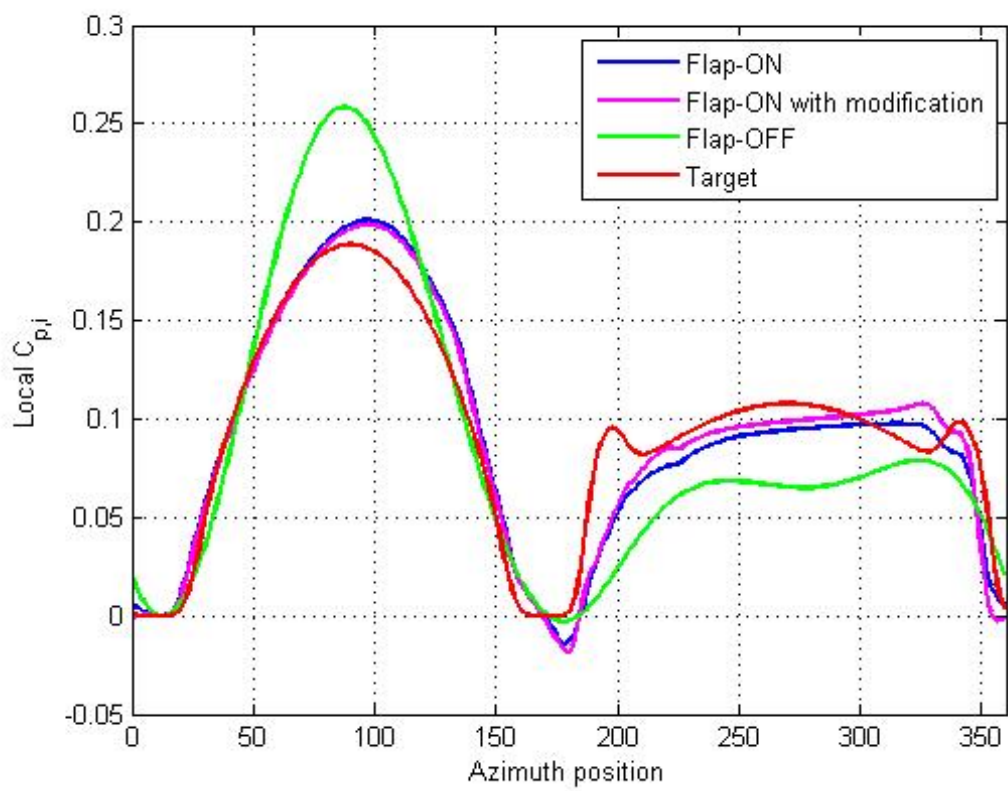


Figure 6.9: Final result: Local $C_{p,i}$ distribution

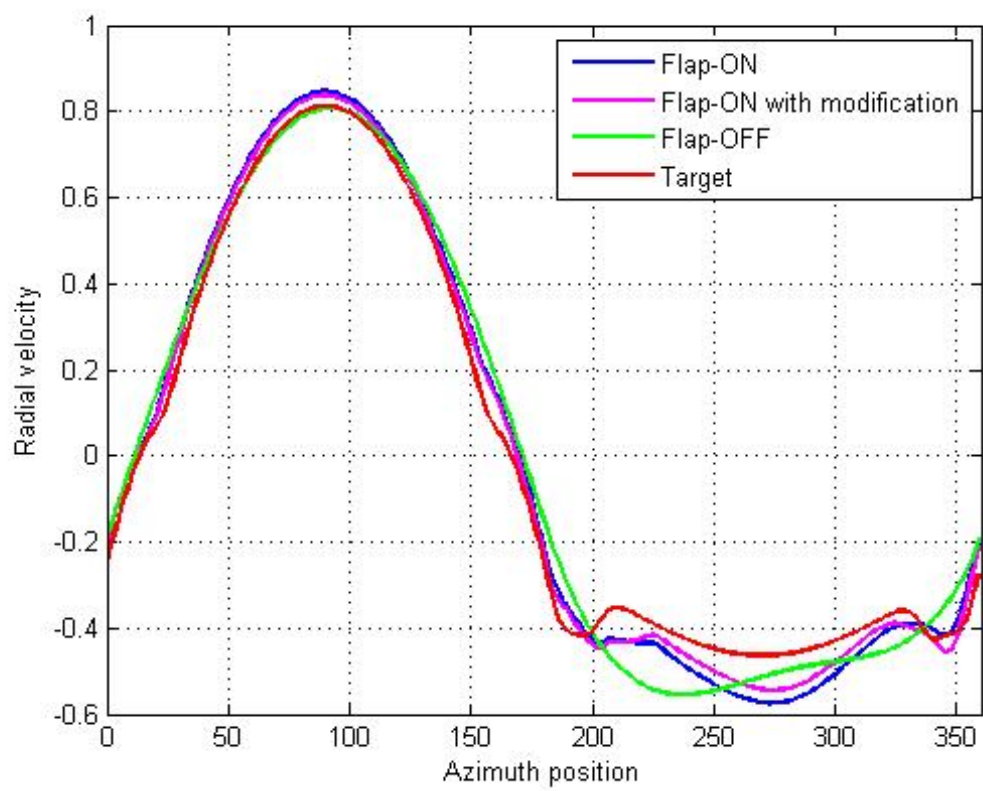


Figure 6.10: The radial velocity distribution

Conclusion and recommendation

As conclusion, Section 7.1 summarizes the important findings through the whole process. On the top of that, 7.2 presents recommendations for further analysis and prospective topics.

7.1 Conclusions

The prerequisite research presented in [10] compared the performances of different aerodynamic models for a VAWT. The comparison can be completed by adding CFD model and measurement data as the benchmark.

Several issues are raised for modeling a VAWT on the aerodynamic perspective. The varying AOA in a revolution finally leads to the nonequivalent loads distribution and the dominance of dynamic stall; The lateral inductions present an equally effective impact on the loading, unlike the one for HAWTs is usually neglectable; The wake interactions and dynamic stall phenomenon both limits the performance in downwind part.

In HAWC2, the dynamic load changes from flap motion do not influence the induction computation. However, for the present application on VAWTs, this limits the implementation as the research target is changing the overall load distribution on the rotor surface with the flaps. Slight disagreements with our self-developed AC code was found, especially in the downwind part. This might caused by other internal sub-routine.

Even though there is only one rotor is implemented, it is considered representative enough to claim the ability of flap to regulate the load distribution. However, it only works on the high TSRs because of the dominance of dynamic stall, and the too high AOA in upwind side in low TSRs. This implies the possible flap installation position are only on the wide sections of a Darrieus Rotor.

Flap is proven to be able to provide a significant power increasing. The achievement is made by transferring the local amount of power capture to another position, assisted with increasing the inductions in some position. Table 6.1 has demonstrated a wide range of variation for both C_p and C_T . This implies that flap is also capable to reduce the rotor load with a little deficit of C_p .

However, it is worth emphasized here the flap variation is azimuth-dependent. The azimuth position is defined according to the wind direction. This unfortunately means a VAWT with flaps becomes sensitive to orientations, crippling one of its advantages than a HAWT. At least a wind direction sensor is then mandatory.

7.2 Recommendations

1. Applying the following improvements in HAWC2. It is recommended that increase the resolution of integrated AC model from 10° to 1° . Moreover, it is recommended to modify the flap implementation so that the load changes from a steady state flap actuation are taken into account in the induction computations.
 2. The similar load-form study should be repeated in HAWC2 to include dynamic stall and the hysteresis after the suggested improvements are made.
 3. Conducting flap into VAWTs for other purpose. Only increasing the power gain was investigated, but it is also potentially feasible on reducing the loads while maintaining the same C_p , adjusting C_p to regulate the power, and achieving aerodynamic brake in a VAWT.
 4. Limiting the aerodynamic performance of the rotor geometry for installing the flap is inevitable, let alone the structural issues. The geometry cannot be aerodynamically or structurally optimal. Hence, it is a mandatory step to compare the aerodynamic performance between the optimized Darrieus and adapted one for flaps.
 5. Applying machine learning for flap control. In dynamic stall such a complex and unclear circumstance, leaving the job to machine itself probably better than entirely relying on the man-caused inputs.
- [29] reported the success of Siemens on applying machine learning in wind farm operation. By collaborating the existing data to determine the wind field, a "try-out" scheme is automatically performed to allocate the induction of each turbine in a tandem array. The best option would be directly adopted next time when the same wind condition is detected. As a result, an overall power output increasing is achieved. The same idea is considered to be feasible in flap control. To optimize the flap variation, such a complex process with machine learning if there is truly a commercial proposal on flap equipped VAWT in the future.

References

- [1] Helge Aagaard Madsen, Uwe Schmidt Paulsen, and Luca Vita. Analysis of vawt aerodynamics and design using the actuator cylinder flow model. *Proceedings of Torque 2012, the Science of Making Torque From Wind*, 2012.
- [2] Jr. Anderson, John D. Fundamentals of aerodynamics. 2011.
- [3] Thanasis K Barlas and GAM Van Kuik. Review of state of the art in smart rotor control research for wind turbines. *Progress in Aerospace Sciences*, 46(1):1–27, 2010.
- [4] Gabriele Bedon, Uwe Schmidt Paulsen, Helge Aagaard Madsen, Federico Belloni, Marco Raciti Castelli, and Ernesto Benini. Aerodynamic benchmarking of the deep-wind design.
- [5] Leonardo Bergami and Mac Gaunaa. *ATEFlap Aerodynamic Model, a dynamic stall model including the effects of trailing edge flap deflection*. Denmark. Forskningscenter Risoe. Risoe-R. Danmarks Tekniske Universitet, Ris Nationallaboratoriet for Bredygtig Energi, 2012.
- [6] Habtamu Beri, Yingxue Yao, et al. Double multiple streamtube model and numerical analysis of vertical axis wind turbine. *Energy and Power Engineering*, 3(03):262, 2011.
- [7] Z ect. Bloomfield, H.J.; Allcock. *MEFEPO North Sea Atlas*. Liverpool : University of Liverpool, 2011.
- [8] Okeoghene Eboibi. The influence of blade chord on the aerodynamics and performance of vertical axis wind turbines. 2013.
- [9] Sandra Eriksson, Hans Bernhoff, and Mats Leijon. Evaluation of different turbine concepts for wind power. *Renewable and Sustainable Energy Reviews*, 12(5):1419–1434, 2008.
- [10] C Simao Ferreira, H Aagaard Madsen, M Barone, B. Roscher, P. Deglaire, and I Arduin. Comparison of aerodynamic models for vertical axis wind turbine. *Energy conversion, IEEE transactions on*, 21(3):725–733, 2006.

-
- [11] Mac Gaunaa. Unsteady two-dimensional potential-flow model for thin variable geometry airfoils. *Wind Energy*, 13(2-3):167–192, 2010.
- [12] Martin OL Hansen. *Aerodynamics of wind turbines*. Routledge, 2013.
- [13] Morten Hartvig Hansen, Mac Gaunaa, and Helge Aagaard Madsen. *A Beddoes-Leishman type dynamic stall model in state-space and indicial formulations*. 2004.
- [14] Joseph Katz and Allen Plotkin. *Low-speed aerodynamics*, volume 13. Cambridge University Press, 2001.
- [15] Jesper Winther Larsen, Søren RK Nielsen, and Steen Krenk. Dynamic stall model for wind turbine airfoils. *Journal of Fluids and Structures*, 23(7):959–982, 2007.
- [16] Torben J. Larsen and Helge Aagaard Madsen. On the way to reliable aeroelastic load simulation on vawt’s. *Proceedings of Ewea 2013*, 2013.
- [17] Torben J Larsen and Anders Melchior Hansen. *How 2 HAWC2, the user’s manual*. Risø National Laboratory, 2007.
- [18] J Gordon Leishman. *Principles of Helicopter Aerodynamics with CD Extra*. Cambridge university press, 2006.
- [19] Allan MacAskill and Paul Mitchell. Offshore wind an overview. *Wiley Interdisciplinary Reviews: Energy and Environment*, 2(4):374–383, 2013.
- [20] H. Aa Madsen. *The actuator cylinder a flow model for vertical axis wind turbine*. PhD thesis, Aalborg university, 1982.
- [21] H. Aa Madsen, T. J. Larsen, U. S. Paulsen, and L. Vita. Implementation of the actuator cylinder flow model in the hawc2 code for aeroelastic simulations on vertical axis wind turbines. 2013.
- [22] H Aa Madsen, Uwe Schmidt Paulsen, and L Vitae. Analysis of vawt aerodynamics and design using the actuator cylinder flow model. In *Journal of Physics: Conference Series*, volume 555, page 012065. IOP Publishing, 2014.
- [23] J.F. Manwell, J.G. McGowan, and A.L. Rogers. *Wind Energy Explained: Theory, Design and Application, 2nd Edition*. John Wiley & Sons, Ltd, 2010.
- [24] WJ McCroskey, LW Carr, and KW McAlister. Dynamic stall experiments on oscillating airfoils. *Aiaa Journal*, 14(1):57–63, 1976.
- [25] WJ McCroskey, Kenneth W Mcalister, LW Carr, and SL Pucci. An experimental study of dynamic stall on advanced airfoil sections. volume 1: Summary of the experiment. 1982.
- [26] BG Newman. Actuator-disc theory for vertical-axis wind turbines. *Journal of Wind Engineering and Industrial Aerodynamics*, 15(1):347–355, 1983.
- [27] I. Paraschivoiu. *Wind Turbine Design: With Emphasis on Darrieus Concept*. Polytechnic International Press, 2002.

- [28] Uwe S Paulsen, Luca Vita, Helge A Madsen, Jesper Hattel, Ewen Ritchie, Krisztina M Leban, Petter A Berthelsen, and Stefan Carstensen. 1 st deepwind 5 mw baseline design. *Energy Procedia*, 24:27–35, 2012.
- [29] Siemens Wind Power. Machine learning: Optimizing how wind turbines work, 2014.
- [30] Marco Raciti Castelli, Alessandro Englaro, and Ernesto Benini. The darrieus wind turbine: Proposal for a new performance prediction model based on cfd. *Energy*, 36(8):4919–4934, 2011.
- [31] DTU Riso. Hawc2 e-learning course handout, 2014.
- [32] DTU Riso. Hawc2 official website, 2014.
- [33] DTU Riso. Deepwind official website, 2015.
- [34] Ewen Ritchie, Henning Bjerregaard, Kristian Sloth, and Rune Ryberg Thygesen. Design tools for magnetic bearings. Technical report, 2014.
- [35] Dominique Roddier, Christian Cermelli, Alexia Aubault, and Alla Weinstein. Wind-float: A floating foundation for offshore wind turbines. *Journal of Renewable and Sustainable Energy*, 2(3):033104, 2010.
- [36] Sandia. Innovative offshore vertical-axis wind turbine rotors, 2015.
- [37] Frank Scheurich and Richard E Brown. Modelling the aerodynamics of vertical-axis wind turbines in unsteady wind conditions. *Wind Energy*, 16(1):91–107, 2013.
- [38] Hyunyoung Shin et al. Model test of the oc3-hywind floating offshore wind turbine. In *The Twenty-first International Offshore and Polar Engineering Conference*. International Society of Offshore and Polar Engineers, 2011.
- [39] Yulin Si, Hamid Reza Karimi, and Huijun Gao. Modeling and parameter analysis of the oc3-hywind floating wind turbine with a tuned mass damper in nacelle. *Journal of Applied Mathematics*, 2013, 2013.
- [40] CJ Simão Ferreira. *The near wake of the VAWT, 2D and 3D views of the VAWT aerodynamics*. PhD thesis, PhD Thesis, Delft University of Technology, Delft, the Netherlands, 2009.
- [41] Herbert J Sutherland, Dale E Berg, and Thomas D Ashwill. A retrospective of vawt technology. *Sandia Report, SAND2012*, 304, 2012.
- [42] RJ Templin. Aerodynamic performance theory for the nrc vertical axis wind turbine. *NASA STI Recon Technical Report N*, 76:16618, 1974.
- [43] John Twidell and Gaetano Gaudiosi. *Offshore wind power*. Multi-Science Publishing Company, 2009.
- [44] European Union. Renewable energy, 2015.
- [45] Luca Vita, Troels Friis Pedersen, and Helge Aagaard Madsen. *Offshore Vertical Axis Wind Turbine with Floating and Rotating Foundation*. PhD thesis, 2011.

- [46] wiki pedia. Le nordais, 2013.
- [47] Alessandro Zanon, Pietro Giannattasio, and Carlos J Simão Ferreira. Wake modelling of a vawt in dynamic stall: impact on the prediction of flow and induction fields. *Wind Energy*, 2014.

Appendix A

The numerical model set-up



Figure A.1: Numerical model set-up

Appendix B

MOD-LIN Actuator Cylinder code

```
1 %% ...
2 % AC.m
3 % The implementation of the linear version of Actuator Cylinder model, with
4 % the MOD LIN modification for a H-rotor of VAWT.
5 %
6 % Input:
7 % The external conditions(v_0, rho);
8 % the rotor diemension (B,R,theta_p,twist,c and TSR)
9 % the airfoil data(C_l and C_D).
10 %
11 % Output:
12 % C-T, C_p, w-x, w-y
13 %
14 %*****
15
16 clc
17 clear
18 close all
19
20 %% Initial conditions
21 solidity=0.1;
22 B=3;          % Number of blades
23 R=1;          % [m]
24 c=solidity*2*R/B;% Chord
25 v_0=9;        % Wind speed(Normalized), from west to east
26 rho=1.225;    % Air density
27 twist=0;      % Twist is zero along the blade(H rotor)
28 TSR=4;        % Tip speed ratio
29 theta_p=0;    % Pitch angle
30 omega=TSR*v_0/R; % Rotational speed(Normalized), anti-clockwise(+)
31
32 H=2;          % [m]
33
34 % iteration
35 maxstep=1e3;
```

```

36 tol=1e-5;
37 relax=0.3;
38
39 %% Discretization for the cylinder
40
41 %% Discretization in azimuth direction %%
42 % Mandatory: Starting from non-zero, skip 180, symmetric about 0-180
43 N=36;
44  $\Delta$ .theta=2*pi/N;
45 theta_0=5/180*pi; % Note: The zero position points to the North.
46 theta_N=theta_0+(N-1)* $\Delta$ .theta;
47 theta=linspace(theta_0,theta_N,N);
48
49 %% The cylinder surface coordinates, blade path %%
50 x_b=-R.*sin(theta);
51 y_b=R.*cos(theta);
52
53
54 %% Discretization for the evaluation points
55
56 factor=1.01; % The radius fraction between the cylinder and the evaluation
57               % circle, can't be 1, otherwise NaN
58 x_p=factor.*x_b;
59 y_p=factor.*y_b;
60
61 w_x=zeros(1,length(theta));
62 w_y=zeros(1,length(theta));
63
64
65 %% Influence coefficient %%
66 % Integral, second time discretization
67 d_theta_step=0.1* $\Delta$ .theta;
68 for j=1:N % different evaluation points
69     for index=1:N % influence from the others
70         d_theta=(theta(index)-0.5* $\Delta$ .theta):d_theta_step:(theta(index)...
71             +0.5* $\Delta$ .theta);
72         integral_x=(-(x_p(j)+sin(d_theta)).*sin(d_theta)...
73             +(y_p(j)-cos(d_theta)).*cos(d_theta))./...
74             ((x_p(j)+sin(d_theta)).^2+(y_p(j)-cos(d_theta)).^2);
75         integral_y=(-(x_p(j)+sin(d_theta)).*cos(d_theta)...
76             -(y_p(j)-cos(d_theta)).*sin(d_theta))./...
77             ((x_p(j)+sin(d_theta)).^2+(y_p(j)-cos(d_theta)).^2);
78         R_wx(index,j)=-trapz(d_theta,integral_x);
79         R_wy(index,j)=-trapz(d_theta,integral_y);
80     end
81 end
82 % figure
83 % plot(theta,R_wx(33,:))
84 % title('R_wx(33,:)')
85
86 for step=1:maxstep
87
88     if factor ==1
89         display('Model Defect')
90         break
91     end
92
93

```

```

94     %% AOA computation
95     %%% The relatived speed %%%
96     V_rel_x=v_0+omega*R.*cos(theta)+v_0.*w_x; % positive: same as the wind
97                                           %           speed
98     V_rel_y=omega*R.*sin(theta)+v_0.*w_y;    % positive: north
99     V_rel=sqrt(V_rel_x.^2+V_rel_y.^2);
100
101     %%% AOA %%%
102     % Computation need the velocity fluctuation, but neglected here
103     V_t=V_rel_y.*sin(theta)+V_rel_x.*cos(theta); % Tangential, from
104                                           % leading to ...
105                                           %           trailing edge
106     V_r=-(V_rel_y.*cos(theta)-V_rel_x.*sin(theta)); % Radial, pointing in
107     phi=atan(V_r./V_t); % Flow angle
108     AOA=phi-theta_p-twist;
109
110     %% Load coefficient (Integral terms)
111     % Physically, it is the pressure jump along the cylinder
112
113     %%% Airfoil Data (Linear Model) %%%
114     C_l=2*pi.*sin(AOA);
115     C_d=0.023*ones(1,length(AOA)); % From AIAA paper
116
117     C_n=C_l.*cos(AOA)+C_d.*sin(AOA);
118     C_t=C_l.*sin(AOA)-C_d.*cos(AOA);
119
120     %%% Blade forces %%%
121     F_n=0.5*rho.*V_rel.^2*c.*C_n; % opposite to V_r
122     F_t=0.5*rho.*V_rel.^2*c.*C_t; % opposite to V_t
123
124     %%% Load coefficients %%%
125     Q_n=B.*F_n/(2*pi*R*rho*v_0^2);
126     Q_t=B.*F_t/(2*pi*R*rho*v_0^2);
127
128
129     %% Velocity fluctuation
130
131     w_x_old=w_x;
132     w_y_old=w_y;
133
134     %%% Influence coefficient %%%
135     for i=1:N
136         for j=1:N
137             w_x_i(i,j)=Q_n(i).*R_wx(i,j);
138         end
139     end
140
141     for i=1:N
142         for j=1:N
143             w_y_i(i,j)=Q_n(i).*R_wy(i,j);
144         end
145     end
146
147     w_x=1/(2*pi).*sum(w_x_i,1);
148     w_y=1/(2*pi).*sum(w_y_i,1);
149
150     % Outside the cylinder

```

```

151         if factor >1
152             for j=N/2+1:N
153                 w_x(j)=w_x(j)+Q_n(j)-Q_n(N+1-j);
154             end
155
156             % Inside the cylinder
157         else if factor <1
158             for j=1:N/2
159                 w_x(j)=w_x(j)-Q_n(j);
160             end
161             for j=N/2+1:N
162                 w_x(j)=w_x(j)-Q_n(N+1-j);
163             end
164         end
165     end
166
167
168     %% MOD LIN model
169     % To obtain the factor k_a to modify the linear version of AC model
170
171     % C_T=trapz(theta,Q_n)/(0.5*2*R*rho*v_0^2);
172     C_T=trapz(theta,Q_n.*sin(theta)+Q_t.*cos(theta));
173     a_lin=C_T/4;
174     a=fsolve(@(a) a-a^2-a_lin,0.0001);
175     k_a=1/(1-a);
176
177     C_p_i=trapz(theta,Q_n.*V_r./(v_0)); % Ideal C_p
178     C_p_r=1/(2*pi)*trapz(theta,B.*(F_t.*omega.*R))/(0.5*rho*v_0^3*2*R);
179
180     % Apply MOD LIN
181     w_x=k_a.*w_x;
182     w_y=k_a.*w_y;
183
184     % Relaxation
185     w_x=((1-relax).*w_x+relax.*w_x_old);
186     w_y=((1-relax).*w_y+relax.*w_y_old);
187
188
189     if abs(w_x-w_x_old)<=tol & abs(w_y-w_y_old)<=tol
190         step
191         break
192     end
193
194 end

```

Appendix C

The outcome of the preprocessor

Note: Only part of outcome is presented due to the long length.

Input file for Flap dyn.stall model. Generated with Delphi preprocessor

.Linear Region: Aoa Cl0 [rad]:

1.471E-5

.Linear Region: dCl / dAoa [1/rad]:

6.58758341

.Linear Region: dCl / dBeta [1/deg]:

0.04108133

. Polars: 1.Aoa — 2.Beta — 3.Clst — 4.Cl Att — 5.Cl fs — 6.Cd — 7.Cm — 8.F

36100

-1 -49 -0.6176 -0.6902106 -0.3352437 0.0072499998 0 0.795444

-1 -48 -0.6176 -0.6902106 -0.3352437 0.0072499998 0 0.795444

-1 -47 -0.6176 -0.6902106 -0.3352437 0.0072499998 0 0.795444

-1 -46 -0.6176 -0.6902106 -0.3352437 0.0072499998 0 0.795444

-1 -45 -0.6176 -0.6902106 -0.3352437 0.0072499998 0 0.795444

-1 -44 -0.6176 -0.6902106 -0.3352437 0.0072499998 0 0.795444

-1 -43 -0.6176 -0.6902106 -0.3352437 0.0072499998 0 0.795444

-1 -42 -0.6176 -0.6902106 -0.3352437 0.0072499998 0 0.795444

-1 -41 -0.6176 -0.6902106 -0.3352437 0.0072499998 0 0.795444

-1 -40 -0.6176 -0.6902106 -0.3352437 0.0072499998 0 0.795444

-1 -39 -0.6176 -0.6902106 -0.3352437 0.0072499998 0 0.795444

-1 -38 -0.6176 -0.6902106 -0.3352437 0.0072499998 0 0.795444
-1 -37 -0.6176 -0.6902106 -0.3352437 0.0072499998 0 0.795444
-1 -36 -0.6176 -0.6902106 -0.3352437 0.0072499998 0 0.795444
-1 -35 -0.6176 -0.6902106 -0.3352437 0.0072499998 0 0.795444
-1 -34 -0.6176 -0.6902106 -0.3352437 0.0072499998 0 0.795444
-1 -33 -0.6176 -0.6902106 -0.3352437 0.0072499998 0 0.795444
-1 -32 -0.6176 -0.6902106 -0.3352437 0.0072499998 0 0.795444
-1 -31 -0.6176 -0.6902106 -0.3352437 0.0072499998 0 0.795444
-1 -30 -0.6176 -0.6902106 -0.3352437 0.0072499998 0 0.795444
-1 -29 -0.6176 -0.6902106 -0.3352437 0.0072499998 0 0.795444
-1 -28 -0.6176 -0.6902106 -0.3352437 0.0072499998 0 0.795444
-1 -27 -0.6176 -0.6902106 -0.3352437 0.0072499998 0 0.795444
-1 -26 -0.6176 -0.6902106 -0.3352437 0.0072499998 0 0.795444
-1 -25 -0.6176 -0.6902106 -0.3352437 0.0072499998 0 0.795444
-1 -24 -0.6176 -0.6902106 -0.3352437 0.0072499998 0 0.795444
-1 -23 -0.6176 -0.6902106 -0.3352437 0.0072499998 0 0.795444
-1 -22 -0.6176 -0.6902106 -0.3352437 0.0072499998 0 0.795444
-1 -21 -0.6176 -0.6902106 -0.3352437 0.0072499998 0 0.795444
-1 -20 -0.6176 -0.6902106 -0.3352437 0.0072499998 0 0.795444
-1 -19 -0.6176 -0.6902106 -0.3352437 0.0072499998 0 0.795444
-1 -18 -0.6176 -0.6902106 -0.3352437 0.0072499998 0 0.795444
-1 -17 -0.6176 -0.6902106 -0.3352437 0.0072499998 0 0.795444
-1 -16 -0.6176 -0.6902106 -0.3352437 0.0072499998 0 0.795444
-1 -15 -0.6176 -0.6902106 -0.3352437 0.0072499998 0 0.795444
-1 -14 -0.6176 -0.6902106 -0.3352437 0.0072499998 0 0.795444
-1 -13 -0.59265 -0.6491293 -0.3169792 0.0071049999 0 0.8325045
-1 -12 -0.5677 -0.6080479 -0.2987147 0.0069599999 0 0.869565
-1 -11 -0.537 -0.5669666 -0.2795693 0.0068399999 0 0.8978934
-1 -10 -0.5063 -0.5258853 -0.2604239 0.0067199999 0 0.9262217
-1 -9 -0.4706 -0.4848039 -0.2405828 0.006635 0 0.9433276
-1 -8 -0.4349 -0.4437226 -0.2207417 0.00655 0 0.9604334
-1 -7 -0.39705 -0.4026412 -0.2006126 0.0064599998 0 0.9737003
-1 -6 -0.3592 -0.3615599 -0.1804835 0.0063700001 0 0.9869673

-1 -5 -0.3196 -0.3207799 -0.1602418 0.0062899999 0 0.9934837
-1 -4 -0.28 -0.28 -0.14 0.0062099998 0 1
-1 -3 -0.23945 -0.23945 -0.119725 0.0061599999 0 1
-1 -2 -0.1989 -0.1989 -0.09945 0.00611 0 1
-1 -1 -0.1578 -0.1578 -0.0789 0.0060800002 0 1
-1 0 -0.1167 -0.1167 -0.05835 0.00605 0 1
-1 1 -0.07565 -0.07565 -0.037825 0.0060399999 0 1
-1 2 -0.0346 -0.0346 -0.0173 0.0060299998 0 1
-1 3 0.00615 0.00615 0.003075 0.0060299998 0 1
-1 4 0.0469 0.0469 0.02345 0.0060299998 0 1
-1 5 0.0863904 0.089158 0.0442217 0.0061374092 0 0.9583332
-1 6 0.1258808 0.1314161 0.0649935 0.0062448182 0 0.9166663
-1 7 0.1641904 0.166958 0.1337467 0.006202409 0 0.9389844
-1 8 0.2025 0.2025 0.2025 0.0061599999 0 0.9613025
-1 9 0.2376 0.2491207 0.1736553 0.006205 0 0.9043202
-1 10 0.2727 0.2957414 0.1448105 0.0062500001 0 0.8473381
-1 11 0.2993983 0.310919 0.2354535 0.0063312324 0 0.8551733
-1 12 0.3260965 0.3260965 0.3260965 0.0064124647 0 0.8630086
-1 13 0.3507483 0.3507483 0.3507483 0.0065362323 0 0.858882
-1 14 0.3754 0.3754 0.3754 0.00666 0 0.8547554
-1 15 0.3754 0.3754 0.3754 0.00666 0 0.8547554
-1 16 0.3754 0.3754 0.3754 0.00666 0 0.8547554
-1 17 0.3754 0.3754 0.3754 0.00666 0 0.8547554
-1 18 0.3754 0.3754 0.3754 0.00666 0 0.8547554
-1 19 0.3754 0.3754 0.3754 0.00666 0 0.8547554
-1 20 0.3754 0.3754 0.3754 0.00666 0 0.8547554
-1 21 0.3754 0.3754 0.3754 0.00666 0 0.8547554
-1 22 0.3754 0.3754 0.3754 0.00666 0 0.8547554
-1 23 0.3754 0.3754 0.3754 0.00666 0 0.8547554
-1 24 0.3754 0.3754 0.3754 0.00666 0 0.8547554
-1 25 0.3754 0.3754 0.3754 0.00666 0 0.8547554
-1 26 0.3754 0.3754 0.3754 0.00666 0 0.8547554
-1 27 0.3754 0.3754 0.3754 0.00666 0 0.8547554

-1 28 0.3754 0.3754 0.3754 0.00666 0 0.8547554
-1 29 0.3754 0.3754 0.3754 0.00666 0 0.8547554
-1 30 0.3754 0.3754 0.3754 0.00666 0 0.8547554
-1 31 0.3754 0.3754 0.3754 0.00666 0 0.8547554
-1 32 0.3754 0.3754 0.3754 0.00666 0 0.8547554
-1 33 0.3754 0.3754 0.3754 0.00666 0 0.8547554
-1 34 0.3754 0.3754 0.3754 0.00666 0 0.8547554
-1 35 0.3754 0.3754 0.3754 0.00666 0 0.8547554
-1 36 0.3754 0.3754 0.3754 0.00666 0 0.8547554
-1 37 0.3754 0.3754 0.3754 0.00666 0 0.8547554
-1 38 0.3754 0.3754 0.3754 0.00666 0 0.8547554
-1 39 0.3754 0.3754 0.3754 0.00666 0 0.8547554
-1 40 0.3754 0.3754 0.3754 0.00666 0 0.8547554
-1 41 0.3754 0.3754 0.3754 0.00666 0 0.8547554
-1 42 0.3754 0.3754 0.3754 0.00666 0 0.8547554
-1 43 0.3754 0.3754 0.3754 0.00666 0 0.8547554
-1 44 0.3754 0.3754 0.3754 0.00666 0 0.8547554
-1 45 0.3754 0.3754 0.3754 0.00666 0 0.8547554
-1 46 0.3754 0.3754 0.3754 0.00666 0 0.8547554
-1 47 0.3754 0.3754 0.3754 0.00666 0 0.8547554
-1 48 0.3754 0.3754 0.3754 0.00666 0 0.8547554
-1 49 0.3754 0.3754 0.3754 0.00666 0 0.8547554
-1 50 0.3754 0.3754 0.3754 0.00666 0 0.8547554
0 -49 -0.4971571 -0.5752355 -0.2767368 0.0069081988 0 0.7384295
0 -48 -0.4971571 -0.5752355 -0.2767368 0.0069081988 0 0.7384295
0 -47 -0.4971571 -0.5752355 -0.2767368 0.0069081988 0 0.7384295
0 -46 -0.4971571 -0.5752355 -0.2767368 0.0069081988 0 0.7384295
0 -45 -0.4971571 -0.5752355 -0.2767368 0.0069081988 0 0.7384295
0 -44 -0.4971571 -0.5752355 -0.2767368 0.0069081988 0 0.7384295
0 -43 -0.4971571 -0.5752355 -0.2767368 0.0069081988 0 0.7384295
0 -42 -0.4971571 -0.5752355 -0.2767368 0.0069081988 0 0.7384295
0 -41 -0.4971571 -0.5752355 -0.2767368 0.0069081988 0 0.7384295
0 -40 -0.4971571 -0.5752355 -0.2767368 0.0069081988 0 0.7384295

0 -39 -0.4971571 -0.5752355 -0.2767368 0.0069081988 0 0.7384295
0 -38 -0.4971571 -0.5752355 -0.2767368 0.0069081988 0 0.7384295
0 -37 -0.4971571 -0.5752355 -0.2767368 0.0069081988 0 0.7384295
0 -36 -0.4971571 -0.5752355 -0.2767368 0.0069081988 0 0.7384295
0 -35 -0.4971571 -0.5752355 -0.2767368 0.0069081988 0 0.7384295
0 -34 -0.4971571 -0.5752355 -0.2767368 0.0069081988 0 0.7384295
0 -33 -0.4971571 -0.5752355 -0.2767368 0.0069081988 0 0.7384295
0 -32 -0.4971571 -0.5752355 -0.2767368 0.0069081988 0 0.7384295
0 -31 -0.4971571 -0.5752355 -0.2767368 0.0069081988 0 0.7384295
0 -30 -0.4971571 -0.5752355 -0.2767368 0.0069081988 0 0.7384295
0 -29 -0.4971571 -0.5752355 -0.2767368 0.0069081988 0 0.7384295
0 -28 -0.4971571 -0.5752355 -0.2767368 0.0069081988 0 0.7384295
0 -27 -0.4971571 -0.5752355 -0.2767368 0.0069081988 0 0.7384295
0 -26 -0.4971571 -0.5752355 -0.2767368 0.0069081988 0 0.7384295
0 -25 -0.4971571 -0.5752355 -0.2767368 0.0069081988 0 0.7384295
0 -24 -0.4971571 -0.5752355 -0.2767368 0.0069081988 0 0.7384295
0 -23 -0.4971571 -0.5752355 -0.2767368 0.0069081988 0 0.7384295
0 -22 -0.4971571 -0.5752355 -0.2767368 0.0069081988 0 0.7384295
0 -21 -0.4971571 -0.5752355 -0.2767368 0.0069081988 0 0.7384295
0 -20 -0.4971571 -0.5752355 -0.2767368 0.0069081988 0 0.7384295
0 -19 -0.4971571 -0.5752355 -0.2767368 0.0069081988 0 0.7384295
0 -18 -0.4971571 -0.5752355 -0.2767368 0.0069081988 0 0.7384295
0 -17 -0.4971571 -0.5752355 -0.2767368 0.0069081988 0 0.7384295
0 -16 -0.4971571 -0.5752355 -0.2767368 0.0069081988 0 0.7384295
0 -15 -0.4971571 -0.5752355 -0.2767368 0.0069081988 0 0.7384295
0 -14 -0.4971571 -0.5752355 -0.2767368 0.0069081988 0 0.7384295
0 -13 -0.4725037 -0.5341542 -0.2585996 0.0067660403 0 0.779704
0 -12 -0.4478502 -0.4930729 -0.2404625 0.0066238819 0 0.8209785
0 -11 -0.4187574 -0.4519916 -0.2215771 0.0065290453 0 0.8594717
0 -10 -0.3896646 -0.4109102 -0.2026918 0.0064342082 0 0.8979648
0 -9 -0.3540518 -0.3698289 -0.1828729 0.0063907891 0 0.917875
0 -8 -0.318439 -0.3287476 -0.1630541 0.0063473699 0 0.9377851
0 -7 -0.2807137 -0.2876662 -0.142946 0.0062613618 0 0.9543611

0 -6 -0.2429885 -0.2465849 -0.1228379 0.0061753532 0 0.9709371
0 -5 -0.2032664 -0.2050646 -0.102305 0.0061308015 0 0.9854686
0 -4 -0.1635443 -0.1635443 -0.0817721 0.0060862498 0 1
0 -3 -0.1228692 -0.1229019 -0.0614469 0.0060662855 0 0.9992034
0 -2 -0.082194 -0.0822596 -0.0411216 0.0060463208 0 0.9984068
0 -1 -0.041097 -0.0411298 -0.0205608 0.0060481601 0 0.9992034
0 0 0 0 0 0.00605 0 1
0 1 0.0410657 0.0410657 0.0205329 0.0060531972 0 1
0 2 0.0821314 0.0821314 0.0410657 0.0060563944 0 1
0 3 0.1228629 0.1228629 0.0614314 0.0060733026 0 1
0 4 0.1635943 0.1635943 0.0817972 0.0060902112 0 1
0 5 0.2030339 0.2049927 0.1022485 0.0062318915 0 0.9841633
0 6 0.2424734 0.2463911 0.1226999 0.0063735717 0 0.9683267
0 7 0.2806652 0.2874724 0.1428686 0.0063382923 0 0.9548711
0 8 0.318857 0.3285537 0.1630373 0.0063030128 0 0.9414155
0 9 0.3543294 0.3696351 0.1828384 0.0063708317 0 0.9204509
0 10 0.3898018 0.4107164 0.2026396 0.0064386511 0 0.8994862
0 11 0.4188544 0.4293118 0.3252733 0.0065440335 0 0.8812474
0 12 0.4479071 0.4479071 0.4479071 0.0066494159 0 0.8630086
0 13 0.4727071 0.4727071 0.4727071 0.0067801285 0 0.8481977
0 14 0.4975071 0.4975071 0.4975071 0.0069108405 0 0.8333868
0 15 0.4975071 0.4975071 0.4975071 0.0069108405 0 0.8333868
0 16 0.4975071 0.4975071 0.4975071 0.0069108405 0 0.8333868
0 17 0.4975071 0.4975071 0.4975071 0.0069108405 0 0.8333868
0 18 0.4975071 0.4975071 0.4975071 0.0069108405 0 0.8333868
0 19 0.4975071 0.4975071 0.4975071 0.0069108405 0 0.8333868
0 20 0.4975071 0.4975071 0.4975071 0.0069108405 0 0.8333868
0 21 0.4975071 0.4975071 0.4975071 0.0069108405 0 0.8333868
0 22 0.4975071 0.4975071 0.4975071 0.0069108405 0 0.8333868
0 23 0.4975071 0.4975071 0.4975071 0.0069108405 0 0.8333868
0 24 0.4975071 0.4975071 0.4975071 0.0069108405 0 0.8333868
0 25 0.4975071 0.4975071 0.4975071 0.0069108405 0 0.8333868
0 26 0.4975071 0.4975071 0.4975071 0.0069108405 0 0.8333868

0 27 0.4975071 0.4975071 0.4975071 0.0069108405 0 0.8333868
0 28 0.4975071 0.4975071 0.4975071 0.0069108405 0 0.8333868
0 29 0.4975071 0.4975071 0.4975071 0.0069108405 0 0.8333868
0 30 0.4975071 0.4975071 0.4975071 0.0069108405 0 0.8333868
0 31 0.4975071 0.4975071 0.4975071 0.0069108405 0 0.8333868
0 32 0.4975071 0.4975071 0.4975071 0.0069108405 0 0.8333868
0 33 0.4975071 0.4975071 0.4975071 0.0069108405 0 0.8333868
0 34 0.4975071 0.4975071 0.4975071 0.0069108405 0 0.8333868
0 35 0.4975071 0.4975071 0.4975071 0.0069108405 0 0.8333868
0 36 0.4975071 0.4975071 0.4975071 0.0069108405 0 0.8333868
0 37 0.4975071 0.4975071 0.4975071 0.0069108405 0 0.8333868
0 38 0.4975071 0.4975071 0.4975071 0.0069108405 0 0.8333868
0 39 0.4975071 0.4975071 0.4975071 0.0069108405 0 0.8333868
0 40 0.4975071 0.4975071 0.4975071 0.0069108405 0 0.8333868
0 41 0.4975071 0.4975071 0.4975071 0.0069108405 0 0.8333868
0 42 0.4975071 0.4975071 0.4975071 0.0069108405 0 0.8333868
0 43 0.4975071 0.4975071 0.4975071 0.0069108405 0 0.8333868
0 44 0.4975071 0.4975071 0.4975071 0.0069108405 0 0.8333868
0 45 0.4975071 0.4975071 0.4975071 0.0069108405 0 0.8333868
0 46 0.4975071 0.4975071 0.4975071 0.0069108405 0 0.8333868
0 47 0.4975071 0.4975071 0.4975071 0.0069108405 0 0.8333868
0 48 0.4975071 0.4975071 0.4975071 0.0069108405 0 0.8333868
0 49 0.4975071 0.4975071 0.4975071 0.0069108405 0 0.8333868
0 50 0.4975071 0.4975071 0.4975071 0.0069108405 0 0.8333868
1 -49 -0.3751 -0.3751 -0.3751 0.00666 0 0.7460281
1 -48 -0.3751 -0.3751 -0.3751 0.00666 0 0.7460281
1 -47 -0.3751 -0.3751 -0.3751 0.00666 0 0.7460281
1 -46 -0.3751 -0.3751 -0.3751 0.00666 0 0.7460281
1 -45 -0.3751 -0.3751 -0.3751 0.00666 0 0.7460281
1 -44 -0.3751 -0.3751 -0.3751 0.00666 0 0.7460281
1 -43 -0.3751 -0.3751 -0.3751 0.00666 0 0.7460281
1 -42 -0.3751 -0.3751 -0.3751 0.00666 0 0.7460281
1 -41 -0.3751 -0.3751 -0.3751 0.00666 0 0.7460281

1 -40 -0.3751 -0.3751 -0.3751 0.00666 0 0.7460281
1 -39 -0.3751 -0.3751 -0.3751 0.00666 0 0.7460281
1 -38 -0.3751 -0.3751 -0.3751 0.00666 0 0.7460281
1 -37 -0.3751 -0.3751 -0.3751 0.00666 0 0.7460281
1 -36 -0.3751 -0.3751 -0.3751 0.00666 0 0.7460281
1 -35 -0.3751 -0.3751 -0.3751 0.00666 0 0.7460281
1 -34 -0.3751 -0.3751 -0.3751 0.00666 0 0.7460281
1 -33 -0.3751 -0.3751 -0.3751 0.00666 0 0.7460281
1 -32 -0.3751 -0.3751 -0.3751 0.00666 0 0.7460281
1 -31 -0.3751 -0.3751 -0.3751 0.00666 0 0.7460281
1 -30 -0.3751 -0.3751 -0.3751 0.00666 0 0.7460281
1 -29 -0.3751 -0.3751 -0.3751 0.00666 0 0.7460281
1 -28 -0.3751 -0.3751 -0.3751 0.00666 0 0.7460281
1 -27 -0.3751 -0.3751 -0.3751 0.00666 0 0.7460281
1 -26 -0.3751 -0.3751 -0.3751 0.00666 0 0.7460281
1 -25 -0.3751 -0.3751 -0.3751 0.00666 0 0.7460281
1 -24 -0.3751 -0.3751 -0.3751 0.00666 0 0.7460281
1 -23 -0.3751 -0.3751 -0.3751 0.00666 0 0.7460281
1 -22 -0.3751 -0.3751 -0.3751 0.00666 0 0.7460281
1 -21 -0.3751 -0.3751 -0.3751 0.00666 0 0.7460281
1 -20 -0.3751 -0.3751 -0.3751 0.00666 0 0.7460281
1 -19 -0.3751 -0.3751 -0.3751 0.00666 0 0.7460281
1 -18 -0.3751 -0.3751 -0.3751 0.00666 0 0.7460281
1 -17 -0.3751 -0.3751 -0.3751 0.00666 0 0.7460281
1 -16 -0.3751 -0.3751 -0.3751 0.00666 0 0.7460281
1 -15 -0.3751 -0.3751 -0.3751 0.00666 0 0.7460281
1 -14 -0.3751 -0.3751 -0.3751 0.00666 0 0.7460281
1 -13 -0.35075 -0.3765989 -0.2784691 0.0065199998 0 0.7413063
1 -12 -0.3264 -0.3780979 -0.1818382 0.0063800002 0 0.7365844
1 -11 -0.29945 -0.3370165 -0.163345 0.0063149999 0 0.7907349
1 -10 -0.2725 -0.2959352 -0.1448519 0.0062500001 0 0.8448855
1 -9 -0.2371 -0.2488176 -0.1228509 0.0062349997 0 0.9224427
1 -8 -0.2017 -0.2017 -0.10085 0.0062199999 0 1

1 -7 -0.1641 -0.1641 -0.113675 0.0061499998 0 0.9831018
1 -6 -0.1265 -0.1265 -0.1265 0.0060800002 0 0.9662037
1 -5 -0.0867 -0.0867 -0.074975 0.0060549998 0 0.9831018
1 -4 -0.0469 -0.0469 -0.02345 0.0060299998 0 1
1 -3 -0.00615 -0.00615 -0.003075 0.006025 0 1
1 -2 0.0346 0.0346 0.0173 0.0060199997 0 1
1 -1 0.07565 0.07565 0.037825 0.0060350001 0 1
1 0 0.1167 0.1167 0.05835 0.00605 0 1
1 1 0.15775 0.15775 0.078875 0.006085 0 1
1 2 0.1988 0.1988 0.0994 0.00612 0 1
1 3 0.23945 0.23945 0.119725 0.0061699999 0 1
1 4 0.2801 0.2801 0.14005 0.0062199999 0 1
1 5 0.3195132 0.320733 0.1602133 0.0063853739 0 0.9932602
1 6 0.3589264 0.3613661 0.1803765 0.0065507479 0 0.9865205
1 7 0.3969132 0.4024474 0.2005232 0.0065553738 0 0.973901
1 8 0.4349 0.4435288 0.2206698 0.0065600001 0 0.9612814
1 9 0.47065 0.4846101 0.2405178 0.0066450001 0 0.9442864
1 10 0.5064 0.5256914 0.2603658 0.00673 0 0.9272914
1 11 0.5373 0.5667728 0.2795398 0.00685 0 0.8995097
1 12 0.5682 0.6078541 0.2987138 0.00697 0 0.8717279
1 13 0.5931 0.612927 0.4583569 0.0071100001 0 0.8525574
1 14 0.618 0.618 0.618 0.0072499998 0 0.8333868
1 15 0.618 0.618 0.618 0.0072499998 0 0.8333868
1 16 0.618 0.618 0.618 0.0072499998 0 0.8333868
1 17 0.618 0.618 0.618 0.0072499998 0 0.8333868
1 18 0.618 0.618 0.618 0.0072499998 0 0.8333868
1 19 0.618 0.618 0.618 0.0072499998 0 0.8333868
1 20 0.618 0.618 0.618 0.0072499998 0 0.8333868
1 21 0.618 0.618 0.618 0.0072499998 0 0.8333868
1 22 0.618 0.618 0.618 0.0072499998 0 0.8333868
1 23 0.618 0.618 0.618 0.0072499998 0 0.8333868
1 24 0.618 0.618 0.618 0.0072499998 0 0.8333868
1 25 0.618 0.618 0.618 0.0072499998 0 0.8333868

1 26 0.618 0.618 0.618 0.0072499998 0 0.8333868
1 27 0.618 0.618 0.618 0.0072499998 0 0.8333868
1 28 0.618 0.618 0.618 0.0072499998 0 0.8333868
1 29 0.618 0.618 0.618 0.0072499998 0 0.8333868
1 30 0.618 0.618 0.618 0.0072499998 0 0.8333868
1 31 0.618 0.618 0.618 0.0072499998 0 0.8333868
1 32 0.618 0.618 0.618 0.0072499998 0 0.8333868
1 33 0.618 0.618 0.618 0.0072499998 0 0.8333868
1 34 0.618 0.618 0.618 0.0072499998 0 0.8333868
1 35 0.618 0.618 0.618 0.0072499998 0 0.8333868
1 36 0.618 0.618 0.618 0.0072499998 0 0.8333868
1 37 0.618 0.618 0.618 0.0072499998 0 0.8333868
1 38 0.618 0.618 0.618 0.0072499998 0 0.8333868
1 39 0.618 0.618 0.618 0.0072499998 0 0.8333868
1 40 0.618 0.618 0.618 0.0072499998 0 0.8333868
1 41 0.618 0.618 0.618 0.0072499998 0 0.8333868
1 42 0.618 0.618 0.618 0.0072499998 0 0.8333868
1 43 0.618 0.618 0.618 0.0072499998 0 0.8333868
1 44 0.618 0.618 0.618 0.0072499998 0 0.8333868
1 45 0.618 0.618 0.618 0.0072499998 0 0.8333868
1 46 0.618 0.618 0.618 0.0072499998 0 0.8333868
1 47 0.618 0.618 0.618 0.0072499998 0 0.8333868
1 48 0.618 0.618 0.618 0.0072499998 0 0.8333868
1 49 0.618 0.618 0.618 0.0072499998 0 0.8333868
1 50 0.618 0.618 0.618 0.0072499998 0 0.8333868